CONSTRAINING THE GEOMETRY, SIZE SCALE AND PHYSICAL CONDITIONS OF OUTFLOWING BROAD ABSORPTION LINE REGIONS IN QUASARS

by

Sui Chi Woo

B.S. in Physics, The University of Hong Kong, 2002

M.Phil. in Physics, The University of Hong Kong, 2004

M.S. in Physics, University of Pittsburgh, 2007

Submitted to the Graduate Faculty of

the Department of Physics and Astronomy in partial fulfillment

of the requirements for the degree of

Doctor of Philosophy

University of Pittsburgh

2013

UNIVERSITY OF PITTSBURGH

PHYSICS AND ASTRONOMY DEPARTMENT

This dissertation was presented

by

Sui Chi Woo

It was defended on

December 12th 2012

and approved by

David Turnshek, Department of Physics and Astronomy, Chair and Professor

John Hillier, Department of Physics and Astronomy, Professor

Anthony Duncan, Department of Physics and Astronomy, Professor

William Harbert, Department of Geology & Planetary Science, Chair and Professor

Andrew Zentner, Department of Physics and Astronomy, Associate Professor

Dissertation Advisors: David Turnshek, Department of Physics and Astronomy, Chair and Professor,

John Hillier, Department of Physics and Astronomy, Professor

CONSTRAINING THE GEOMETRY, SIZE SCALE AND PHYSICAL CONDITIONS OF OUTFLOWING BROAD ABSORPTION LINE REGIONS IN QUASARS

Sui Chi Woo, PhD

University of Pittsburgh, 2013

Quasars are known for generating luminosities of up to $10^{47}\,\mathrm{erg\,s^{-1}}$ in volumes of scales smaller than $2 \times 10^{15}\,\mathrm{cm}$. The optical/UV continuum emission is generally believed to arise from a rotating accretion disk (AD) surrounding a supermassive black hole (SMBH) of $\sim 10^8 M_\odot$. Such emission can be calculated by treating the AD as a multi-temperature blackbody. While the continuum emitting region is well defined, the properties, location and kinematics of the broad emission line regions (BELRs) and broad absorption line regions (BALRs) remain unclear. On one hand, the reverberation mapping technique can give constraints on the location of the BELRs, but not the kinematics. On the other hand, the line-of-sight kinematics of the BALRs is directly observable, but their locations are not well constrained, resulting in a large range of inferred distances, from 0.01 pc to tens of kpc. Therefore, I combined observational results to investigate the geometry, size, and physical conditions of the BELRs and BALRs.

I verified that the Lyα and CIV BELRs are located at a similar distance. Using these findings, I was able to constrain the size of the Lyα BELR and place a lower limit on the size of the NV BALR. I built an empirical model with the optical/UV continuum emission from the AD, the BELR from the chromosphere of the AD, and the outflowing BALR. In the continuum region, I found that over 95 percent of the total flux comes from the region at $\sim 125 r_g$, where r_g is the gravitational radius of the SMBH. For the BELRs, I computed a disk-wind model with relativistic effects to explain the often-observed single-peaked BEL

profiles. However, I show that such a model cannot explain the observed blue asymmetries in the high-ionization BELs or their blueshifted peaks relative to low-ionization BELs. Using results on time variability of BALR gas, and assuming the variability is caused by the gas moving perpendicular across the line-of-sight over a time scale of about a year, I conclude that the BALR gas is clumpy or filamentary, with the clumps having a size scale of $\sim 10^{-3}$ pc.

TABLE OF CONTENTS

LIST OF TABLES

LIST OF FIGURES

1.0 INTRODUCTION

1.1 ACTIVE GALACTIC NUCLEI OVERVIEW

Active Galactic Nuclei (AGN) is the term used to describe highly energetic objects that exist in the central regions of galaxies. In AGN a huge amount of energy is radiated across the entire electromagnetic spectrum. The physical structure of AGN is now thought to be well understood. At the AGN center there is a supermassive black hole (SMBH), with masses of millions to billions of solar masses. Moving out from the SMBH, there is the hot accretion disk (AD) with a scale of light days, followed by the broad emission line region (BELR) gas with a scale of hundreds of light days, then comes the optically thick doughnut-shaped torus with a scale of parsecs, and lastly is the narrow emission line region (NELR) gas with a scale of hundreds of parsecs.

The detailed classification of AGN is based on their observational properties. Our understanding has improved and evolved throughout the decades, as better instrumentation has become available to clarify their properties and resolve their features to a higher degree. There have been many subclasses of AGN defined in various ways and in different astronomical wavelength bands. For example, Seyfert galaxies and quasars are two of the main classes of AGN. Low luminosity quasars are indistinguishable from bright Type 1 Seyferts, so there seems to a continuum of similar objects separated into two classes following a luminosity-size scaling.

Seyfert galaxies, the low-to-medium luminosity AGN, are divided into two types. Type 1s have luminosities of $\sim 10^{44}\,\mathrm{erg\,s^{-1}}$ with optical emission line widths of a thousand kilometers per second or more, whereas Type 2s have luminosities of $\sim 10^{43}\,\mathrm{erg\,s^{-1}}$ with narrower widths, e.g., hundreds of kilometers per second. Emission lines with broad bases in Type

1s often exhibit variability on timescales of tens of days, similar to that of their ultraviolet (UV) continua, while narrower emission lines in both types show no significant variations. In Type 2s, the broad emission component appears to be missing, but spectropolarimetry of some nearby bright Type 2 Seyferts has shown a broad base to the permitted emission lines in polarized (reflected) light (Antonucci & Miller 1985; Moran et al. 2000) suggesting that the BELR is obscured from our direct view.

Quasars, the high-luminosity AGN, are generally hundreds of times brighter than Seyfert galaxies. Quasars are particularly numerous at redshifts of $z \sim 2$ when the Universe was about one third of its present age. Their spectra resemble the spectra of Type 1 Seyfert galaxies, and the bases of their broad emission lines (BELs) can reach up to one tenth of the speed of light while the full width half maximums (FWHMs) of these lines can surpass ten thousand kilometers per second in extreme cases. Generically, they are roughly divided into radio-loud and radio-quiet, although radio-loud quasars are about ten times fewer than radio-quiet ones. In addition to differing in their radio properties, the two groups differ in the ratio of their x-ray to optical luminosities. This ratio is larger in radio-loud quasars than in radio-quiet quasars (Ku et al. 1980). Radio loudness is usually associated with a relativistic outflow or jet. The radio emission is due to synchrotron radiation of high energy electrons spiraling along magnetic fields.

From an observational viewpoint, there have been numerous well documented studies of the lower-luminosity Seyfert galaxies as they are nearby and brighter, and easier to observe, while studies of quasars are more difficult because they are more distant and dimmer. However, since quasars share many properties with the lower-luminosity Seyferts, understanding Seyferts can provide important clues that will allow us to better understand quasars.

Several other subclasses and names of AGN are: radio galaxies, low-ionization nuclear emission-line region (LINER) galaxies, BL Lac objects and optically violent variables (OVVs), Narrow-Line X-Ray galaxies (NLXGs), and more (see Peterson 1997).

1.2 QUASARS

Quasars (Quasi Stellar Objects, abbreviated as QSOs)[1] are known for generating extraordinary luminosities (up to $10^{47}\,\mathrm{erg\,s^{-1}} \sim 2.5 \times 10^{13} L_\odot$) of order $\sim 10^2$ to 10^3 times higher than a normal luminous galaxy in volumes as small as $\sim 2 \times 10^{14}\,\mathrm{cm}$ ($\sim 3000 R_\odot$), where $L_\odot$ and $R_\odot$ are the solar luminosity and solar radius, respectively. Their radiation is emitted across the spectrum from x-rays to radio waves with a peak in the optical and ultraviolet (UV) bands shown in Figure 1. The vast amount of energy emitted over 7 orders of magnitude in frequency depends on many different physical processes (Koratkar & Blaes 1999). Strong radio emission comes from relativistic jets, which appear in approximately 10% of the quasar population, known as radio-loud quasars (de Vries et al. 2006). The infrared (IR) radiation is thought to arise from the reprocessing of UV emission by dust with a temperature in the range of 10–1800 K and at a range of distances from the central UV source. The optical/UV photons which contribute to the main energy production mechanism of a quasar is thought to arise from an accretion disk (AD), which is the spectral region that I will mostly be discussing in this thesis. The x-ray emission can be interpreted as Compton up-scattering of optical/UV photons by hot or nonthermal electrons somewhere in the central engine, possibly a hot, magnetized corona above the disk. Although detailed mechanisms of energy generation are unclear, those emitting regions can vary in size from scales of $\sim 10^2$ light-seconds for emission of high energy radiation to as large as an $\sim 1\,\mathrm{Mpc}$ scale for extended radio emission.

The optical/UV continuum emission accounts for about one-third of the total energy of a quasar. This emission is generally believed to arise from a rotating AD surrounding a SMBH of typically $\sim 10^8 M_\odot$ (e.g., Lin & Papaloizou 1996; Ulrich et al. 1997; Mirabel & Rodríguez 1999). When the gas in the AD spirals in toward the central SMBH, it loses gravitational energy due to frictional forces (i.e., viscous forces), and the energy is converted into kinetic energy and radiation (Rees 1984). Friction (i.e., viscosity) in the AD causes the emitting regions to become very hot, with temperatures of $\sim 10^5 - 10^6\,\mathrm{K}$, and it is able to

[1] Note that the word "quasar," traditionally, was used only for the radio-loud sources, while radio-quiet quasars were known as QSOs. It is becoming more common now to use quasar as a general term to refer to both types, and that practice is followed in this thesis.

emit radiation in x-rays. This process can convert about 10% of the rest-mass energy into radiation (Raimundo et al. 2012).[2] The observed optical/UV continuum emission can be explained by multi-temperature blackbody emission from the AD, with the emission peak in the far-UV region between 900 Å and 1100 Å (e.g., Malkan 1983; Czerny & Elvis 1987; Wandel & Petrosian 1988; Laor 1990). In spectral data, this nonstellar continuum flux can be fitted over a limited wavelength range by a simple power law of the form $F_\nu \propto \nu^{-\alpha}$, where F_ν is the monochromatic flux at frequency ν. The spectral index α is determined differently for each wavelength range. In quasars, for example, the indices are 1–1.2 in the IR range, 0.3–0.7 in the optical/UV, and 0.9 at hard x-rays. For the radio-quiet and radio-loud quasars, the spectral indices in the radio bands spread widely in the range of 0–1 (Sanders et al. 1989).

One of the prominent features for quasars is the BEL spectrum that is not seen except in the hottest stars as shown in Figure 2. The lines are very strong in emission, featuring the elements of hydrogen (the Balmer and Lyman series are prominent), helium, carbon and magnesium, among others. The lines are also very broad, with FWHM velocities normally in the range of $\sim$ 1000–15,000 $\mathrm{km\,s^{-1}}$; these large velocity widths for the line emitting gas were recognized very early on (Greenstein & Schmidt 1964). These lines are produced mainly by permitted transitions and can show superposed narrow components with FWHMs of $\sim$ 200–2000 $\mathrm{km\,s^{-1}}$ plus emission due to narrow forbidden transitions. Both the narrow and broad features of emission lines are also seen in the Seyfert galaxies. As noted earlier, the Seyfert galaxies are historically classified into two types: Type 1s show both broad and narrow emission lines, in a similar manner to quasars, while all of the line emission in Type 2s is narrow.

Together with the emission features are broad absorption lines (BALs) which appear in at least 10% of optically-selected quasars (Turnshek 1984b; Weymann et al. 1991), as shown in Figure 3. They are characterized by distinctive absorption troughs arising from resonance lines of various ions and they are blueshifted (outflowing) with respect to their associated BELs. There is general agreement that they are intrinsic to the quasar and caused by gas within the quasar itself, with outflow velocities up to thirty and possibly sixty thousand

[2]The efficiency of accretion η is defined by $L_{disk} = \eta \dot{M}_{acc} c^2$, where L_{disk} is the total luminosity of the disk radiation, $\dot{M}_{acc}$ is the accretion mass and c is the speed of light. The efficiency of accretion in quasars is often assumed to be $\eta \sim 0.1$.

kilometers per second relative to the emission line redshift. Some are often described as P Cygni profiles,[3] by analogy to similar features seen in stars which eject material toward the observer.

Analyses of such intrinsic absorption systems have suggested that there is a link between the absorbing gas and the BELR. Detailed studies of broad absorption line quasars (BALQSOs) could provide diagnostic tools for investigations of the nuclear region of a quasar (Wampler et al. 1995; Turnshek et al. 1996). However, these regions are unresolved with present-day imaging detectors. On the other hand, thanks to spectroscopy we are able to understand some of the properties of quasars. The spectroscopic results can be used to provide constraints on realistic quasar models. However, to date, theoretical models have been unable to explain all of the observational phenomena, but the deficiencies of currently proposed models will not be fully discussed in this chapter. Readers who are interested can refer to a summary presented in Table 1 of Sulentic et al. (2001).

1.2.1 Broad Emission Lines

It has been recognized for a long time that both broad and narrow emission lines coming from both high- and low- ionization species are present in Type 1 Seyfert galaxies and quasars. These emission lines from elements with various ionization states exhibit diverse spectroscopic properties. The lines of Lyα λ1216, CIV λ1549, HeII λ1640 and HeII λ4686 are considered to be examples of high-ionization lines, with ionization potentials > 50 eV; the HI Balmer lines, FeII multiplets, MgII λ2800 and the CaII IR triplet are examples of low-ionization lines, with ionization potentials < 20 eV.

The BEL profiles in quasars exhibit a wide variety, and investigations of their shapes can provide information about the conditions of the emitting gas surrounding the SMBH, and hence the structure and kinematics of the BELRs. Results on their properties include:

1. BELs with widths of several to many thousands of kilometers per second, indicating that the BELRs are in the vicinity of a central SMBH (Boroson & Green 1992);

[3] There are two components to a P Cygni spectral line profile in a star: the redshifted emission is from the Doppler-broadened expanding shell, and the blueshifted absorption feature is from material expanding towards the observer.

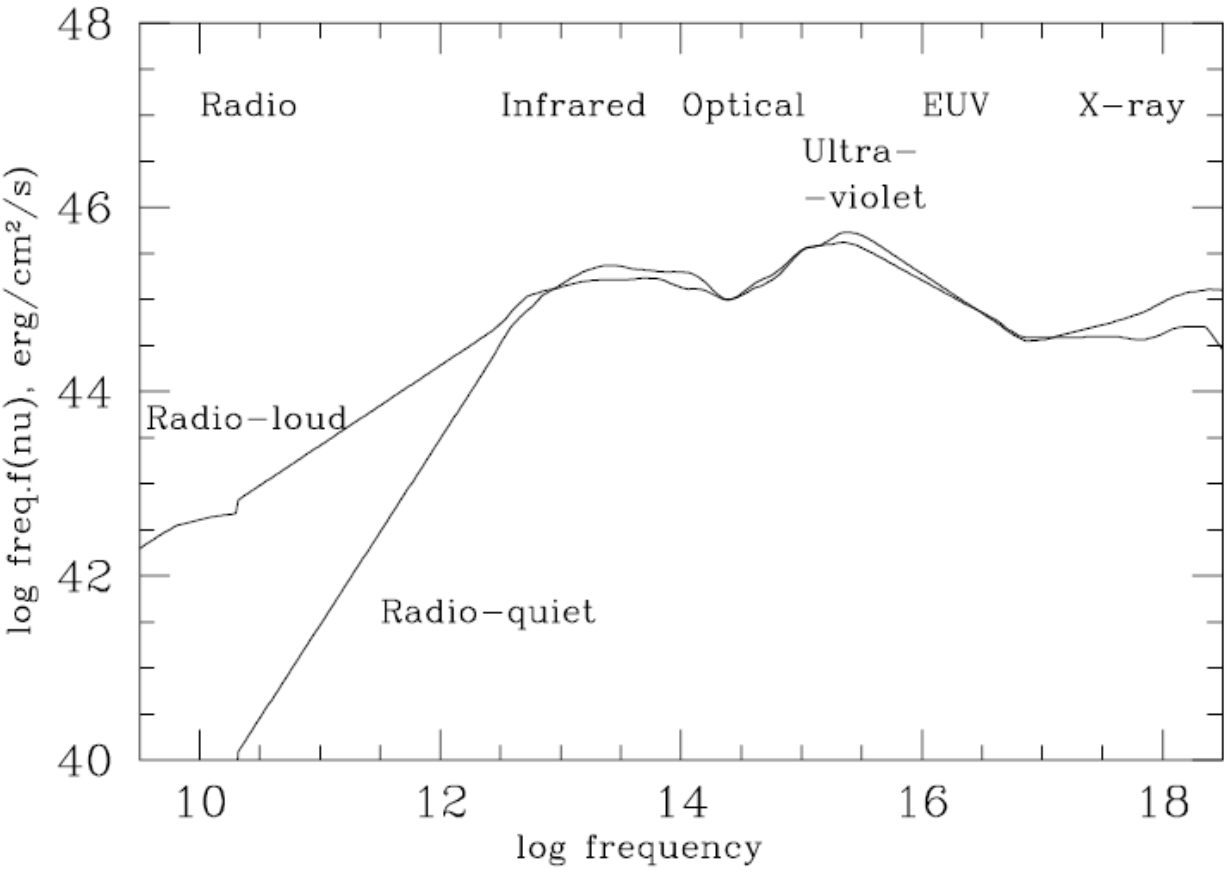

Figure 1 The radio to x-ray spectra of radio-loud and radio-quiet quasars (Elvis et al. 1994). The two curves are almost the same, except for the factor of ~ 100 divergence in the radio band.

2. Generally smooth BELs, suggestive of a continuous flow and consistent with a covering factor <10%, and sometimes a broad flat structure at the base of the emission, suggestive of a wind associated with a disk;

3. Often a blueward peak in high-ionization BELs (e.g., CIV) which is usually offset to lower redshift relative to low-ionization BELs (e.g., MgII) by hundreds of kilometers per second, suggesting the possibility of electron scattering (Kallman & Krolik 1986; Ferrara & Pietrini 1993), a line-of-sight orientation effect, or radial motions of the line emitting gas together with obscuration of the redward emission line flux (Richards et al. 2002);

4. Sometimes a significant asymmetry with excess flux in the blue wing of, e.g., the CIV

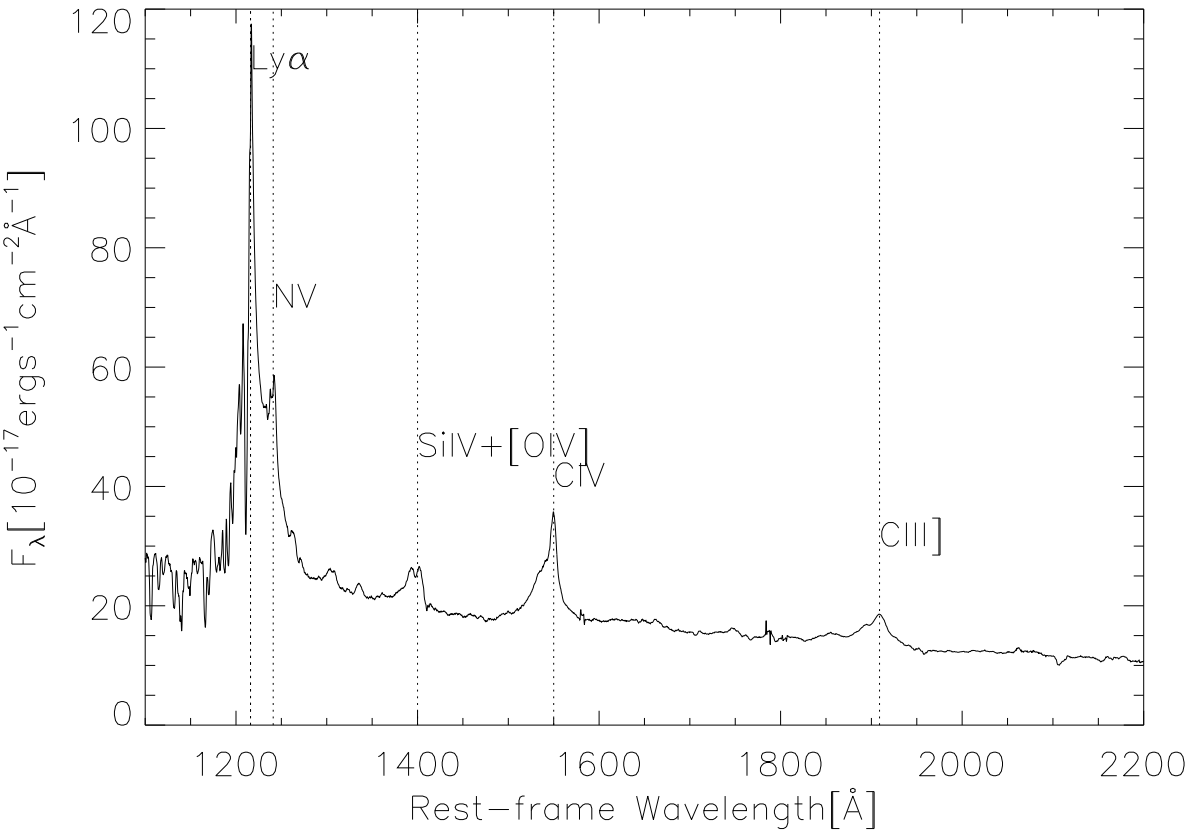

Figure 2 Rest frame spectrum of SDSS J004806.06-010321.6.

BEL for radio-quiet quasars, but either a red or a blue excess in radio-loud quasars, with the interpretation that a blueward asymmetry is associated with an accretion disk, while a redward asymmetry is related to a strong radio jet (Richards et al. 2002).

5. Electron number density constraints based on the lack of [OIII] forbidden BELs and the presence of CIII] semi-forbidden BELs in quasar spectra, suggesting that the BELR gas has electron number densities in the range $10^5 \leq n_e \leq 10^{10}\,\mathrm{cm}^{-3}$.
6. Variability on time scales of days to weeks to months, with a luminosity dependence, which is used to constrain the distance between the BELR and the inner ionizing continuum source (Peterson 1997).
7. Being dominated by the gravitational potential of the central black hole and, with the assumption of Keplerian motion, is used to estimate central black hole masses; however, some observational results indicate that BELR gas could be in random or disk-like orbits,

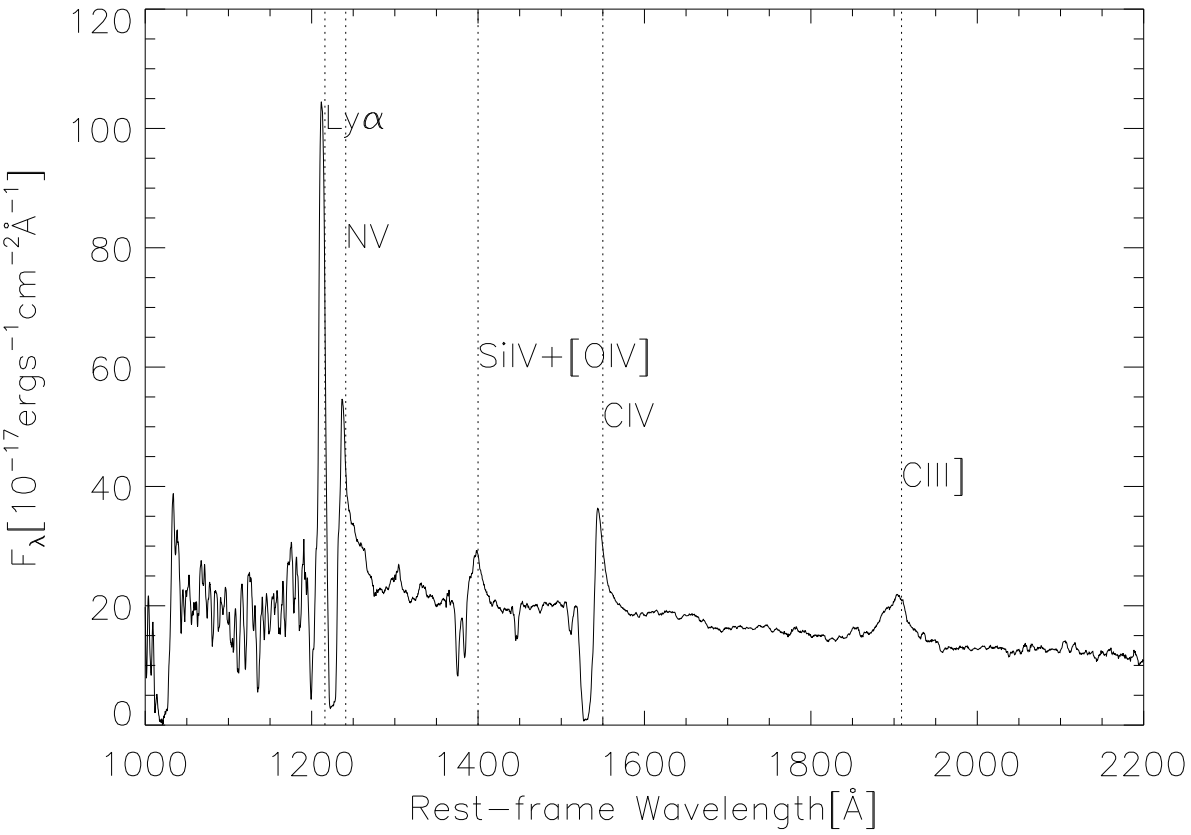

Figure 3 Rest frame spectrum of SDSS J131912.4+534720.8.

and some of the gas could be inflowing or outflowing, so the dynamics of the BELR is still uncertain.

Analysis of the line features can place constraints on models of the geometry and kinematics of BELRs. To explain the complex morphology of the observed BEL shapes, different models have been proposed (e.g., binary BH models, cloud models, disk-wind models, etc.) (Sulentic et al. 2000). The broad line widths are due to the Doppler effect rather than other broadening mechanisms (e.g., broadening due to collisions, natural broadening, etc.). Therefore, accretion disk models with Keplerian rotation have often been considered as explanations for the BELs. The models fit the widely accepted AGN paradigm that the central engine consists of a massive black hole fueled by an accretion disk. However, for a simple model with a disk geometry, a double-peaked feature in the BEL profile will be observed

unless the disk is viewed nearly face-on. But there is insignificant evidence for double-peaked signatures in the BEL profiles of quasars. Single-peaked line profiles are generally observed, and it is possible to produce this using a disk-wind model with a Keplerian disk (Murray & Chiang 1997). Single-peaked BEL profiles can also be explained using other models, but only if two or more kinematically and physically different emission regions are present (see, e.g., Marziani et al. 1993; Romano et al. 1996; Popovic et al. 2001; Popović et al. 2002, 2003, 2004; Bon et al. 2006; Ilić et al. 2006; Hu et al. 2008; Bon et al. 2009a,b). In these models, other line-emitting components, which add to emission from the disk component, have been considered as explanations for the single-peaked BEL profiles with wide widths. Even though such models are flexible enough to explain different complex BEL shapes, the physical parameters of individual components are not easily constrained. Moreover, analyses of single-peaked BELs often show that shoulder-like profiles in the wings of the line could be a fingerprint of BELs coming from an accretion disk (Popović et al. 2003; Eracleous & Halpern 2003; Strateva et al. 2003). This supports both scenarios that the optical/UV BELs originate either at the base of the disk-wind, or in multiple emission regions where one of them is from disk broad emission lines. Therefore, further exploration of the two models, together with observational constraints, are keys to obtaining a clear picture of the geometry of BELRs.

Ideas about the kinematics of the BELs is less concrete. The BELR gas can be in chaotic virialized motion, Keplerian orbits, radiatively-driven outflows, infall, and various combinations of these possibilities. Velocity-resolved reverberation mapping provides information about the kinematics of the line emitting regions. One study demonstrated that the BELR was not outflowing but gravitationally bound instead, but this is in conflict with other evidence for outflow, especially the blueshifting of the high-ionization lines (Gaskell & Goosmann 2008). The most widely adopted solution is the two-component model, which assumes that the BELR has two components with different kinematics: a gravitationally-bound low-ionization BELR, and a radially-outflowing high-ionization BELR. These two components have often been associated with "disk" and "wind" components. Alternatively, the accretion disk-wind model (Murray & Chiang 1997; Proga et al. 2000) suggests that the disk-wind component is the single origin of BELRs, where the high-ionization BEL gas is

predominately rotating at the base of the outflowing wind, which causes the blueshifting feature. This outflow could be covering a large range of disk radii (Murray et al. 1995), or mostly covering a narrow radial range (Elvis 2000), with the specific suggestion that the BELR forms at the radius where the gas pressure becomes comparable to the radiation pressure. The wind outflow is expected to be either radiation pressure driven, or magnetically driven. As different dynamical models affect the line profiles and the location of BELRs, they should be tested extensively.

Observationally, reverberation mapping is an important means to provide information concerning the spatial distribution of the line emitting gas, by using light echoes of BELs created by continuum variations. It is well known that the BELs are produced mainly by photoionization, followed by collisional excitation or recombination processes, which produce the emission lines. Changes in the continuum fluxes (treated as ionizing fluxes) give rise to changes in the BEL fluxes with a light travel time delay. Therefore, the distance of BELRs from the central source of ionizing radiation can be estimated. The response of line flux variations to ionizing continuum variations appears in not only the high-ionization BELs but also the low-ionization BELs. Since the high-ionization BELs respond faster to continuum variations than low-ionization BELs, there is clear evidence that the high-ionization BELRs are closer to the central ionizing source than the low-ionization BELRs. The absence of variations for narrow emission lines, indicates that the narrow line emitting gas is farther out from the central ionizing source. As such, all this observational information provides constraints on the distance between the different emitting regions and the central source of ionizing radiation. Details will be discussed in Chapter 3. Line profile variations are also observed in some sources (e.g., Gilbert et al. 1999), and this topic will be discussed in Chapter 4.

1.2.2 Broad Absorption Lines

Recent studies show that BAL quasars/QSOs form $\sim$ 15-40% of the quasar population (Hewett & Foltz 2003; Reichard et al. 2003; Trump et al. 2006; Dai et al. 2008; Stalin et al. 2011; Allen et al. 2011). They are characterized by the presence of broad absorption lines nor-

mally spreading over 5000–20,000 $\mathrm{km\,s^{-1}}$ but sometimes higher (Green et al. 2001). Quasars are classified as having BALs when they have contiguous absorption over $>2000\,\mathrm{km\,s^{-1}}$ at absorption depths >10% below the continuum level (Weymann et al. 1991). These are the classical BALs, and they cover a wide range of ionization. The BALs are further divided into groups based on the characteristics of the gas producing the BAL troughs: high-ionization BALs (HiBALs) contain strong, broad absorption troughs of highly ionized species (e.g., CIV, OVI and NV); low-ionization BALs (LoBALs), in addition to the standard absorption lines seen in HiBALs, contain absorption from low-ionization species (e.g., MgII, AlII and AlIII); a small subset of LoBALs with excited-state FeII or FeIII absorption are termed FeLoBALs (Wampler et al. 1995). While the LoBALs comprise about 15% of the BAL population (Hamann & Sabra 2004), only 13% of the LoBALs are FeLoBALs, which are about 1% of the total BAL population. As these FeLoBALs are very rare, they are not a well studied population of BALQSOs.

In general, BALQSO properties are as follows:

1. Blueshifted BALs with respect to associated BELs, but normally not outflowing to velocities beyond $\sim 20,000 - 30,000\ \mathrm{km\,s^{-1}}$, i.e., an outflow speed of $0.1c$ (Hewett & Foltz 2003);
2. Saturated and non-black absorption troughs in some cases, indicating partially covered continuum regions by some of the absorbers (Arav et al. 1999);
3. Appearing in the spectra of approximately 15 to 40% of optically-selected quasars (Haggard et al. 2012), and consistent with a viewing-angle effect;
4. Occultation of the Lyα BEL by the absorption trough due to NV, indicating that the outflow is launched from a region roughly cospatial with, or farther out than, the BELR (Turnshek 1984a; Turnshek et al. 1988).

1.3 STANDARD MODEL

The observations mentioned in previous sections gave rise to what has become the standard model for AGN. While this working model is still not completely established, it describes

many of the observations and represents a broad consensus among researchers in the field. The model includes a black hole which is fed by accretion through an accretion disk. The release of gravitational energy by the accreted material can roughly explain the observed continuum emission, in luminosity and spectral energy distribution. The direct clue to physical conditions in the central regions is the strong continuum emission and the BELs which originate farther out, as evidenced by the studies of continuum and BEL variability, and the deduced time lags between them. The small size of such "central engines" is consistent with the short variability time scale. For a review of this model see, e.g., Blandford (1990); Antonucci (1993); Peterson (1997); Netzer (1999).

The standard model provides a crude estimate of the location of the observed continuum and BELR, which is believed to be a function of the source luminosity. Starting from the central back hole of $\sim 10^8 M_\odot$, the x-ray and UV continuum radiation is primarily emitted within a radius of $\sim 10^{-3}\,\mathrm{pc}$. Moving out to the distance of $\sim 0.1\,\mathrm{pc}$, we find the region emitting the BELs. Farther out to the distance of $\sim 100\,\mathrm{pc}$, we find the region where the narrow emission lines (NELs) are produced. At these distances, photoionization models and the relative strength of various emission lines suggest that the gas temperature in the BELR is of order $1 - 3 \times 10^4\,\mathrm{K}$ and the particle density is $n \leq 10^{10}\,\mathrm{cm}^{-3}$. The typical gas density in the narrow emission line region (NELR) is $10^3 - 10^6\,\mathrm{cm}^{-3}$ and the gas temperature is similar to that in the BELR. Under these conditions, the large widths of the lines cannot be explained by thermal motion since the sound speed in a $10,000\,\mathrm{K}$ gas amounts to only $\sim 10\,\mathrm{km\,s}^{-1}$. A reasonable explanation for the large widths of the emission-lines is Doppler broadening due to bulk motion of gas.

As the BELR is too small to be resolved by any astronomical observations, the main source of information about it comes from spectral line studies. The chemical composition of the gas in the BELR and the NELR is roughly known from spectral line studies, although the analysis of the broad and narrow emission lines is complicated and somewhat uncertain due to the large optical depth in many lines. In the standard model, the general ideas about the BELR structure involve "clouds" that are simply large gas concentrations. Some models suggest giant stars as the clouds in the BELR, while others consider arbitrary gas condensations. The clouds are moving around the black hole in a velocity pattern that is

yet unknown. As for the NELR, the model suggests gas clouds that are less dense and move slower, which explains the narrowness of the lines.

The standard model explains that the gas giving rise to the emission lines is photoionized by the central radiation which interacts with atoms and ions in the BELR and the NELR. Photoionization can explain most of the emission line fluxes and line ratios. Continuum luminosity changes are explained as changes in accretion rate onto the black hole. The variable photoionizing flux results in BEL flux variations, with a time delay characteristic of the size of BELR, i.e., the light travel time between the central source and the BELR. Those changes are not seen in the NELs since the NELR is three orders of magnitude or more larger.

There are attempts to unify several AGN subclasses into the standard model, which is referred to as The Unified Scheme. This scheme seems to be successful, particularly in unifying Type 1 and Type 2 Seyfert galaxies. According to this scheme, a torus (an optically thick doughnut-shape ring of cold gas and dust) surrounds the central regions and obscures the central continuum source and BELRs when the viewing direction intercepts the torus. Such orientation effects can successfully explain the observed properties of different types of AGN. When observing the AGN from the polar direction, and the obscuring torus is oriented face-on, both the central continuum and lines emitted by the BELRs and NELRs are seen, and the object appears as a Type 1 AGN. In contrast, when the AGN is observed from the plane of the torus, and the torus intercepts the observer's line-of-sight, both the central core and the BELRs are hidden. As a result, only NELs are present in the optical spectrum, and the object is classified as a Type 2 AGN. This scheme is also confirmed by x-ray observations of Type 2 AGN, since x-rays emitted from the core penetrate the torus and provide a clear view of the center at high energies. Moreover, the scheme attempts to unify radio-loud and radio-quiet sources, assuming that the former are associated with relativistic jets which are responsible for the radio emission.

A sketch shown in Figure 4 demonstrates that different viewing angles toward the central region is a crucial element for explaining different types of AGN. However, the model is far from being complete and there are many features that are currently unclear. For example, there is uncertainty about the distance scale of the BALR.

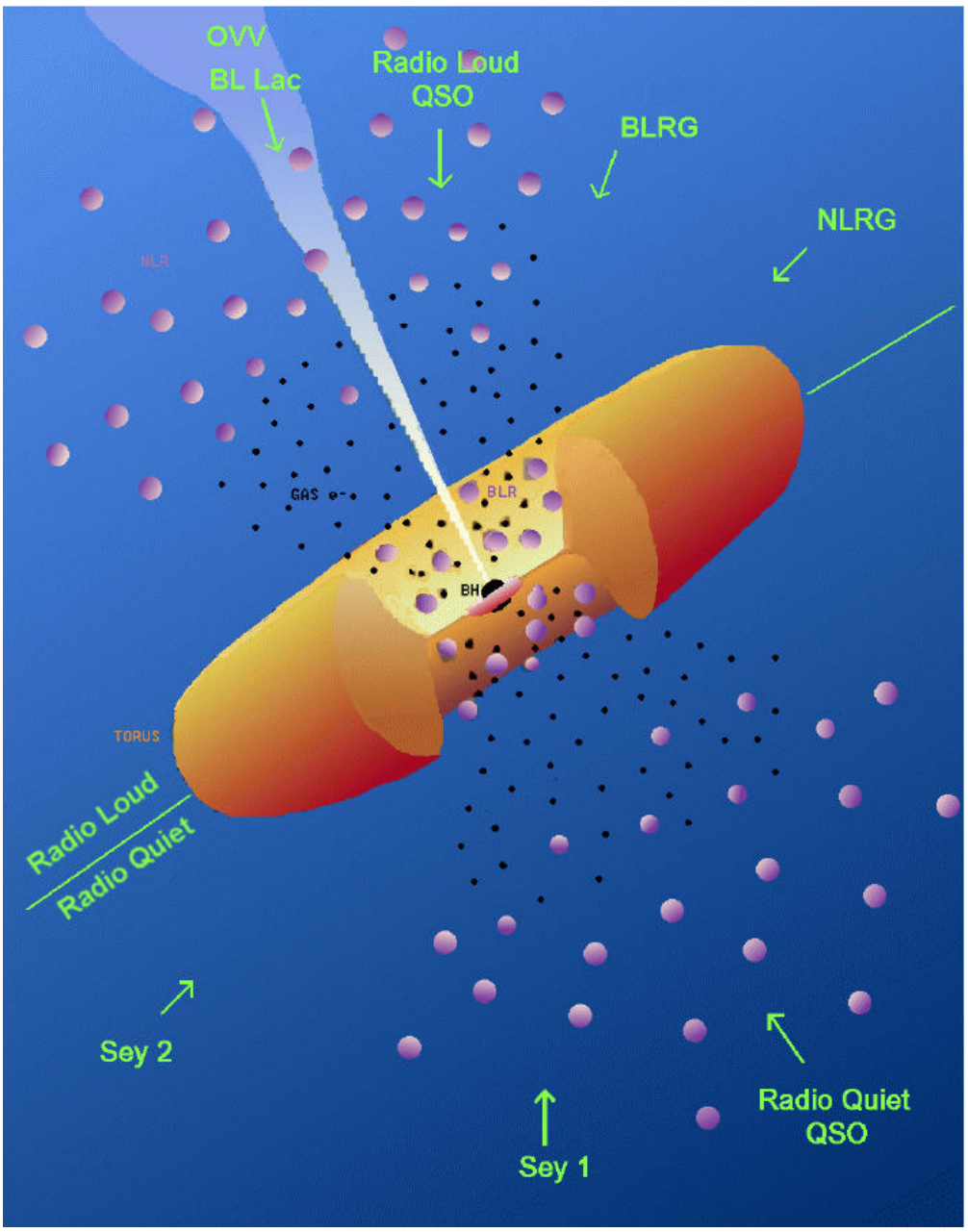

Figure 4 A sketch showing a summary of AGN classification according to the unified model illustrated in the text. Adapted from Urry & Padovani (1995).

1.4 MOTIVATION

As mentioned above, although the continuum region is well understood, specifying the properties, location and kinematics of the emission and absorption line regions in AGN has been problematic. Note that constraints on the location of the BELR come from reverberation mapping but the kinematics are not well constrained. However, the line-of-sight kinematics of the BALR is observable, but its location is not well constrained. As the BALRs are outside the BELRs, the minimum distance of the BALR is constrained by the reverberation mapping distance of the BELR. There has been a wide range of inferred BALR distances, ranging from 0.01 pc to tens of kpc. Given knowledge of the observational phenomena, the theme for the research in this thesis is to test and constrain models for the geometry, size scale, and physical conditions of the BELRs and outflowing BALRs in quasars.

It is well known that spectral analysis can reveal some of the physical properties of quasars. In the rest-frame optical/UV spectra of quasars, the cores of the strong absorption components are much deeper than some of the continuum plus BEL flux levels, which indicates that the absorption components exist outside the BELRs. In particular, the absorption trough of NV can cover and attenuate the Lyα BEL, as the separation of these lines happens to be roughly 6,000 $\mathrm{km\,s^{-1}}$. This specifically indicates that the NV BALR lies outside the Lyα BELR. Hence, with an estimate of the BELR distance, the minimum distance of the BALR can be established.

The reverberation mapping technique can be used to measure the distance of the BELR (e.g., Kaspi et al. 2007; Peterson 1993). BELR gas is photoionized by the x-ray and UV continuum emission from the inner region of the AD, and then as the gas cools it radiates line emission due to collisional excitation and recombination processes, including Lyα, NV and CIV BELs (e.g., Davidson & Netzer 1979; Mathews & Capriotti 1985). Consequently, when the AD continuum emission varies in strength, one can observe echoes of those variations in the BELs with a time lag. The time lags can be used to determine the distances between the central continuum source and the high- and low-ionization BELRs. So far, the reverberation mapping technique is relatively well established for the average luminosity of an AGN. Using this result, the distance of the BELR is inferred to be at ~ 0.1 pc for a high-luminosity quasar

with a luminosity of $10^{47}\,\mathrm{erg\,s^{-1}}$.

Since the BALR lies outside the BELR as discussed above, the minimum distance of the BALR is constrained by the reverberation mapping distance of the BELR. However, the maximum distance of the BALR from the central source is more difficult to constrain. For the standard model of a quasar, a black hole with a mass of $10^8 M_\odot$ has a radius of about 3×10^{11} m, and this indicates that the continuum emission from the AD occurs at $1-30\times10^{12}$ m. The reverberation mapping studies then suggest that the BELRs are located at $2 - 20 \times 10^{14}$ m. The dusty torus has its inner radius at about 10^{15} m. The narrow line region extends to $10^{16} - 10^{18}$ m, and radio jets in radio-loud quasars have been detected at $10^{15} - 10^{22}$ m (Urry & Padovani 1995). As such, it is often thought that BALRs may be relatively close to the quasar nucleus at $< 3\times10^{16}$ m, although direct observational evidence for this is not very strong.

There has been a wide range of inferred distances for the BALRs, recently ranging from 0.01 pc to tens of kpc. At present, the locations of the BALRs in quasars are not reconciled. There are currently two main theories for the BALRs. One theory involves variants of a wind driven off the accretion disk or something related to the accretion disk. Murray & Chiang (1997) found that for a quasar with $\sim 10^8 M_\odot$ a wind can be launched at $\sim 10^{-3}$ pc from the central engine and that this was the origin of the BELR and BALR. Elvis (2000) proposed a bi-conical wind model viewed at different angles that will explain the many varieties of complex BAL features seen in quasars. Another possibility is a wind formed by photoionized evaporation from the inner edge of the torus (Krolik & Kriss 2001), which would locate it at a few parsecs from the continuum source. However, some recent observational studies tend to show that the BALRs could be at galactic-scale distances $\geq$3 kpc. Due to such large distance determined, it is possible that such an outflow can be connected with galactic wind instead of an accretion disk-wind (Arav et al. 2012). Furthermore, more evidence suggests that very low-ionization outflows (e.g., CII and SiIII) take place over a large range of scales in quasars, possibly from as close in as 1 pc out to tens of kiloparsecs. There appears to be very little correlation of outflow velocity with distance from the AGN core. Partial covering of the background source plays an important role in all cases studied, indicating very small scale structure in the outflow, independent of the size scale of the outflow itself. Summaries

of inferred distances and other physical parameters of the absorption outflows are presented in Table 10 of (Dunn et al. 2010) and Table 6 of (Edmonds et al. 2011).

With all of these discrepancies in estimates for BALR distances, as well as the lack of direct evidence for the origin of the BALR, the work in this thesis attempts to build an empirical model for the inner structure of a quasar which is consistent with observational results (from spectroscopy and reverberation mapping) on the continuum region, the BELR, and the BALR. The geometries, kinematics, and size scales of the various regions will be considered. The results should clarify our current understanding of the inner structure of a quasar.

1.5 STRUCTURE OF THE THESIS

Since the process of generating continuum emission from an AD is well understood, the main work of this thesis involves specification of the empirical quasar model as it applies to the geometries, size scales, and other physical properties of the BELRs and BALRs. In particular, in Chapter 2 I present the development of a hydrodynamic code for accretion disk winds, in order to investigate the dynamics of the BELR and BALR from first principles. However, the formulation does not employ magnetic fields, which may be important. In Chapter 3 I describe the principle of reverberation mapping which uses variability to determine the distances of BELRs from the central ionizing source. How these results constrain the masses of SMBHs in quasars is also considered. The reverberation mapping results for low-luminosity AGN are well established, and the locations of the Lyα and CIV BELRs are known to be similar. In contrast, these results are ambiguous for high-luminosity, high-redshift quasars due to observational difficulties. For example, Kaspi et al. (2007) reported on a reverberation mapping study using the Lyα and CIV BELs for some luminous quasars, but they were unable to report a positive result to derive a Lyα BELR distance. To expand the distance sample to high-luminosity, high-redshift quasars, I verified the variability of Lyα and CIV BELs using two-epoch quasar spectra from the Sloan Digital Sky Survey (SDSS) in Chapter 4. This study shows there is a strong correlation between Lyα BEL variability and CIV BEL

variability, suggesting that these BELRs are at similar distances from the central source in high-luminosity, high-redshift quasars. In Chapter 5, using the derived BELR reverberation mapping distances, I define the three main components of the empirical model: optical/UV continuum emission from the AD, the BELR originating from an accretion disk-wind, and the BALR. For the optical/UV continuum emission I use multi-temperature blackbodies to model the AD and calculate the continuum emission flux, including taking into account relativistic effects. The BELs are computed by adopting Murray et al. (1995) disk-wind model, in which a wind is launched from a rotating AD and the escape probability of line photons depends on how the wind is viewed. For the BALRs, I use observational results mainly derived from the classical high-ionization BALs. In Chapter 6 I employ the empirical model with a set of reasonable parameters to analyze the size and the physical conditions of the BALRs. Lastly, I discuss the results and briefly note the importance of some future work in Chapters 7 and 8.

2.0 ACCRETION DISK-WIND MODEL

To investigate the formation of broad emission lines (BELs) and broad absorption lines (BALs), which are poorly understood, we adopt the Accretion Disk Wind (ADW) scenario. In these models a wind emerges from an accretion disk and accelerates rapidly in the radial direction due to UV radiation pressure from the inner disk region. The observed BELs are formed in the accretion disk chromosphere, while the BALs are caused by the disk wind and are only observed when the accretion disk is viewed along the wind nearly edge-on. The ADW model is very well motivated in comparison to alternative models. Therefore, the development of ADW models is essential for progress. Comparison of these model results with observational results will lead to a clearer understanding of models of quasars and their limitations. In addition, these models will provide constraints on the locations, physical conditions, and sizes of BELRs and BALRs. For example, if we find ADW models to be applicable, we will be able to determine reliable metal abundances of quasars, which would be a major breakthrough.

In this chapter, we attempt to study line-driven winds from luminous accretion disks using numerical methods to solve the 2.5-dimensional, time-dependent equations of hydrodynamics. In doing so we have accounted for the radiation force due to spectral lines using a generalized multidimensional formulation of the Sobolev approximation. We have adopted the formalism of the line-driven radiation force derived by Pereyra that have been used to calculate a white dwarf accretion disk wind with a steady wind solution (Pereyra et al. 2004). With the hydrodynamic code used in this study, we found that the local disk radiation can launch a wind from the disk and the inner disk radiation can drive the wind to reach terminal velocities. However, in contrast to Pereyra's results, our numerical simulations show the existence of an non-steady wind solution in every circumstance we have explored.

2.1 ACCRETION DISK-WIND SCENARIO

The ADW scenario has been proposed to explain the formation of BELs and BALs in quasars, which are primary observational characteristics of quasars. Approximately 15 to 40% of optically selected quasars exhibit blueshifted BALs with respect to the BELs in their spectra (Haggard et al. 2012). Some example spectra are shown in Figure 5 (Turnshek 1988). Many BALs display P Cygni type line feature like the ones in Figure 5; some present themselves as detached absorption troughs, and others present themselves as multiple absorption troughs; non-black saturation of the absorption troughs is sometimes due to velocity-dependent continuum coverage rather than the column density distribution in the outflows. The absorption feature blueward of the emission redshift shows that gas is flowing radially outwards with terminal speeds sometimes up to one tenth of the speed of light. It has generally been argued that most quasars possess such outflows, which cover a significant fraction of the sky as seen from the center of the accretion disk, and BALs are seen when an observer views along the outflow (Turnshek et al. 1980; Junkkarinen 1983; Junkkarinen et al. 1987; Hamann et al. 1997). The detection of both blueshifted and redshifted polarized light in the vicinity of the CIV line appears to be consistent with the outflow being nearly in the plane of the accretion disk (Ogle 1997). It has been claimed that the observed presence of multiple BAL troughs could be explained by viewing angles being close to the angle that separates the x-ray shielded region and the x-ray non-shielded region, or that they could be due to discontinuities in the ion balance of the wind caused by x-rays (Vilkoviskij et al. 1999).

The obvious source of a BAL outflow near the plane of the accretion disk is the disk itself. The high-velocity outflow suggests that it originates near the black hole, but it is located outside the region where the strong x-ray and UV continuum is produced. The question then arises as to how we observe very high luminosities in the x-rays and UV region on one hand, and on the other hand we observe BALs from moderately and highly ionized species that have been accelerated to one tenth of the speed of light. Quasars, in general, are observed to be vast emitters of soft x-rays (Mushotzky et al. 1993). With the powerful x-ray and UV emission, the outflowing material could be expected to be fully photoionized. To address this, the ionization balance in the BAL outflow is a key constraint for any model. To resolve

the overionization problem, two mechanisms have been proposed. One mechanism is to have the filling factors of AGN outflows less than unity, i.e., the outflowing gas would consist of many dense clouds. Another mechanism suggests that the filling factors are equal to unity but the winds are shielded from the powerful radiation by some highly ionized material located between the central engine and the winds (e.g., Krolik 1999). Most models overcome the overionization problem of the wind simply by assuming many high-density gas clouds. Moreover, the acceleration mechanisms for those high-velocity outflows need to be addressed in any model. Several forces to drive the outflows in AGN have been suggested, for example, gas pressure, magneto-centrifugal force due to an accretion disk, radiation pressure due to dust, and radiation pressure due to lines (Proga et al. 2000, and references therein).

Our understanding of the ability of the line-driving mechanism to produce powerful high-velocity winds is based on studies of winds in hot stars that radiate mostly in the UV continuum. By analogy with O-stars, the presence of strong blueshifted absorption together with an intense UV radiation field suggests that radiation pressure acting on resonance lines is the acceleration mechanism (e.g., Lamers & Cassinelli 1999, and references therein). The presence of the BALs themselves strongly indicates that substantial momentum is transferred from a powerful radiation field to the outflowing wind. With the inclusion of resonance lines, Castor et al. (1975, hereafter CAK75) showed that the effective line-driven radiation force can increase by several orders of magnitude above that due to electron scattering alone. On the other hand, the lack of structure on the thermal velocity scale (roughly 10 $\mathrm{km\,s^{-1}}$) suggests that the outflow is continuous rather than discrete, and that it is a steady flow based on the lack of observed velocity changes over time (Foltz et al. 1987; Turnshek et al. 1988; Barlow et al. 1992a; Barlow 1994; Hamann et al. 1997). In spite of the similarity of winds in stars and AGN, the accretion disk scenario is different from the stellar scenario in essential ways, including the role of rotation near a Keplerian accretion disk, the radial dependence of the disk temperature distribution, the increasing gravitational force on the disk atmosphere, the influence of the strong X-way flux from the inner disk, and the black hole. There is also the fundamental difference in geometry: stellar winds are to a good approximation spherically symmetric, whereas the winds in BAL quasars likely arises from a flattened disk and are, at best, axially symmetric.

Radiation driving on spectral lines is the most promising scenario for AGN outflows, and these line-driven disk-wind models have been proposed by several authors. The most representative ADW model is by Murray et al. (1995, hereafter MCG95). They studied a wind arising from the accretion disk at a small distance from the central black hole at $\sim 10^{16}$ cm mainly due to the local disk radiation. Afterward the wind is accelerated radially to high velocity by the radiation from the inner disk region. Since the presence of a steady flow is always observed, without radiation pressure the increment of gravity in the direction perpendicular to the accretion disk does not allow a steady flow to be generated (Pereyra et al. 1997). A key ingredient to the MCG95 model is that the central engine radiation is weakened by "hitchhiking" gas located between the central engine and the wind, providing a shielding effect on the wind. Otherwise the material in the ADW would be ionized to the point where the line radiation pressure would be negligible. The authors postulated the existence of hitchhiking gas, but they did not derive its origin from first principles. The authors demonstrated the role of this shielding gas on a 1-dimensional, time independent quasi-radial flow. If the detected phenomenon of BALs is a viewing angle effect, as suggested in the ADW scenario, one would expect to observe them only at viewing angles where the x-ray emission is absorbed, consistent with the wind being "shielded" from the x-rays. Furthermore, the ADW scenario is roughly consistent with BAL outflows covering ∼10% or more of the central continuum source, and thus could account for the percentage of observed BALQSOs within a unified picture (see Section 1.3). The authors also found that the ADW could account for BAL troughs of the P Cygni type, as well as the detached type.

The prominent BELs in the UV (e.g., OVI, Lyα, NV, SiIV, and CIV) are some of the defining feature of quasars, and they may also be associated with a high-velocity wind. In the MCG95 model, the authors suggested that the formation of the BELs would be in the accretion disk chromosphere. Through the time delay in BEL flux variation to continuum flux variation, the location, geometry and kinematics of the BELRs can be measured using so-called reverberation mapping studies (see Chapter 3). Instead of the larger distance of the BELR found in emission line cloud models, the MCG95 model found that the size sale of the BELR is consistent with reverberation mapping results for low-luminosity AGN like Seyfert galaxies (Korista et al. 1995, 1996). Furthermore, the MCG95 model demonstrates

the peculiar non-symmetric response seen in velocity resolved studies of the CIV BEL, namely that the red wing of the BEL responds faster than the blue wing to changes in the continuum (Chiang & Murray 1996). In the ADW scenario, the observed BEL widths would naturally be explained by the formation of BELs within a disk atmosphere, since the widths are roughly consistent with predicted Doppler broadening due to disk rotation.

The MCG95 model also successfully produces often-observed single-peaked BEL profiles. The authors presented the calculations of BEL profiles from the disk atmosphere, which included the velocity gradients associated with the wind emerging from the disk. They calculated radiative transfer effects coupled not only with velocity gradients due to disk rotation, but also coupled with velocity gradients due to the disk wind. They found that optically thick emission line profiles tend to be narrower than in the non-wind case, and they found that the BEL profiles tend to be single-peaked. These results not only presented an attractive explanation for the single-peaked emission lines seen in some high-inclination white dwarf accretion disks, but also showed that the often single-peaked BELs in quasars could be consistent with the ADW scenario.

So far it has been possible to model line-driven disk winds using 2-dimensional axisymmetric numerical hydrodynamical simulations (Pereyra et al. 1997, 2000; Pereyra & Kallman 2003; Proga et al. 1998, 1999, 2000). Most of these models have been applicable for low-luminosity white dwarf accretion disks; some of them have been extended to the study of high-luminosity quasar accretion disks. Since the steady nature of AGN wind flows is an observational characteristic, line-driven disk-wind scenarios can be testable through numerical simulations. There have been two opposing results in the AGN line-driven disk-wind models: one group believes that steady line-driven winds can be achieved; the other group has advocated to adopt one that incorporates additional physics (e.g., magnetic fields) in order to resolve the non-existence of steady winds by a line-driven radiation field alone.

For example, with regard to the launching of winds Proga and collaborators demonstrated unsteady outflows in their numerical results, obtaining large amplitude velocity and density fluctuations while the wind was launched from the disk. Once the wind is launched and it is fully exposed to the central source of radiation from the accretion disk, the outflow becomes steady in simulations (see Proga et al. 1998, 1999, 2000, for details). On the other hand,

Pereyra and collaborators concluded that radiation line driving can both launch a wind from the accretion disk and accelerate it (see Pereyra et al. 1997, 2000; Pereyra & Kallman 2003). As a result, the objective of this work here is to test for the existence/nonexistence of steady disk winds in the ADW scenario. We have used the methods developed by Pereyra to study the hydrodynamics of disk winds.

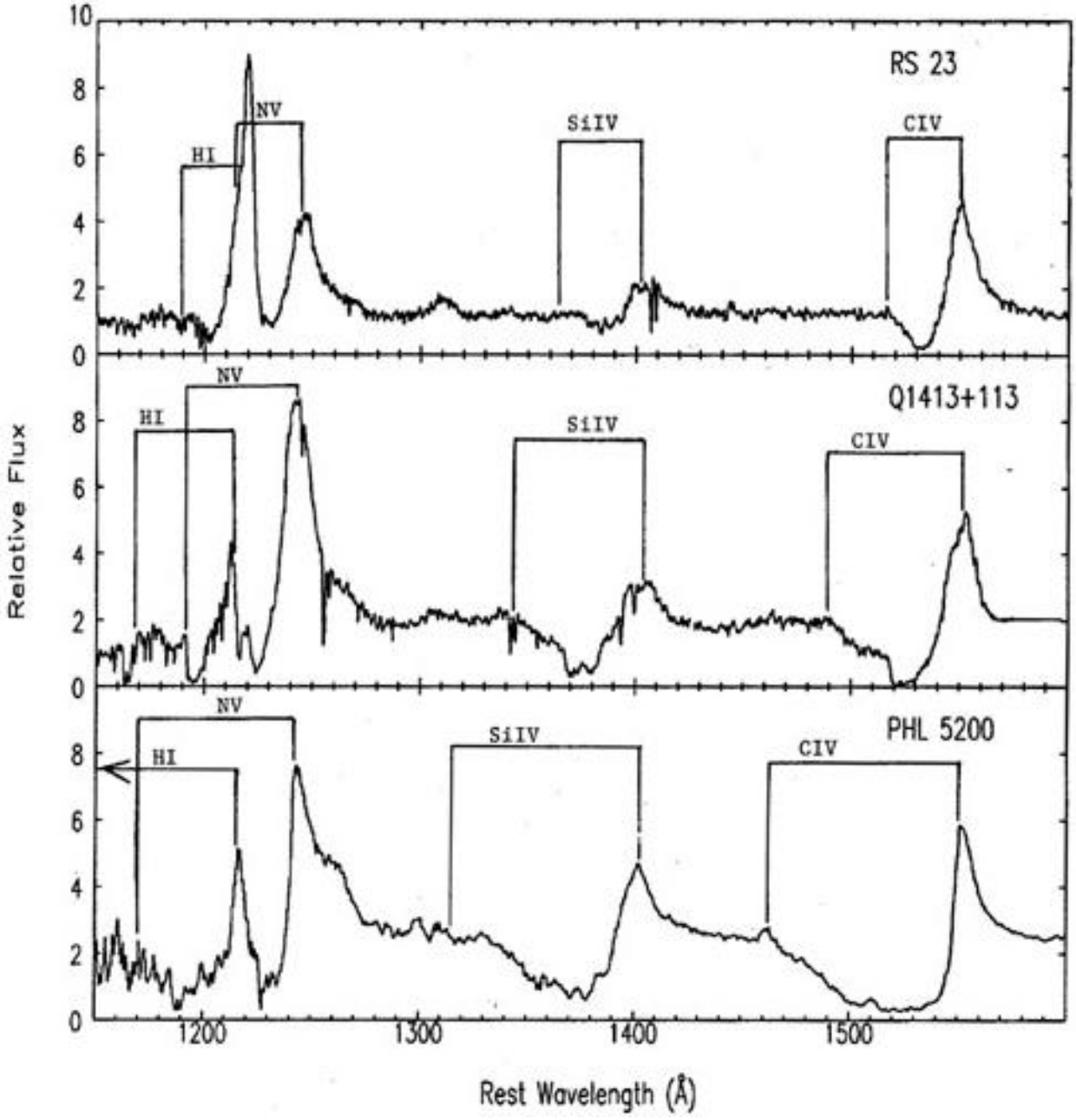

Figure 5 Rest frame spectra of 3 BALQSOs with P Cygni-like BALs (Turnshek 1988).

2.1.1 Accretion Disk Physics

The accretion of matter onto supermassive black holes (SMBH) can often be described by using the thin disk accretion model of Shakura & Sunyaev (1973). The potential energy is released in the form of radiation when matter spirals inwards. Because the accretion disk is optically thick, energy is dissipated and matter can remain cold, thus forming a geometrically "thin" disk. The turbulent viscosity is responsible for the transport of angular momentum outwards, which is often described through the standard $\alpha-$model.

Although the energy flux is generated through viscous dissipation, Shakura & Sunyaev (1973) showed that the accretion disk radiation and the disk temperature are radially dependent, with no knowledge of the physical nature of the viscosity α. The accretion disk would have an inner radius r_i, approximately equal to the innermost stable circular orbit (ISCO) of the SMBH; the outer radius r_o reaches out to where the gravity of the disk is unstable, which is on the order of a few thousand times the inner radius. For a non-rotating (Schwarzschild) black hole the ISCO is $r_i = 6r_g$, while for a rapidly rotating (Kerr) black hole the ISCO is roughly smaller by a factor of 5, i.e., $r_i = 1.23r_g$, where the gravitational radius is $r_g = GM_{BH}/c^2$, G is the gravitational constant, c is the speed of light, and M_{BH} is the mass of the SMBH. Assuming that the disk is in a steady state, the shear stress at the inner radius of the disk is negligible, and the matter in the disk follows Keplerian orbits, one finds that the energy emitted per area Q at radius r is given by Shakura & Sunyaev (1973):

$$Q = \frac{3GM_{BH}\dot{M}_{acc}}{8\pi r^3}\left[1 - \sqrt{\frac{r_i}{r}}\right], \tag{2.1}$$

where $\dot{M}_{acc}$ is the mass-accretion rate onto the SMBH. Using Equation 2.1, the luminosity produced by the entire disk can be obtained simply by integrating the energy emission per area Q over the two sides of the disk:

$$L_{disk} = 2\int_{r_i}^{r_o} Q\, 2\pi r dr. \tag{2.2}$$

Thus,

$$L_{disk} = \frac{GM_{BH}\dot{M}_{acc}}{2r_i}\left\{1 - \frac{3r_i}{r_o}\left[1 - \frac{2}{3}\left(\frac{r_i}{r_o}\right)^{1/2}\right]\right\}; \tag{2.3}$$

assuming $r_i \ll r_o$,

$$L_{disk} \approx \frac{GM_{BH}\dot{M}_{acc}}{2r_i}. \tag{2.4}$$

Assuming that the accretion disk is optically thick and geometrically thin, each element of the disk surface radiates roughly as a blackbody, and considering Equation 2.1, the radial temperature distribution of the disk yields

$$T = \left\{ \frac{3GM_{BH}\dot{M}_{acc}}{8\pi r^3 \sigma_S} \left[1 - \sqrt{\frac{r_i}{r}} \right] \right\}^{1/4}, \tag{2.5}$$

where σ_S is the Stefan-Boltzmann constant. The accretion disk temperature is radially dependent. The maximum temperature T_{max} is found at the distance $r \sim 1.2r_i$, where r_i is the inner radius of the AD. Thus, T_{max} is derived as

$$T_{max} \sim \left(\frac{\dot{M}_{acc}}{M_{BH}^2} \right)^{1/4}, \tag{2.6}$$

where T_{max} decreases with an increasing BH mass M_{BH} or a smaller mass-accretion rate $\dot{M}_{acc}$.

The amount of luminosity emitted from the disk is determined by the rate of mass accreted $\dot{M}_{acc}$ onto a BH which can be parametrized by the introduction of the accretion efficiency η:

$$L_{acc} = \eta \dot{M}_{acc} c^2. \tag{2.7}$$

This dimensionaless quantity measures how efficiently the rest mass energy of the accreted material is converted into radiation. It would be $\eta \sim 0.06$ for a non-rotating BH and $\eta \sim 0.4$ for a maximally rotating BH. Conventionally, the accretion luminosity should be compared to the Eddington luminosity L_{Edd} of the BH, which is the maximum possible accretion luminosity due to a spherically symmetric distribution of fully ionized, pure hydrogen gas. This occurs where the inward gravitational force by the central BH and the outward radiation pressure by electron scattering are balanced:

$$L_{Edd} = \frac{4\pi GM_{BH}m_p c}{\sigma_T}, \tag{2.8}$$

where m_p is the proton mass and σ_T is the Thomson cross section. Since evidence often shows that the luminosities of AGN and quasars are sub-Eddington, Equation 2.8 is still valid for these accreting systems with cylindrical geometries (Czerny et al. 1996). Thus, the accretion luminosity can be estimated as

$$L_{acc} = \lambda L_{Edd}, \tag{2.9}$$

where the Eddington ratio is expected to be $\lambda < 1$. The momentum of UV photons emitted by the accretion disk with L_{acc} accelerates the material with resonance line driving. By definition, when $L_{acc} > L_{Edd}$ the outward radiation pressure would exceed the inward gravitational force, and the accretion would be halted. When $L_{acc} < L_{Edd}$ the radiation pressure can effectively launch and accelerate powerful winds. In highly accreting AGN one can assume in a conservative way $\lambda \sim 0.1$. Few studies tend to indicate quasars accreting at super-Eddington rates (Collin et al. 2002).

In our numerical model, we use the local radiation flux in Equation 2.1 to compute the continuum and the resultant line radiation pressure forces, under the assumption of local blackbody radiation from the accretion disk. We employ the temperature distribution of the disk in Equation 2.5 to set a boundary condition for the wind near the disk surface, assuming that the temperature at the base of the wind is equal to the disk surface temperature for each radius.

2.1.2 Line Radiation Pressure Force

The dynamics of disk winds depend on a variety of physical process, including the outward radiative acceleration from line driving f_{rad}, and an effective inward gravitational acceleration, reduced by the outward continuum radiative force from free electrons scattering, and the rotational force arising from the fact that the material at the base of the wind is likely to be in a circular Keplerian orbit in the accretion disk. Considering a Keplerian accretion disk, the material is rotating about the SMBH near the equatorial plane, the radial gravitational forces are at balance with the centrifugal forces, and the wind must start off vertical. When the wind rises above the disk, the radiative force becomes dominant and they overcome the gravitational force of the disk such that the wind tends to flow radially.

The description of the radiation pressure force due to line driving is crucial to determine the kinematics of disk winds. We adopt the expression of the radiation force derived by Pereyra et al. (2000), as a steady disk-wind solution was obtained in their numerical stimulation. In their expression, the radiation emitted by an accretion disk includes not only the radiation pressure along the direction perpendicular to the disk but also the radiation pressure parallel to the disk.

The expression for the total line radiation force per mass of disk wind that we adopt is

$$f_{rad} = \frac{\sigma_T}{c} k \left(\frac{1}{\rho \sigma v_{th}} \left| \frac{dv_z}{dz} \right| \right)^{\alpha} [S_z(r,z)\hat{z} + S_r(r,z)\hat{r}], \tag{2.10}$$

where k and α are the line force parameters, ρ is the mass density, σ is the line opacity, v_{th} is the thermal sound speed, v_z is the component of the wind velocity in the z-direction, and S_z and S_r are the corresponding radiation flux components (the S_ϕ component is zero owing to the axial symmetry of the accretion disk). They are given by

$$S_z(r,z) = \int_{r_0}^{\infty} \int_0^{2\pi} \frac{Q(r')}{\pi} \times \frac{z^{\alpha+2}}{[(r^2 + r'^2 + z^2 - 2rr'\cos\phi)^{1/2}]^{\alpha+4}} r' d\phi dr' \tag{2.11}$$

and

$$S_r(r,z) = \int_{r_0}^{\infty} \int_0^{2\pi} \frac{Q(r')}{\pi} \times \frac{z^{\alpha+1}(r - r'\cos\phi)}{[(r^2 + r'^2 + z^2 - 2rr'\cos\phi)^{1/2}]^{\alpha+4}} r' d\phi dr', \tag{2.12}$$

where $Q(r')$ is the rate of emitted energy per unit area, at a given radius r, radiated by a standard disk, calculated through Equation 2.1.

A few approximations have been introduced to obtain the above expression for the line radiation force. For example, the Sobolev approximation is used to calculate the line opacity and the total line flux integral as evaluated by the formalism of CAK75. See Pereyra et al. (2000) for details. Equation 2.10 is obtained under the approximation that the velocity gradient of the wind is primarily in the direction perpendicular to the surface of the disk. This assumption is justified by the accretion disk winds in quasars which tend to initially flow in the direction perpendicular to the disk due to the local radiation pressure. Also, to make the computations manageable, the assumption of a velocity gradient primarily in the z-direction allows us to obtain an expression for the line radiation pressure that requires

the calculation of a spatial integration only once, rather than having to evaluate the spatial integrals at each time step.

Neglecting the radiation pressure parallel to disk, the total line radiation force per mass for disk winds in Equation 2.10 is simplified (Pereyra et al. 1997):

$$f_{rad} = \frac{\sigma_T F}{c} \left(\frac{z}{R}\right)^{\alpha} k \left(\frac{1}{\rho \sigma v_{th}} \left|\frac{dv}{dz}\right|\right)^{\alpha}, \tag{2.13}$$

where F is the total radiation flux in the direction perpendicular to the disk and z is the height above the disk. The authors noted that the radiation pressure force, at a given radius r, increases with height above the disk plane according to $(z/R)^{\alpha}$ where $R^2 = z^2 + r^2$. Such an increase is necessary, physically, if the wind is to overcome the increasing gravity in the form of $g = GM_{BH}z/R^3$. It is important to note that, unlike stellar atmospheres, the gravity at a given radius r increases with height from $z = 0$ up to a maximum at $z \sim 0.7r$. Gravity then decreases at greater heights, following a $1/z^2$ law at large distances above or below the disk. The authors suggested that changing ionization balance in the wind or changing obscuration due to the presence of "bulges" or bumps on the disk surface could produce similar effects.

For the continuum radiation pressure the total radiation flux is calculated throughout the disk wind

$$F = \oint \left[\int_0^{\infty} I(\hat{n}) d\nu\right] \hat{n} d\Omega. \tag{2.14}$$

Taking the source of radiation to be the accretion disk, we have

$$F_z(r,z) = \int_{r_0}^{\infty} \int_0^{2\pi} \frac{Q(r')}{\pi} \times \frac{z^2}{[(r^2 + r'^2 + z^2 - 2rr'\cos\phi)^{1/2}]^4} r' d\phi dr' \tag{2.15}$$

and

$$F_r(r,z) = \int_{r_0}^{\infty} \int_0^{2\pi} \frac{Q(r')}{\pi} \times \frac{z(r - r'\cos\phi)}{[(r^2 + r'^2 + z^2 - 2rr'\cos\phi)^{1/2}]^4} r' d\phi dr', \tag{2.16}$$

where F_z and F_r are the corresponding components of the radiation flux vector F originating from the disk (the F_ϕ component is zero owing to the axial symmetry of the accretion disk) and $Q(r')$ is the radiation emission per area of the disk calculated through Equation 2.1.

2.2 HYDRODYNAMIC MODEL

2.2.1 Equations

In our hydrodynamic model, we examine 2.5-dimensional radiatively-driven outflows in the accretion disks of quasars. The 2.5-dimensional model is the two-dimensional hydrodynamical equations of the wind in cylindrical coordinates with rotation in azimuthal symmetry. That is, we assume that the derivative of any physical variable with respect to ϕ is zero. The first spatial dimension is the height above the disk z which is treated with planar symmetry. The second spatial dimension is the distance between the center of the disk and the projection on the disk r which is treated with cylindrical symmetry.

For the general time-dependent simulations, the equations of hydrodynamics are as follows (Pereyra et al. 2000): the mass conservation equation,

$$\frac{\partial \rho}{\partial t} + \frac{1}{r}\frac{\partial (r\rho v_r)}{\partial r} + \frac{(\rho v_z)}{\partial z} = 0, \tag{2.17}$$

the momentum conservation equations,

$$\begin{aligned}
\rho\frac{\partial v_r}{\partial t} &+ \rho v_r\frac{\partial v_r}{\partial r} - \rho\frac{v_\phi^2}{r} + \rho v_z\frac{\partial v_r}{\partial z} \\
&= -\rho\frac{GM_{BH}}{(r^2+z^2)}\frac{r}{(r^2+z^2)^{1/2}} - \frac{\partial P}{\partial r} + \rho\frac{\sigma F_r(r,z)}{c} \\
&+ \rho\frac{\sigma S_r(r,z)}{c} \times k\left(\frac{1}{\rho\sigma v_{th}}\left|\frac{dv_z}{dz}\right|\right)^\alpha, \qquad (2.18) \\
\rho\frac{\partial v_\phi}{\partial t} &+ \rho v_r\frac{\partial v_\phi}{\partial r} - \rho\frac{v_\phi v_r}{r} + \rho v_z\frac{\partial v_\phi}{\partial z} = 0, \qquad (2.19) \\
\rho\frac{\partial v_z}{\partial t} &+ \rho v_r\frac{\partial v_z}{\partial r} + \rho v_z\frac{\partial v_z}{\partial z} \\
&= -\phi\frac{GM_{BH}}{(r^2+z^2)}\frac{z}{(r^2+z^2)^{1/2}} - \frac{\partial P}{\partial z} + \rho\frac{\sigma F_z(r,z)}{c} \\
&+ \rho\frac{\sigma S_z(r,z)}{c} \times k\left(\frac{1}{\rho\sigma v_{th}}\left|\frac{dv_z}{dz}\right|\right)^\alpha, \qquad (2.20)
\end{aligned}$$

and the energy conservation equations,

$$\begin{aligned}
\frac{\partial \rho E}{\partial t} &+ \frac{1}{r}\frac{\partial r\rho E v_r}{\partial r}\frac{\partial \rho E v_z}{\partial z} = -\frac{1}{r}\frac{\partial r P v_r}{\partial r} - \frac{\partial P v_z}{\partial z} \\
&- \rho\frac{GM_{BH}}{(r^2+z^2)}\frac{r}{(r^2+z^2)^{1/2}}v_r + \rho\frac{\sigma F_r(r,z)}{c}v_r \\
&+ \rho\frac{\sigma S_r(r,z)}{c} \times k\left(\frac{1}{\rho\sigma v_{th}}v_r\left|\frac{dv_z}{dz}\right|\right)^{\alpha} \\
&- \rho\frac{GM_{BH}}{(r^2+z^2)}\frac{z}{(r^2+z^2)^{1/2}}v_z + \rho\frac{\sigma F_z(r,z)}{c}v_z \\
&+ \rho\frac{\sigma S_z(r,z)}{c} \times k\left(\frac{1}{\rho\sigma v_{th}}v_z\left|\frac{dv_z}{dz}\right|\right)^{\alpha},
\end{aligned} \tag{2.21}$$

where P is the pressure, γ is the ratio of specific heats, ρ is the density, v_r, v_ϕ, and v_z are the corresponding velocity components in cylindrical coordinates, G is the gravitational constant, M_{BH} is the mass of the black hole, σ is the Thomson cross section per unit mass, c is the speed of light, v_{th} is the ion thermal velocity, S_z, S_r, F_z and F_r are the corresponding radiation flux components (see Equations. [2.11], [2.12], [2.15] and [2.16]). The total energy per unit mass is the sum of the kinetic energy and the internal energy:

$$E = \frac{1}{2}(v_r^2 + v_\phi^2 + v_z^2), \tag{2.22}$$

and the internal energy is related to the pressure through the equation of state of an ideal gas:

$$P = \rho e(\gamma - 1), \tag{2.23}$$

where e is the internal energy per unit mass. Note that the centrifugal and Coriolis forces appear naturally under cylindrical coordinates as the third term of the left-hand side in Equation 2.18 and the third term of the left-hand side in Equation 2.19.

The above equations are computed numerically using a piecewise parabolic method (PPM: Colella & Woodward 1984) hydrodynamic code called VH-1, originally developed at the University of Virginia (J. Blondin). The basic code was modified for the present study to include radiative driving terms, in order to solve the time-dependent equations for 2.5-dimensional cylindrical coordinates. In the 2.5-dimensional stimulation, the spatial mesh must be defined, and tests with different grid resolutions are needed to ensure similar results.

2.2.2 Boundary Conditions

The implementation of the boundary conditions in PPM must be specific to the values of the physical parameters at each grid point in the boundary of the spatial computational grid as well as the physical parameters at two grid points beyond each boundary grid point. The latter set of two spatial grid points are named "ghost zones" since they are points off the actual computational grid. Velocity and density in the ghost zones must be set in order to provide a reasonable condition for exiting wind solutions.

At the lower boundary, the velocity in the two radial zones below z_1 is set by constant-slope extrapolation, thus allowing the base velocity to adjust to whatever is appropriate for the overlying flow (Owocki et al. 1988). This usually corresponds to a subsonic wind outflow, although inflow at up to the sound speed is allowed. The base density in the ghost zones is set to satisfy the assumption of hydrostatic equilibrium of the disk, which yields a steady base outflow that is moderately subsonic.[1] In the disk atmosphere, the density profile of the accretion disk at radius r is a function of vertical height given by $\rho = \rho_o \exp(-z^2/H^2)$, where ρ_o is the density at the mid-plane of the accretion disk, $H = c_s(r^3/GM)^{1/2}$ is the scale height of the disk, and c_s is the sound speed. Each vertical size z_1 of the wind in the computational grid is adopted to start at $3H$, where the winds lift off from the subsonic regions of the disk. If a lower-boundary density is set to be much smaller than the base density at $3H$, a supersonic base outflow will be produced, and thus it is unable to adjust properly to the mass flux appropriate to the overlying line-driven wind. On the other hand, a much larger base density is set to make the lower boundary too "stiff", leading to persistent oscillations in the base velocity (Owocki et al. 1994).

At the outer boundary, the physical parameters at the ghost zones are set by simple flow extrapolation assuming constant gradients. For the boundaries of the radial ghost zones, zero gradients are implemented at the ghost zones for the physical parameters.

These time-dependent simulations also require setting an initial condition for the density and velocity over the entire spatial mesh at some starting time $t = 0$. For this we generally use a standard, finite-disk-corrected CAK wind, computed by relaxing a 1-dimensional sim-

[1] Computationally, we treat the steady base outflow as mildly subsonic with speeds of about 20% of the sound speed.

ulation to a steady state. Since the radial forces balance on the disk surface, the initial wind velocity must be normal to the surface of the disk, therefore the velocity along the r-direction is fixed at a value of $v_r = 0$. The velocity along the ϕ-direction is fixed at Keplerian speeds. From the assumed initial conditions, the models are advanced forward in time steps set to a fixed fraction 0.1 of the Courant time, which is the minimum computational time for the flow propagating along the zone with its sound speed.

2.2.3 Line Force Parameter

In the CAK formalism, the force multiplier is defined as the ratio of the radiation pressure force to that of electron scattering:

$$M = k \left[\frac{1}{\rho \sigma v_{th}} \left| \frac{dv}{dz} \right| \right]^{\alpha}. \tag{2.24}$$

The values k and α are the CAK parameters, dependent on temperature and the relative abundance of different elements in order to determine the strength of the line-driving force. The parameter k is proportional to the total number of lines, defined in terms of the electron scattering coefficient and a fiducial ion thermal speed (Abbott 1982); α is the ratio of optically thick lines to optically thin lines. For $\alpha = 1$ the line force considers only the thick lines, whereas for $\alpha = 0$ only thin lines are taken into account. Gayley (1995) pointed out that these parameters are correlated with each other in the study of OB stars, and the author also presented results on these parameters for the various stellar effective temperatures shown in Gayley's Table 1. For OB stars, the values are usually taken to be $k = 1/30$ and $\alpha = 0.7$ (Castor et al. 1975). In other models, Pereyra et al. (2000) used the values $k = 1/3$ and $\alpha = 0.7$. The combination of the velocity gradient and the density of the wind would determine the nature of the line force. If the velocity gradient increases to sufficiently high value, the contribution to the radiation pressure due to lines arrives at a maximum value. Abbott (1982) found the maximum value of the line radiation was obtained when $(1/\rho\sigma v_{th})dv/dz \leq 10^7$. In the Pereyra models, the authors assumed that the maximum possible value of the line force was obtained when $(1/\rho\sigma v_{th})dv/dz = 10^8$ (Pereyra et al. 2000). To be more realistic, local ionization equilibrium should be included into our model

self consistently and the line radiation force multiplier at each spatial grid point in the wind should be calculated in a manner equivalent to Abott's calculation for OB stars.

The ionization of the wind is crucial, for it determines the lines that can drive the flow, and hence the dynamics of the flow. If the wind is too ionized, no lines will be available to accelerate it. To avoid highly ionized gas, x-ray shielding is necessary. In our 2.5-dimensional model, we assume constant ion populations in the x-ray shielded region, and adopt the line force parameters used by MCG95 for their 1-dimensional models. In the x-ray non-shielded region we assume that line-force is negligible, which is an excellent approximation since the wind is completely ionized. As an improvement, it has been suggested that a photoionization code should be incorporated into ADW models (see Pereyra & Kallman 2003, for details).

2.2.4 Physical Parameters of the ADW Model

In the 2.5-dimensional hydrodynamic simulations, the mass of SMBH is used to set the initial parameters, for example, the rate of mass accreting into the SMBH and the inner radius of the accretion disk. We consider a non-rotating SMBH of $10^9 M_\odot$ as the test case. The inner radius of the accretion disk is $r_i = 3r_g \sim 4 \times 10^{15}$ cm. Together with the Eddington luminosity $L_{Edd} \sim 10^{47}\,\mathrm{ergs}^{-1}$, and Equations 2.7 and 2.9, we compute the mass accretion rate $\dot{M}_{acc} \sim 2 \times 10^{26}\,\mathrm{g\,s}^{-1}$, which can be used to determine the temperature structure of the accretion disk by Equation 2.5 for the given mass of the SMBH. To define the computational grids, the radial zones are set from the inner disk region $r_1 = 10r_i$ in terms of the inner radius of the disk to a maximum $r_n = 100r_1$, i.e., $r_1 \sim 10^{16}$ cm and $r_n \sim 10^{18}$ cm; the vertical zones are set from the subsonic height $z_1 = 3H$ in terms of the scale height of the disk to the supersonic height z_n defined as a larger distance beyond the maximum gravity of the SMBH. Note that the scale height is a function of the disk radius. At the lower-boundary of radial zones, the scale height is $H \sim 3 \times 10^{12}$ cm, thus defining the vertical zones to $z_1 \sim 10^{13}$ cm and $z_n \sim 10^{16}$ cm. The mass-loss rate of the wind $\dot{M}_w$ can be solved analytically from a standard, finite-disk-correction CAK wind solution as the input parameter for numerical models (see Pereyra et al. 2004, for details). In this case we calculate an approximate value $\dot{M}_w \sim 10^{26}\,\mathrm{g\,s}^{-1}$. For steady winds, mass conservation from Equation 2.17 yields the total

mass-loss rate $\dot{M}_w = \rho v A$, where ρ is the density of the wind, v is the velocity of the wind, and A is the area of the disk where winds launch. The location where winds start to lift off from subsonic regions inside the disk atmosphere defines the lower-boundary of vertical zones. The base density here is set to $\rho \sim 10^{-12}\,\mathrm{g\,cm^{-3}}$ by assuming the disk material propagates close to the sound speed, i.e, $v = c_s$. The sound speed is calculated using $c_s = \sqrt{k_B T(r)/\mu m_H}$, where k_B is the Boltzmann constant. Similar to the solar value, an atomic weight $\mu = 1.28$ is used, and m_H is the proton mass.

2.3 RESULT AND DISCUSSION

Following the work presented by Pereyra and collaborators (Pereyra et al. 2004, 2006), we have implemented their models with arbitrary gravitational fields, radiation flux distributions, and geometries into the VH-1 time-dependent hydrodynamic code based on the PPM numerical scheme, for 1-dimensional and 2.5-dimensional cases. Some of their models (i.e., the one they name as "FSH02") simplify to mimic the disk environment described by an analytic velocity law for a disk wind if a steady line-driven disk wind exits: that is, the accretion disk is steady and capable of supplying the corresponding mass flow of the wind. Other models are more realistic and mathematically more elaborate, and implement the exact line-driven radiation force from a standard accretion disk. For testing their models we calculated the line force through the CAK k–α parameterization (Castor et al. 1975). In our simulation, we have also explored a large parameter space, for example, the initial input (i.e., black hole mass), the boundary condition (i.e., base density), the computational grids (i.e., size), the computational time-step (i.e., Courant time) and the stimulation time. With the physical parameters of the ADW of the quasar described in Section 2.2.4, our numerical results show strong evidence for the non-existence of steady wind solutions for all of Pereyra models in both 1-dimensional and 2.5-dimensional cases. These results seem to be consistent with those obtained from Proga's time-dependent hydrodynamical models.

Our first attempt was to implement the 1-dimensional model of a solar-mass white dwarf accretion disk into the VH-1 code we modified. For the purpose of steady solution existence

analysis, we have reduced the 2.5-dimensional model to a series of the 1-dimensional models so that results could be tested for consistency through comparison with 1-dimensional analytic models which Pereyra developed. Based on the crude assumptions of disk-wind physical parameters, Pereyra and collaborators argued in favor of the existence of steady winds and derived an analytical expression for the velocity law of the winds. In the Pereyra simulation, they found that the initial wind conditions are not crucial for the existence of steady solutions, and they set the wind density at the base to a free boundary condition, which is determined by the simulation once a steady state is achieved. On the contrary, our simulation illustrates that the wind solutions are determinative to the implementation of the computational grids rather than the initial guess of wind conditions. We found that the computation grid which is best for zone spacing is in logarithmic scale increments, with the first zone defined at the sub-sonic region of the disk atmosphere. In contrast to different boundary conditions adopted by Pereyra, we set the base density to the inner boundary condition which is satisfied by the hydrostatic equilibrium assumption, such that the solution of the stimulated wind could be launched from the AD with a sub-sonic speed. In the simulation of a white dwarf accretion disk, we show that a steady wind can be achieved by fine-tuning the combination of grid size and boundary conditions. We also find the discontinuities in spatial derivatives of the velocity solution where the flow is highly supersonic, causing the occurrence of a kink in line-driven winds as shown in Figure 6. From there, we tried to extend the VH-1 code to the 1-dimensional ADW model for quasars with the black hole mass $\sim 10^9 M_\odot$. The accretion physics of quasars is similar to that of white dwarf but follows a mass scaling. We would expect similar numerical results for the cases of white dwarfs and quasars. However, by all means of numerical implementation, we are not able to achieve a steady disk-wind solution for quasars.

In conclusion, a steady disk-wind solution with a constant wind mass-loss rate is a consequence of balancing the gravitational forces and the radiation pressure forces. Our results demonstrate that a disk wind can be launched and developed by the local disk radiation. However, the existence or non-existence of steady wind solutions needs to be further explored. One of the issues is, of course, numerical instabilities in code implementation. Other possibilities could be that radiation driving is not enough to explain the observed steady

wind structure in AGN. This brings us to suggest that other mechanisms be considered, including magnetic driving, as Proga suggested (Proga 2000).

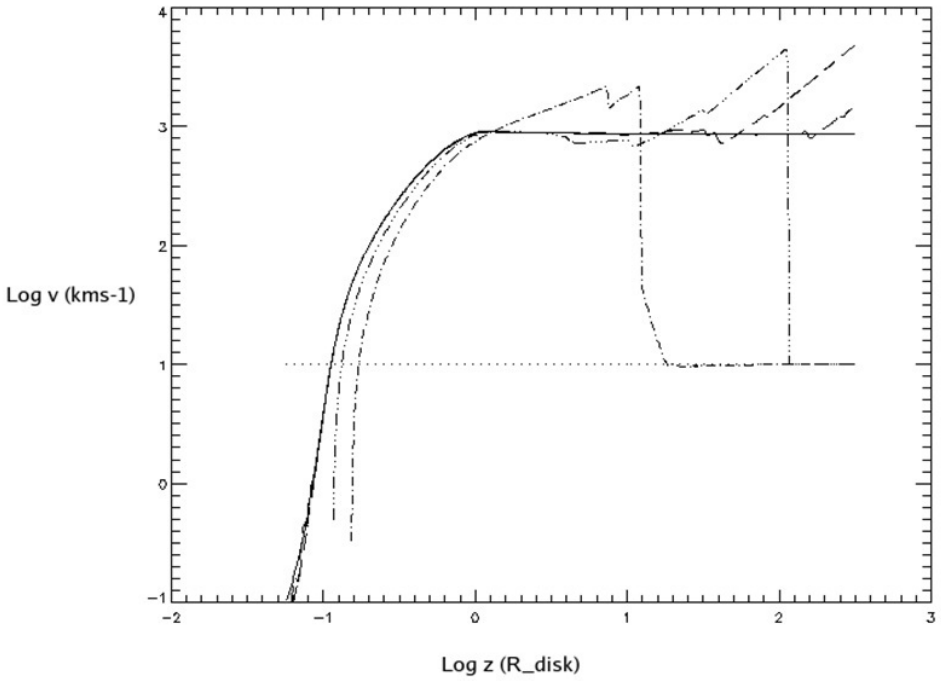

Figure 6 Time-dependent velocity distribution for a solar-mass white dwarf accretion disk scenario with a wind mass-loss rate of $2 \times 10^{-14} M_{\odot}\,\mathrm{yr}^{-1}$ and a solar radius for the accretion disk. The dotted line represents the initial velocity input. The solid line represents the final steady solution with a kink characteristic. The other lines represent the velocities at intermediate time steps.

3.0 REVERBERATION MAPPING TECHNIQUE

The time-delay between the broad emission line (BEL) variations and the ionizing source variations of a quasar or Type 1 Seyfert galaxy can be used to estimate the distance between the broad emission line regions (BELRs) and the central ionizing source. This technique is called reverberation mapping (RM). Based on measurements of emission-line time lags from RM observations, simple relationships between the sizes of the BELRs and the luminosities of sources can be established. By knowing this relation and making some assumptions, the mass of the central black hole (BH) can be estimated. Recent RM studies have been expanded from low-luminosity Seyfert galaxies to high-luminosity quasars. As such, a size-luminosity relation over 7 orders of magnitude in luminosity has been determined. Although the BELRs are much too small to be resolvable spatially, with an angular extent of only $\sim 10^{-5}$ arcsec even in nearby Seyfert galaxies at 50 Mpc, having scaling relation is important for placing constraints on the size scales of line-emitting regions in theoretical models. Our empirical model employs the most updated RM results of high-luminosity quasars to constrain the sizes of BELRs, particularly for the Lyα and CIV BELRs of a given BH mass.

3.1 PRINCIPLE OF REVERBERATION MAPPING

The term reverberation mapping applied to quasars and Seyfert galaxies first appeared in Blandford & McKee (1982) when emission-line variability became recognized as a real phenomenon. This RM method requires detailed comparison of continuum and BEL variations over time to determine the geometry as well as velocity field of the BELRs. In the standard model of AGN, the central source of x-ray and UV radiation is generated at the inner

part of the accretion disk, which has a spatial extent of a few tens of gravitational radii, $r_g \sim 1.5 \times 10^{13}(M/10^8 M_\odot)\,\mathrm{cm}$, from the central BH and heated to a very high temperature. The BELRs are at a distance ranging from a few hundreds to thousands of gravitational radii from the source, where emission line gas is orbiting around the BH. The observed emission lines are widely broadened due to the Doppler effect, as the gas and clouds in the emitting regions move supersonically at thousands of kilometers per second, which is believed to share the same Keplerian speed of the accretion disk around the central mass. The gas is photoionized by the central source of ionizing radiation, then the gas re-emits the radiation at discrete wavelengths, forming various collisionally excited and recombination lines in the AGN spectrum.

Continuum variability is a common characteristic of quasars and Seyfert galaxies. Because the emission of the BELRs is photoionized by the continuum radiation, it is naturally expected that variations in the continuum's strength will subsequently lead to corresponding variations in the strength or profile of the BELs. The fact is that any variation can only travel at the speed of light c, so there must be a time-delay between a variation in the continuum and a certain BEL. The first analysis of AGN emission-line time lags was carried out by Bahcall et al. (1972), who calculated the response of the total line intensity in a spherical distribution of gas due to a continuum variation. The authors demonstrated that an external observer will not see the entire emission line region respond instantaneously. Because of the finite speed of light, a cloud emitting at a distance r from the central ionizing source, and at angle θ to the observer's line of sight, will appear to respond after a time:

$$t = \frac{r}{c}(1 - \cos\theta). \tag{3.1}$$

Finally, the observer will see the entire line-emitting region responding on a time scale characteristic of the light-travel time across the region r/c. In the case of a thin spherical distribution of gas, when the ionizing flux is increased by a constant factor (a "boxcar") in a time interval $0 \leq t \leq \tau_{\mathrm{on}}$ and then resumes its original value (i.e., rectangular function), a distant observer will see that the line intensity rises linearly with time for $0 \leq t \leq \tau_{\mathrm{on}}$, is constant for $\tau_{\mathrm{on}} \leq t \leq 2r/c$, and then decays to its original value in a time τ_{on}, where $r \leq c\tau_{\mathrm{on}}/2$ is the radius of the shell.

The line-intensity response we observe is the integral of the responses of each line-emitting element to a short continuum change over time. For each BELR geometry and each change in continuum flux, there is a unique BEL response. Therefore, measuring the continuum and line light curves (i.e., light intensity as a function of time) can result in obtaining the geometry of the BELR. Blandford & McKee (1982) introduced the technique to solve the "transfer equation" which relates the two light curves through the "transfer function". Mathematically, it is represented as

$$L(t) = \int_{\infty}^{\infty} \Psi(\tau) C(t-\tau) \mathrm{d}\tau, \tag{3.2}$$

where $L(t)$ is the emission-line light curve, $C(t)$ is the continuum light-curve, and $\Psi(\tau)$ is the velocity-delay map (also called the "transfer function"), which contains the geometrical and physical information inherent to the reprocessing of energy that relates the two light curves. Given the observables $C(t)$ and $L(t)$ as a function of time, the transfer function can be solved, and thus used to infer the geometry and kinematics of the BELRs. From a practical standpoint, measuring the time shift τ between the continuum and the emission-line light curves can be used to derive the size of the BELR, R_{BELR}, simply by using $R_{\mathrm{BELR}} = c\tau$, where c is the light speed.

There are several fundamental assumptions that underlie the above RM principle, specifically:

1. The ionizing continuum originates in a single, central source extending to 10-100 gravitational radii. This size estimate is based on accretion disk models that are generally consistent with the observations.
2. The recombination time of photoionized BELR gas is much shorter than the light travel time across the BELR. This assumption is supported by a measured light-travel time of days to weeks, and the known recombination time for the BELR gas which is of order 1 hour.
3. The BELR structure and kinematics do not vary over the duration of the monitoring period. This places practical time limits on the duration of a single RM observing campaign.

4. The observed optical/UV continuum has a simple relation with the ionizing continuum that drives the line variations. Such a relation is not necessarily linear.
5. The continuum over a wide wavelength range is generally assumed to vary in phase with little or no time delay, though with smaller amplitude variations at longer wavelength. However, there are some exceptions (e.g., Peterson et al. 1998) and it is clear that a full understanding of the continuum emission processes is yet to be obtained. An extreme example is shown by Nandra et al. (1998), who found that the x-ray emission variations lag behind the UV by ~ 4 days.
6. The BELRs are under the influence of the gravitational potential of the central BH. This assumption has been discussed and justified by Peterson & Wandel (1999) and Wandel et al. (1999) for the Seyfert 1 galaxy NGC 5548.

3.2 BELR SIZE AND BH MASS ESTIMATE

RM measurements can be interpreted with confidence and the results lead to an estimate of black hole mass.

As the emission lines coming from the BELRs are widely broadened, the line-emitting gas is assumed to rotate at a Keplerian speed around the central BH. The rotational speed of the BELR gas, $v_{\rm BELR}$, can be estimated from the widths of the BEL profiles:

$$v_{\rm BELR} = f \times \Delta V. \tag{3.3}$$

The coefficient f, which relates the emission-line width ΔV to the intrinsic Keplerian velocity $v_{\rm BELR}$, is a geometric factor of order unity containing the information on the BELR's kinematics, geometry and inclination. The line width ΔV is commonly measured as the FWHM. Ideally, the width could be in the variable part of the BEL. For gas moving isotropically, $f \sim \sqrt{3}/2$ if a Gaussian line shape is observed. For gas purely in rotation along the accretion disk plane, the factor depends on the inclination disk-angle to the observer, i.e., $f \sim \sin i$ where i is the angle between the line of sight and the rotation axis (see Decarli et al. 2008 and references therein for the details).

Thus, knowing the distance to a BELR and the Keplerian velocity, along with the assumption that the motions in the BELR are dominated by the gravitational potential of the central BH, the BH mass can be calculated from the virial equation:

$$M_{\rm BH} = \frac{v^2_{\rm BELR} R_{\rm BELR}}{G} = \frac{f^2 {\rm FWHM}^2 R_{\rm BELR}}{G}. \tag{3.4}$$

Note that some RM observational results used FWHM for the measurement of the line width, and others argue that the line dispersion $\sigma_{\rm line}$ might be a better choice.[1] For example, Peterson et al. (2004) gets more self-consistent BH mass estimates by using $\sigma_{\rm line}$ instead of FWHM.

3.3 LIMITATIONS AND UNCERTAINTIES

Unfortunately, low S/N data can inhibit accurate line width measurements in a systematic manner (Denney et al. 2009). Since the mass scaling is in the second power of the measured line width, systematic differences or larger scatter in the measurements will propagate to significant differences in the mass values.

The mean time lag τ for a given BEL is measured from the centroid of the continuum and emission-line cross-correlation function. There should be no bias on the mean time lag as long as the BELR is axisymmetric and it emits isotropically. However, the assumption of isotropic emission in the BELRs will be relaxed in the later model.

The line widths are generally believed to represent a Keplerian velocity, however, the observed profiles are different from the ones expected from simple Keplerian orbits of arbitrary

[1] The first moment of the line profile is

$$\lambda_0 = \int \lambda P(\lambda) d\lambda / \int P(\lambda) d\lambda, \tag{3.5}$$

where $P(\lambda)$ is the line flux in a function of λ. The second moment of the profile is

$$\sigma^2_{\rm line}(\lambda) = < \lambda^2 > - \lambda_0^2 = \left[\int \lambda^2 P(\lambda) d\lambda / \int P(\lambda) d\lambda \right] - \lambda_0^2, \tag{3.6}$$

which is defined as the variance or mean square dispersion. The square root of this equation is the line dispersion $\sigma_{\rm line}$ or rms width of the line (Peterson et al. 2004).

inclinations. Thus, how to convert the observed BEL profile into a velocity measurement which can be used to calculate BH mass is not clear. The line-width determination is more challenging if the FWHM is affected by random noise, unremoved narrow-line components, or absorption due to intervening gas. For example, there have been a few RM monitoring campaigns on the MgII BEL, but the line is usually blended with FeII emission. Another problematic example is variable FeII emission lines near Hβ. Additionally, the line profiles and widths from the spectra obtained in RM studies may be variable (Kaspi et al. 2000). These variations in widths can be due to real changes in the BELR velocity field, or other observational effects, such as blending with weak lines.

The scaling factor f converts the virial product, based on the observables, to an actual mass. If the BELR is a flat Keplerian disk observed at inclination angle i, the scaling factor would include a $1/\sin^2 i$ term to account for the velocity projection. However, without additional information on the kinematics, geometry and inclination of the AGN from observations, we cannot determine f for a particular source.

3.4 PREVIOUS MAPPING RESULTS

3.4.1 Low-Luminosity Seyfert Galaxies

In the past two decades many monitoring campaigns were carried out and the sizes of BELRs for about three dozen AGN have been acquired. Most studies have concentrated on low-luminosity objects because their time lags are shorter and redshifts are low. In the following we summarize the conclusive results from these RM projects:

1. Different BELs respond to continuum variations on different time scales, therefore the size of a BELR depends on the emission line species observed. Previous RM studies show that higher ionization BELs (e.g., Lyα, NV, and CIV) have shorter time lags than lower ionization BELs (e.g., MgII, CIII], and Hβ), indicating that the high-ionization species tend to form closer to the central continuum source (Peterson 1993; Kollatschny 2003).
2. The typical line responses to continuum variations in low-luminosity AGN are of order

light-days to light-weeks, indicating that the BELR is smaller by an order of magnitude than was estimated from early 1980's photoionization models. This finding led to a revision of the old models to fit the new observational results (Peterson 1993).

3. In principle the BELR gas could be outflow, inflow, in Keplerian motion, in randomly-inclined orbits, or commonly mixed. There is, however, good evidence that the gravitational force of the central black hole dominates the motion of the BELR gas (e.g., Koratkar & Gaskell 1989, 1991; Crenshaw & Blackwell 1990; Peterson & Wandel 1999).

4. The size-luminosity relation in Seyfert 1s shows a large scatter. However, this relation is found to be consistent with a size scaling proportional to the square root of the luminosity expected from photoionization equilibrium, under the assumptions that the BELR gas is characterized by the same ionization parameter and density, and absorbs the same shape of ionizing continuum, independent of luminosity.

5. Different monitoring epochs have sometimes resulted in different time-lag results. For example, observations of NGC5548 indicated that the time lags from different observing seasons are correlated with the optical luminosity of the object (Peterson et al. 1999). This suggests a possible physical change in the BELR with time.

6. BELR gas is thought to be predominantly optically thick. However, in NGC5548, non-linearities in line responses to continuum variations are consistent with the idea of optically-thin regions in parts of the BELR (Shields et al. 1995).

7. Early campaigns have showed no detectable phase differences in variations between the UV and optical continua. However, more recent studies have found evidence for phase differences, suggesting a stratified continuum reprocessing region extending several light-days from the central source, possibly within the accretion disk (Collier et al. 1998; Peterson et al. 1998). Moreover, Nandra et al. (1998) found that the UV continuum variation in NGC 7469 leads the x-rays by ~ 4 days. This observation is unexpected and may require a significant change of view about x-ray production mechanism in AGN.

3.4.2 High-Luminosity Quasars

Many RM studies pertain to low-luminosity Seyfert 1 galaxies, and very little has been done on the luminous quasars. Observationally, they are fainter because of their large distances, making RM studies more difficult and demanding. Several attempts at such measurement have been made so far, but the results are controversial (Welsh & Robinson 2000; Trevese et al. 2006). Some potential problems, issues, and findings of RM studies in high-luminosity AGNs are as follows:

1. High-luminosity quasars are typically found at high redshifts $z \geq 1$. The required observing periods of such sources are significantly lengthened by the cosmological time dilation factor of $1 + z$. Furthermore, high-redshift sources are fainter and hence more difficult to observe.
2. Quasars with bolometric luminosity $\sim 10^{47} - 10^{48}\mathrm{ergss}^{-1}$ are expected to harbor some of the most massive BHs known, e.g., $10^9 M_\odot$. More massive BHs may have slower continuum flux variation with smaller amplitudes (Giveon et al. 1999; Vanden Berk et al. 2004). The smaller intrinsic variability amplitude of the continuum could result in smaller flux-variability amplitudes for the BELs, affecting the ability to detect the time delay in the BELR response.
3. The long-term continuum variability of quasars has been studied for many years (e.g., Usher 1978; Zamorani et al. 1984; Obrien et al. 1988; Hook et al. 1994; Netzer et al. 1996). Continuum flux has been shown to vary, and the amplitude of the variability is luminosity and wavelength dependent. For high-redshift quasars, the variability amplitudes in the rest-frame UV are higher than in the optical, leading to better characterized continuum light curves.
4. Assuming the size-luminosity relatiion behaves like a power-law, $R \propto L^\alpha$, Kaspi et al. (2005) used a sample with a range of luminosities, $10^{43} - 10^{46}\,\mathrm{erg\,s^{-1}}$, and found that the mean Balmer-line BELR size scales differently with optical, UV, and x-ray luminosities. These results disagree with the theoretical expected slope of 0.5, indicating that the simple assumption that all AGN have on average the same ionization parameter, BELR density, column density, and ionizing spectral energy distribution is not valid, and there

is likely some evolution in a few of these characteristics along the luminosity scale.

3.5 SCALING RELATIONS FOR CIV AND LYα FROM REVERBERATION MAPPING

Most of the RM studies mentioned above were based on Balmer BELs, generally Hβ, and optical luminosity variations. For objects at redshifts $z \geq 2.5$, studies have been expanded to UV luminosities and UV BELs such as CIV (e.g., McLure & Jarvis 2002; Vestergaard & Peterson 2006). In low-luminosity AGN, the size relation for high-ionization to low-ionization BELRs has been well established (Peterson 1993), while for high luminosity AGN this is still demanding. The first attempt to do this was based on the RM results for low-luminosity AGN. Using Hβ results Warner et al. (2003) inferred the distance of the CIV BELR from a low-luminosity sample and obtained

$$R_{\rm BELR}({\rm CIV}) = 9.7 \left[\frac{\lambda L_\lambda(1450\mathring{A})}{10^{44}\,{\rm erg\,s^{-1}}}\right]^{0.7} {\rm lt\text{-}days}, \tag{3.7}$$

where $\lambda L_\lambda(1450\mathring{A})$ is the continuum luminosity at 1450 Å. Then Kaspi et al. (2007) directly used the RM technique on the CIV BEL from eight luminous and distant quasars, and obtained

$$R_{\rm BELR}({\rm CIV}) = 1.7 \left[\frac{\lambda L_\lambda(1350\mathring{A})}{10^{43}\,{\rm erg\,s^{-1}}}\right]^{0.52} {\rm lt\text{-}days}. \tag{3.8}$$

This is the first available RM result for the CIV BEL using luminous quasars. When more data become available, the slope and offset of the relation will likely be modified. Applying the current result to objects with similar luminosity, the distance estimate in Equation 3.7 is roughly two times larger than the distance estimate from Equation 3.8. In spite of the discrepancy, it is promising that there is some indication that low-luminosity results might be scaled and applied to high-luminosity objects. For now, constraining the size scale of the CIV BELR in theoretical models by adopting either size-luminosity scaling is reasonable.

In the virial theorem, given the velocity v of a particle orbiting at a certain radius R around the central source, the central mass is simply $M = Rv^2/G$. Likewise, in RM studies, if the radius of the emitting region is known, then the mass of the central black hole can be

estimated. Therefore, given the motion of BELR, $v_{\rm BELR}$, which is concealed in the FWHM of a line profile with the geometric factor in Equation 3.3, Kaspi et al. (2000) has presented relations for black hole masses as follow:

$$M_{\rm BH} = 1.5 \times 10^5 \left(\frac{R_{\rm BLR}}{\text{lt-days}}\right) \left(\frac{v_{\rm FWHM}}{10^3 \text{kms}^{-1}}\right)^2 M_\odot. \tag{3.9}$$

Combining Equation 3.7 and Equation 3.9, it yields

$$M_{\rm BH} = 1.4 \times 10^6 \left(\frac{\text{FWHM(CIV)}}{10^3 \text{km s}^{-1}}\right)^2 \left(\frac{\lambda L_\lambda(1450\mathring{A})}{10^{44}\,\text{erg s}^{-1}}\right)^{0.7} M_\odot. \tag{3.10}$$

Similarly, combining Equation 3.8 and Equation 3.9, it yields

$$M_{\rm BH} = 2.5 \times 10^5 \left(\frac{\text{FWHM(CIV)}}{10^3 \text{km s}^{-1}}\right)^2 \left(\frac{\lambda L_\lambda(1350\mathring{A})}{10^{43}\,\text{erg s}^{-1}}\right)^{0.52} M_\odot. \tag{3.11}$$

These inferred black hole masses are purely inferred from the widths of BELs and continuum luminosities. Such results provide important constraints on the structure of quasars. Thus, thanks to the RM technique, size scales of BELRs and central black hole masses can be constrained in theoretical models. However, it is worth noting that accurately measuring high-redshift BELs remains challenging due to the complexity in some of quasar spectra.

As noted earlier, high-luminosity, high-redshift AGN (e.g., quasars) have rarely been studied due to observational difficulties. In particular, RM distance estimates using high-ionization lines like the Lyα BEL have not been available for luminous objects, while there have been numerous RM studies of low-luminosity AGN using the Lyα and CIV BELs. At low luminosity it has been confirmed that both lines have similar size scales. However, Kaspi et al. (2007) reported no significant (i.e., $> 5\%$) Lyα BEL variability in luminous quasars. In contrast, however, they did report variations in the CIV BEL in response to continuum variations, and they established a size-luminosity relation for the CIV BEL. Therefore, to explore the feasibility of expanding RM samples to high-redshift, high luminosity quasars, and to check the results of Kaspi et al. (2007), I carried out further work to verify the variability of CIV and Lyα BELs. I used a sample of quasars which were observed twice in the Sloan Digital Sky Survey (SDSS). I found variability in both BELs, which was clearly contradictory to the Lyα BEL results of Kaspi et al. (2007). Combining our findings with the existing relation between distance and line-luminosity of CIV, I was able to constrain the location of Lyα BELR. The work is discussed in next chapter.

4.0 VARIABILITY OF BROAD EMISSION LINES IN HIGH-LUMINOSITY, HIGH-REDSHIFT QUASARS

We examine the variability of the high-ionization Lyα λ1216 broad emission line (BEL) in a sample of 63 high-luminosity, high-redshift quasars observed at two epochs by the Sloan Digital Sky Survey (SDSS). These bright objects lie in the redshift interval $z = [2.5, 4.3]$ and have luminosities greater than $\lambda L_\lambda \sim 2.7 \times 10^{45}$ erg s^{-1} at 1300 Å. Utilizing improved spectrophotometric flux calibrations relative to nearby compact stars observed simultaneously, we are able to measure the flux changes in Lyα and the nearby continuum at two epochs. We find 21 objects that exhibit Lyα BEL flux variability at a significance level greater than 5σ on time scales ranging from days to years in the quasar rest frame. The results show that, despite some early work in which no significant Lyα BEL flux changes were detected, variability is present and readily observable. We also consider the CIV λ1549 BEL. The lack of a strong correlation between Lyα BEL variability and nearby continuum variability is consistent with the presence of a time lag between the variations, whereas the presence of a stronger correlation between Lyα BEL variability and CIV BEL variability suggests that these BEL regions (BELRs) are at similar distances from the central ionizing source. Some interesting examples are high-lighted in the analysis, including a case where the flux of a Lyα BEL increased by $\sim 26\%$ in 14 days in the quasar rest frame, suggesting that the BELR has the shape of a disk, which is being observed face-on. This work demonstrates that future campaigns of spectrophotometric monitoring can improve our understanding of the structure of the BELRs of high-luminosity, high-redshift quasars.[1]

[1] Chapter 4 is a paper submitted to MNRAS by Sui Chi Woo, David A. Turnshek, Carles Badenes, and Steve Bickerton.

4.1 INTRODUCTION

Broad emission lines (BELs), such as Lyα, Nv and Civ, are prominent signatures seen in the optical/UV spectra of quasars. These lines arise in gas photoionized by the x-ray and UV continuum emission from the inner region of an accretion disk surrounding a supermassive black hole (SMBH) (Peterson 2011, 2006; Elvis 2010; Davis et al. 2007). Consequently, when continuum fluxes vary with time, BEL fluxes should respond to these variations but with time lags. Reverberation mapping studies of individual quasars and active galactic nuclei (AGN) can use results on time lags to determine the distances between central continuum sources and BEL regions (BELRs). Furthermore, these size estimates for BELRs can be used with BEL velocity widths to infer the masses of SMBHs, under the assumption that the line-emitting regions are gravitationally bound to the SMBHs (Grier et al. 2012; Denney et al. 2010; Vestergaard & Peterson 2006; Kaspi et al. 2005). Deducing BELR size scales and SMBH masses are fundamental to understanding the physics of quasars.

There have been numerous reverberation mapping studies of lower luminosity, low-redshift AGN such as Seyfert galaxies. See, for example, Peterson (1993) and Peterson et al. (2004) for early reviews. Observationally such objects are brighter because they are nearby, and therefore variations are easier to detect. Also, their BELs tend to vary on shorter time-scales, of order light-days to light-weeks, and this permits more convenient temporal sampling to study the variability. Studies of lower luminosity AGN show that higher ionization BELs (e.g., Lyα and Civ) respond more rapidly to continuum variations than lower ionization BELs (e.g., Hβ, Ciii], and Mgii), indicating that lower ionization BELRs are farther out from the central source. In particular, the eight-month UV monitoring program of NGC 5548 ($\lambda L_\lambda \sim 4.2 \times 10^{43}$ erg s^{-1} at 1300 Å) found time lags of ~ 10 days for both Lyα and Civ, suggesting that these BELRs have similar size scales (Clavel et al. 1991).

To date, limited reverberation mapping work has been attempted on the more luminous quasars. Although quasars are known to be more energetic than AGN, they are usually significantly fainter than well-studied AGN due to their higher redshifts. Moreover, under the assumption that the photoionized BELRs of quasars and AGN have similar physical conditions, quasar BELR distances from the central source (and hence time lags) are expected

to be larger by a factor of $\sim (L_{quasar}/L_{AGN})^{0.5}$, where L is luminosity. This is exacerbated by the fact that time lags in observed frames should be a factor of $1+z$ larger than in quasar/AGN rest frames due to cosmological considerations (i.e., at high redshifts we observe variations in "slow motion"). All of these effects make reverberation mapping studies of high-luminosity, high-redshift quasars more difficult and challenging.

While numerous studies have demonstrated that quasars have variable continua, few studies of their BEL variability have been made. O'Brien & Harries (1991) found a time lag of $\sim$ 74 days between the UV continuum and the Lyα BEL in the luminous quasar 3C273. However, Ulrich et al. (1993) argued that the BEL variations were only marginally significant. A number of years ago Kaspi et al. (2007) reported no significant (i.e., $> 5\%$) Lyα BEL variability in a luminous sample of high-redshift quasars. However, they did report significant variations in the CIV BEL in response to continuum variations, leading to a time lag estimate of $\sim$ 188 days in the quasar rest frame. Given these ambiguous results, it is not clear whether the Lyα BEL shows the same variability results as the CIV BEL, and whether reverberation mapping results from low-luminosity, low-redshift AGN can be scaled and applied to high-luminosity, high-redshift quasars.

Therefore, the goal of this chapter is to investigate the variability of BELs in high-luminosity, high-redshift quasars. This would help clarify the feasibility of reverberation mapping studies for such a sample. To accomplish this we selected a sample from the Sloan Digital Sky Survey (SDSS) which had multiple spectral observations and we applied the spectrophotometric calibrations of Yip et al. (2009) to improve the spectrophotometry. In Section 4.2 we present the quasar sample, and we discuss the additional calibrations which can improve the relative spectrophotometric accuracy of the data. In Section 4.3 we outline how we measure flux changes in BELs and continua, and we present the results. Among other findings, our analyses show that $\sim$33% of our sample exhibits significant ($> 5\sigma$) Lyα BEL flux variations. These variations are not strongly correlated with nearby continuum variations, which is consistent with the presence of a time lag. However, a stronger statistical correlation between Lyα BEL flux variations and CIV BEL flux variations is seen, which suggests that these BELRs have similar size scales. In Section 4.4 we summarize the results and briefly discuss future prospects.

4.2 QUASAR DATA SET

4.2.1 Sample Definition

For this study we used the SDSS data release (DR8, Aihara et al. (2011)) to select an appropriate sample of quasars. In the observed frame SDSS spectra cover the optical to near-infrared ($3800-9200$ Å) with resolution $\lambda/\Delta\lambda \sim 2000$ at 5000 Å (Stoughton et al. 2002). To define our quasar sample and ensure that Lyα λ1216 BELs are included in the spectra, we selected objects which are spectroscopically classified as QSOs, have redshifts in the interval $z = [2.5 - 5.0]$, and have multiple spectroscopic observations. The spectral classifications given in DR8 are highly reliable, with 98% accuracy in two independent reduction pipelines (spectro1d and idlspec2d). We excluded quasars observed using different plates on different dates to avoid possible calibration problems. Reasons for repeat spectroscopic observations in the SDSS are described in Wilhite et al. (2005). The repeat observations span time intervals ranging from days to years in the observed frame, leading to interesting durations for probing spectral variability in the quasar rest frames. In addition to the wide range of time intervals, the large sample size and homogeneity of SDSS spectroscopic data provide a unique advantage.

We found 407 quasars meeting the above criteria in DR8. Since variability in the observed frame at these higher redshifts is generally expected to increase with time interval, we have used only the first and last observations in order to maximize the time interval when more than two observations at different dates with the same plate exist.

4.2.2 Refinement of the Spectrophotometric Calibration

The work of Vanden Berk et al. (2004) and Wilhite et al. (2005) demonstrate that some additional spectrophotometric calibrations of SDSS spectra can be applied to increase the accuracy of spectral variability studies. Wilhite et al. (2005) used the stars to derive calibration differences between same-plate pairs, under the assumption that the majority of stars are non-variable. Later Yip et al. (2009) adopted a slightly different methodology, using galaxies instead of stars, since galaxies should be non-variable. Yip et al. (2009) estimated

that their method improves the relative flux calibration between plate pairs by about a factor of two. The two-step calibration methods we used in this study are summarized below. See Yip et al. (2009) for a complete discussion.

First, to achieve an improved relative flux calibration for objects on a pair of plates taken at different MJDs (modified Julian dates), a wavelength-dependent flux ratio correction calibration is derived and applied. This is step one. This is done by employing corrections made available by Yip et al. (2009). Their final corrections were derived from fifth-order polynomial least-squares fits, which provide low-order spectral corrections and eliminate higher-order spurious spectral features. These corrections were available for plate pairs in our sample up to DR6. Therefore, this further limited our sample size, since only 181 of the 407 plate pairs in our DR8 sample had an available wavelength-dependent calibration correction. This correction was applied to all 181 objects to search for variability.

Second, for significantly variable quasars, which are identified after step one and which require closer examination, we can derive and apply a wavelength-independent (i.e., gray) flux normalization correction using measurements of nearby non-variable compact objects surrounding a quasar.[2] This improves the relative spectrophotometric calibration between plates. We call this correction C_{band}, where "band" refers to the rest wavelength intervals specified below. Instead of choosing a narrow wavelength band at 6450 Å $\pm$ 520 km s^{-1} as suggested in Yip et al. (2009), we use the entire region from just longward of Lyα to longward of CIV, but exclude the locations of prominent emission lines. The rest frame wavelength bands which we use to derive C_{band} are $1260-1286$ Å, $1318-1380$ Å, $1430-1525$ Å, and $1580-1620$ Å.[3] Table 1 gives examples of the additional improvements that can be achieved by presenting before and after C_{band} corrections for four selected quasars and nearby non-variable compact objects. These four example quasars are further discussed in Section 4.3.4. After C_{band} corrections are applied, compact objects should show no significant variability, and this turns out to be the case.

[2]A better approach might involve using galaxies to further improve the flux calibration, since they are clearly non-variable. However, because galaxies are extended and quasars are compact, possible variations in seeing between plate epochs make this approach problematic.

[3]The derived C_{band} results for each compact object change less than a few percent when the wavelength intervals are reduced by a factor of two to 1260-1273 Å, 1318-1349 Å, 1430-1478 Å, and 1580-1600 Å. Thus, derived C_{band} corrections are robust and reasonably optimized.

In summary, as outlined above, we implemented the first step to improve the wavelength-dependent spectrophotometric calibration and then the second step to improve the wavelength-independent relative spectrophotometric calibration, before we performed the variability analysis in Section 4.3.

4.2.3 Elimination of Problematic Objects

4.2.3.1 Poor Sky Subtraction Sky subtraction of SDSS spectra is done in an automated data reduction pipeline. Wild & Hewett (2010) have pointed out that significant systematic residuals can remain in SDSS sky-subtracted spectra due to sub-optimal subtraction of the strong OH sky emission lines longward of 6700 Å. In addition, we have found that some lower signal-to-noise ratio (S/N) spectra (e.g., spectra of fainter high-redshift quasars initially selected for this study) can suffer from poor sky subtraction, leading to false-positive results on spectral variability. For the two observation epochs of our sample of 181 quasars, we plot in Figure 7 the average synthetic r-band magnitude derived from the SDSS spectra versus the average spectral S/N. As expected, S/N is seen to decrease with increasing magnitude. However, for average $r > 19.7$ or average $S/N < 10$ we have identified cases of false-positive results when performing our variability analysis. A clear indication of potential problems can be seen by examining data for the faint quasar SDSS J101840.46+285000.7, which has average $r \approx 22.3$ and average spectral $S/N \approx 0.9$. In our initial analysis of this object we detected significant flux variations over the entire range of observed wavelengths in just ~ 2.5 days in the quasar rest frame. However, examination of the sub-exposures (Bickerton et al. 2012), which were used to form the SDSS spectra at the two epochs, showed that poor sky subtraction was responsible for the apparent flux variations. The initial epoch spectrum was formed from nine sub-exposures and the final epoch spectrum was formed from three sub-exposures. Figure 8 illustrates the correlations between fluctuating sky spectra and Lyα + N V BEL fluxes and nearby continuum fluxes (see Section 4.3.1 for how these were measured), respectively, over 12 sub-exposures.[4] Following the initial analysis of our sample we have concluded that a reliable search for spectral

[4] For the analysis presented in Figure 8, we measured the Lyα + N V BELs, but for the subsequent analyses we measured the Lyα BEL.

variability requires the exclusion of objects with average $r-$band magnitudes fainter than ~ 19.7 and average spectral $S/N < 10$. This reduces our sample to 66 quasars.

4.2.3.2 Discrepant Redshifts When considering quasar redshift information for our sample we had to exclude three objects because the SDSS pipeline redshifts were discrepant: SDSS J101449.56+032600.8, SDSS J105905.06+272755.4, and SDSS J115852.86−004301.9.[5] This reduces the size of our final sample to 63 quasars with luminosities $\lambda L_\lambda > 2.7 \times 10^{45}$ erg s^{-1} at 1300 Å and redshifts $z = [2.5, 4.3]$.

4.3 VARIABILITY ANALYSIS

Due to S/N differences and velocity offsets among different measured BELs, the SDSS pipeline usually calculates slightly different emission redshifts for the pair of spectra being analyzed. Also, Wild & Hewett (2010) have shown that SDSS quasar redshifts possess systematic biases of ~ 600 km s^{-1}. For consistency, and because of the effects mentioned above, we take two precautions when performing our analysis. First, we calculate a single redshift by averaging the pair of redshifts available for the two spectra. We then shift each spectrum into the rest frame of the quasar for subsequent analysis. The rest-frame wavelength region of interest was chosen to be $1100 - 1700$ Å so that the regions containing Lyα λ1216 BELs and CIV λ1549 BELs are included. Second, as discussed below, when measuring BEL fluxes, we use a velocity window which is large enough to ensure that typical velocity offsets will not significantly affect the results.

As discussed in the next two sections, we use two methods to make two different kinds of comparison to assess variability. Both methods rely on determining and subtracting the continua underneath the BELs in each spectrum. In the first method flux differences of BELs and continua between the two spectra are considered. In the second method flux ratios of BELs and continua between the two spectra are considered.

[5] For SDSS J101449.56+032600.8 and SDSS J105905.06+272755.4, the BELs are incorrectly identified so the redshifts are incorrect. For SDSS J115852.86−004301.9, the classification of QSO is incorrect.

4.3.1 Continuum and BEL Flux Changes

4.3.1.1 Continuum Changes For each two-epoch pair of spectra we start by determining the mean continuum flux of each spectrum in the line-free regions near the Lyα BEL, defined as $1276 - 1286$ Å and $1318 - 1334$ Å, which ensures that the region in the vicinity of any OI λ1302 BEL is excluded. Also, if necessary, any bad spectral regions within these wavelength intervals are identified by visual inspection and excluded. The spectrum with higher S/N in the observed r-band in the two-epoch pair is labeled HSN, whereas LSN refers to the one with lower S/N. The continuum flux difference at ~ 1300 Å is determined by subtracting the LSN-epoch mean flux from the HSN-epoch mean flux: $\Delta F_{c1300} = F_{c1300,HSN} - F_{c1300,LSN}$. The normalized flux change in the continuum is then defined to be $\Delta F_{c1300}/F_{c1300,HSN}$. Since the change in continuum level near ~ 1300 Å is as near as we can get to the ionizing continuum, we use this wavelength to measure the continuum change throughout this study. Standard deviations are determined by propagating the SDSS pipeline flux errors. Twenty-nine objects exhibit continuum flux changes at levels of significance $> 5\sigma$.

4.3.1.2 Lyα BEL Flux Changes To study flux variations in the Lyα BEL we chose $1204 - 1229$ Å as the region of interest (i.e., a region encompassing ≈ 6170 km s^{-1} around the BEL). This generally covers most of the flux in a Lyα BEL and is selected to mostly avoid inclusion of the nearby NV λ1240 BEL. Thus, the chosen interval is a practical fixed choice not intended to match the observed width of the Lyα BEL, but it is suitable for the purpose of this study. The measured change in BEL flux can weakly depend on the chosen wavelength interval.[6] To determine the continuum level to subtract underneath a Lyα BEL we use the mean continuum flux in the nearby continuum (Section 4.3.1.1). This works as well as an extrapolated straight-line fit. An extrapolated higher-order polynomial fit would be inappropriate. Unfortunately, the region shortward of the Lyα BEL is generally depressed by the Lyα forest in the moderate resolution SDSS spectra, so this region could not be used

[6] Also, a flux change might vary across the BEL profile. For example, one or both of the BEL wings could show changes that are different than changes in the BEL core. We searched for clear indications of such behavior by considering the central half of the original velocity interval (i.e., $1210 - 1223$ Å), but found no clear examples of this. However, see Section 4.3.4.3.

to help determine the continuum level underneath the Lyα BEL. The absolute Lyα BEL fluxes in the HSN and LSN pair of spectra are then $F_{\mathrm{Ly}\alpha,HSN}$ and $F_{\mathrm{Ly}\alpha,LSN}$, respectively. Consistent with our previous definitions for a change in the continuum, the Lyα BEL flux difference is $\Delta F_{\mathrm{Ly}\alpha} = F_{\mathrm{Ly}\alpha,HSN} - F_{\mathrm{Ly}\alpha,LSN}$ and the normalized Lyα BEL flux difference is $\Delta F_{\mathrm{Ly}\alpha}/F_{\mathrm{Ly}\alpha,HSN}$.

Figure 9 shows the distribution of normalized Lyα BEL flux changes versus normalized continuum flux changes for the 63 sample quasars. Again, the standard deviations shown for the plotted points are determined by propagating the SDSS pipeline flux errors. Twenty-one quasars (shown in red) show Lyα BEL flux variations at a significance level $> 5\sigma$. Among these 21 quasars we have selected four to discuss in Section 4.3.4.

As an illustration of what the results shown in Figure 9 might mean we have parameterized how flux changes in a hypothetical, but typical, Lyα BEL profile and the associated nearby continuum would appear in this plot. To do this we parameterize a continuum-normalized HSN spectrum as

$$f_{HSN}(\lambda) = 1 + Ae^{-(\frac{\lambda - 1216\text{Å}}{\delta\lambda})^2}, \tag{4.1}$$

where A is the amplitude of the Lyα BEL peak at 1216 Å relative to the normalized continuum and $\delta\lambda$ sets the line width. For this illustration we put $A = 5.5$ and $\delta\lambda = 12$ Å (~ 3000 km s^{-1}), which are typical. The hypothetical LSN spectrum is then paramerterized as

$$f_{LSN}(\lambda) = a_1 + a_2 Ae^{-(\frac{\lambda - 1216\text{Å}}{\delta\lambda})^2}, \tag{4.2}$$

where a_1 and a_2 dictate how the flux in the continuum and Lyα BEL change, respectively. A grid of a_1 (on the dashed horizontal axis) and a_2 (on the dotted vertical axis) parameters are overplotted on Figure 9 to give an indication of the nature of the observed flux changes in our sample.

4.3.1.3 CIV BEL Flux Changes Following the procedure we used to measure Lyα BELs in Section 4.3.1.2, we have also measured CIV BELs. However, the continuum levels we subtract from CIV BELs are measured at $1470-1488$ Å and $1600-1616$ Å in the quasar rest-frames. We then measure the CIV BEL over the rest-frame interval $1534-1566$ Å, which corresponds to a velocity interval that is similar to the one used for the Lyα BEL. Eight objects exhibit CIV BEL flux changes at levels of significance $> 5\sigma$. In the bottom panel of Figure 9 we show $\Delta F_{CIV}/F_{CIV,HSN}$ versus $\Delta F_{c1300}/F_{c1300,HSN}$. On this bottom panel we also show the same grid of a_1 and a_2 values shown in the top panel of Figure 9 for the Lyα BELs. This permits a comparison between changes in the Lyα and CIV BELs.

4.3.1.4 Correlations between Flux Changes in the Continuum, Lyα BEL, and CIV BEL Past monitoring campaigns of low-luminosity Seyfert 1s conducted with the *International Ultraviolet Explorer* (*IUE*) have revealed similar time lags for Lyα and CIV BELs (Korista et al. 1995). To check if this holds in our quasar sample, in Figure 10 we plot the normalized Lyα BEL flux changes versus the normalized CIV BEL flux changes. Analysis of the results shown in Figures 9 and 10 reveal correlations between the flux change results. After taking into account the variances of the data points, the correlation coefficients are: 0.43 for Lyα BEL flux changes versus continuum changes (Figure 9, top panel), 0.51 for CIV BEL flux changes versus continuum changes (Figure 9, bottom panel), and 0.74 for Lyα BEL flux changes versus CIV BEL flux changes (Figure 10). Thus, there is a significantly stronger correlation between observed changes in the two BELs, in comparison to correlations between changes in either BEL and the continuum.

4.3.2 Flux Ratios between the HSN and LSN Epochs

The second method we use to evaluate variability involves examining the ratio of spectral components at the two different epochs. This is useful because it provides a different way to assess our results. To evaluate this we consider $R_{\rm Ly\alpha} = F_{\rm Ly\alpha,HSN}/F_{\rm Ly\alpha,LSN}$ versus $R_{c1300} = F_{c1300,HSN}/F_{c1300,LSN}$ and $R_{CIV} = F_{CIV,HSN}/F_{CIV,LSN}$ versus R_{c1300} in Figure 11 (top panel and middle panel, respectively). We also plot $R_{\rm Ly\alpha}$ versus R_{CIV} in Figure 11

(bottom panel). The data shown in red in these figures are the same data originally plotted in red in Figures 9 and 10, i.e., objects showing absolute flux variations in the Lyα BEL at a level of significance $> 5\sigma$. Of course, when R values are unity it represents no flux change and when, for example, $R_{\rm Ly\alpha} = R_{c1300}$ it indicates that the Lyα BEL and the nearby continuum experienced the same fractional increase or decrease in flux (i.e., gray scaling). The results generally confirm the findings of Section 4.3.1.4. After taking into account the variances of the flux ratios, the correlation coefficients are: 0.54 for $R_{\rm Ly\alpha}$ versus R_{c1300} (Figure 11, top panel), 0.69 for R_{CIV} versus R_{c1300} (Figure 11, middle panel), and 0.76 for $R_{\rm Ly\alpha}$ versus R_{CIV} (Figure 11, bottom panel).

4.3.3 Time Variations

For our sample of 63 high-luminosity, high-redshift quasars, the top, middle and bottom panels of Figure 12 show results on the fractional changes in Lyα BEL flux, CIV BEL flux and continuum flux, respectively, as a function of time between observation epochs in the quasar rest frame, $\Delta\tau$.

4.3.4 Examples of Detected Variations

From the 21 quasars with $> 5\sigma$ Lyα BEL variations shown in Figure 9 (red points), we select four representative cases to illustrate. Table 2 summarizes the two-epoch flux measurements of the BELs and continua for these four quasars, along with their associated emission redshifts, rest-frame time intervals $\Delta\tau$ between the two observationi epochs, r-band magnitudes, and luminosities.

The spectral changes in the four quasars are shown in Figures 13−16. The red and blue curves in the figures represent the spectra at HSN-epochs and LSN-epochs, respectively. The overplotted black solid lines are the spline fits to the continua and BELs. The dark red curve in the top panel of the figures is the flux difference between the two epochs, whereas the dark red curve in the bottom panel is the flux ratio between the two epochs. A brief discussion of the four examples follows.

4.3.4.1 SDSS J004240.65+141529.6 The spectra of SDSS J004240.65+141529.6 ($z \approx 3.70$) are shown in Figure 13, $\sim$ 14 days apart in the quasar rest frame. The redshift of the Lyα BEL is somewhat larger than indicated by the SDSS pipeline redshift, but the redshift of the CIV BEL is a close match. The measured Lyα BEL flux seen in the second LSN-epoch spectrum is $\sim$ 26% fainter than in the first HSN-epoch spectrum, whereas the nearby continuum flux decreases only $\sim$ 6%. The relatively fast change in Lyα BEL flux in this quasar might be considered surprising given its high luminosity. For example, if the luminosity of this quasar is compared to the luminosity of AGN NGC 5548, we find: $(L_{quasar}/L_{AGN})^{0.5} \sim 13.6$. Of course, time lags can not be derived from two-epoch data. However, if BELRs are larger in luminous quasars, one might naively expect fractional Lyα BEL flux variations to be slower in high-luminosity objects. Yet the fractional variations seen in this quasar are comparable to the ones seen in NGC 5548 (Peterson 1994). The observed fast change suggests that a significant fraction of the Lyα BELR has a correspondingly small size scale along our sightline. For example, this would occur if the Lyα BELR were confined to a disk-like region, and we were viewing the disk close to face-on. In such a geometry the light travel time across the BELR along our sightline would be $\sim sin(i) D_{\mathrm{Ly}\alpha\ BELR}$, where i is the inclination angle relative to the disk's polar axis and $D_{\mathrm{Ly}\alpha\ BELR}$ is the diameter of the Lyα BELR disk. Thus, this observation would support the idea that the Lyα BELR is due to disk emission. Alternatively, these short time-scale variations might indicate anisotropic emission from the BELR, as has been discussed by Perez et al. (1989).

4.3.4.2 SDSS J132750.44+001156.8 SDSS J132750.44+001156.8 (Figure 14, $z = 2.53$) shows increases in the Lyα BEL flux and nearby continuum flux of $\sim$ 34% and $\sim$ 12% during a period of $\sim$84 days in the quasar rest frame. The BELs are very broad, such that the wings of the Lyα and CIV BELs are not included in the $\sim$ 6200 km s^{-1} interval that we measure. Relative to the SDSS pipeline redshift, the redshift of the peak of the Lyα BEL appears higher and the redshift of the peak of the CIV BEL appears lower. A significant flux change in the CIV BEL is not observed. The continuum spectral slope at the brighter HSN-epoch is bluer than observed at the LSN-epoch.

4.3.4.3 SDSS J095106.32+541149.8

The spectra of SDSS J095106.32+541149.8 (Figure 15, $z = 2.69$) were taken ~ 610 days apart in the quasar rest frame. Significant flux changes in both the Lyα and CIV BELs are present, whereas no significant change in the nearby continuum flux is observed. Relative to the initial LSN-spectrum the Lyα BEL flux increased $\sim 25\%$, the nearby continuum flux increased $\sim 1\%$, and the CIV BEL flux increased $\sim 20\%$. The redshift of the Lyα BEL is consistent with the SDSS redshift, but the redshift of the CIV BEL is somewhat lower. The Lyα BEL may show a larger flux change in the line core than in the wing.

4.3.4.4 SDSS J120802.64+630328.9

The spectra of SDSS J120802.64+630328.9 (Figure 16, $z = 2.57$) were taken ~ 613 days apart in the quasar rest frame. No significant flux changes in both the Lyα and CIV BELs are observed, whereas a significant change in the nearby continuum flux is present. Relative to the initial HSN-spectrum the Lyα BEL flux increased $\sim 2\%$, the nearby continuum flux increased $\sim 23\%$, and the CIV BEL flux decreased $\sim 7\%$. The redshift of the Lyα BEL is consistent with the SDSS redshift, but the redshift of the CIV and NV BEL is somewhat lower. A strong damped Lyα (DLA) absorption-line system, which is intervening and unrelated to the quasar, is identified at a redshift of $z_{abs} = 2.442$.

4.3.5 Correlations and their Dependence on Time Interval and Luminosity

In order to study any correlations that may depend on the time interval between observations and the quasar luminosity, we have formed a new parameter $\Delta\tau' = \Delta\tau/(L_{quasar}/L_{AGN})^{0.5}$. If the variation time increases in proportion to $(L_{quasar}/L_{AGN})^{0.5}$, $\Delta\tau'$ would scale the time intervals to take such an effect into account. We have used $L_{AGN} = 4.2 \times 10^{43}$ ergs s^{-1}, which is the luminosity of NGC 5548 at 1300 Å. We then divide our sample in half according to $\Delta\tau'$. Half of our sample has $\Delta\tau' < 1.35$ days and half has $\Delta\tau' > 1.35$ days. Since we found that changes in the Lyα and CIV BELs are well correlated, we have also averaged the individual change results on Lyα and CIV to form a variance-weighted average ΔF_{BEL}. The correlation between BEL flux changes versus continuum changes are then considered

for our sample for short ($\Delta\tau' < 1.35$ days) and long ($\Delta\tau' > 1.35$ days) luminosity-scaled, rest-frame time intervals. The results are shown in Figure 17. We find that there is a strong correlation between BEL flux change and continuum change when $\Delta\tau' < 1.35$ days (correlation coefficient of 0.77), but the correlation is much weaker when $\Delta\tau' > 1.35$ days (correlation coefficient of 0.30). Thus, the overall trend seen in our sample is for BEL and continuum variations to become less correlated for for the longer luminosity-scaled, rest-frame time intervals. We found this interesting, but the origin of this effect is unclear.

4.4 SUMMARY AND DISCUSSION

We have investigated the variability of the Lyα BEL in a sample of 63 quasars observed at two epochs by the SDSS. The quasars have redshifts that lie in the interval $z = [2.5, 4.3]$ and luminosities greater than $\lambda L_\lambda \sim 2.7 \times 10^{45}$ erg s^{-1} at 1300 Å. Variability of the Lyα BEL is inferred to be ubiquitous in our sample on rest-frame time scales ranging from days to years, with $\sim 33\%$ of the sample showing Lyα BEL variations $> 5\sigma$. Thus, despite some earlier work which reported no significant Lyα BEL flux variations in a similar sample, variability is clearly present and readily observable in high-luminosity, high-redshift quasars.

However, during the work that led us to consider our final sample of 63 quasars, examination of the SDSS sub-exposures led us to conclude that faint ($r > 19.7$ mag) and low signal-to-noise ($S/N < 10$) spectra may produce unreliable results.

In addition to measuring variations in the Lyα BEL, we also measured the corresponding continuum and CIV BEL variations. Even with two-epoch data, some interesting trends are seen in our sample. For example, there is not a strong correlation between Lyα BEL variability and nearby continuum variability, and this is consistent with the presence of a time lag between the variations. However, there is a strong correlation between Lyα BEL variability and CIV BEL variability, and this suggests that these BELRs are at similar distances from the central ionizing source.

Finally, some interesting examples are emphasized in the analysis. For example, in one case (SDSS J004240.65+141529.6) the flux of a Lyα BEL increased by $\sim 26\%$ in only 14

days in the quasar rest frame. This probably indicates that a significant fraction of the Lyα BELR has a correspondingly small size scale along our sightline. In the absence of anisotropic Lyα emission from the BELR, the most likely reason for this fast change would be that the Lyα BELR has the shape of a disk, and we are viewing the disk close to face-on (Section 4.3.4.1). In such a geometry the light travel time across the BELR along our sightline would be $\sim sin(i) D_{\mathrm{Ly}\alpha\ BELR}$, where i is the inclination angle relative to the disk's polar axis and $D_{\mathrm{Ly}\alpha\ BELR}$ is the diameter of the Lyα BELR disk. Thus, for example, this observation appears to be consistent with models where the BELR primarily originates in the chromosphere of a quasar's face-on accretion disk (Murray et al. 1995; Murray & Chiang 1997). If this is the case, such observations may some day provide constraints on quasar inclination angles, or at least allow us to identify quasars that have nearly face-on accretion disks. In any case, this work demonstrates that future campaigns of spectrophotometric monitoring can improve our understanding of the structure of the BELRs of high-luminosity, high-redshift quasars.

4.5 SDSS ACKNOWLEDGMENT

We thank Ching-Wa Yip for providing the wavelength-dependent flux ratio corrections for our sample and all private discussions and Daniel Vanden Berk for some early discussions about variability analysis.

Funding for the SDSS and SDSS-II has been provided by the Alfred P. Sloan Foundation, the Participating Institutions, the National Science Foundation, the U.S. Department of Energy, the National Aeronautics and Space Administration, the Japanese Monbukagakusho, the Max Planck Society, and the Higher Education Funding Council for England. The SDSS Web Site is http://www.sdss.org/.

The SDSS is managed by the Astrophysical Research Consortium for the Participating Institutions. The Participating Institutions are the American Museum of Natural History, Astrophysical Institute Potsdam, University of Basel, University of Cambridge, Case Western Reserve University, University of Chicago, Drexel University, Fermilab, the Institute for Ad-

vanced Study, the Japan Participation Group, Johns Hopkins University, the Joint Institute for Nuclear Astrophysics, the Kavli Institute for Particle Astrophysics and Cosmology, the Korean Scientist Group, the Chinese Academy of Sciences (LAMOST), Los Alamos National Laboratory, the Max-Planck-Institute for Astronomy (MPIA), the Max-Planck-Institute for Astrophysics (MPA), New Mexico State University, Ohio State University, University of Pittsburgh, University of Portsmouth, Princeton University, the United States Naval Observatory, and the University of Washington.

Table 1. Flux ratios for four quasars and surrounding compact objects before and after the gray recalibration correction.

	Quasars		Compact Objects			
	SDSS J	C_{band}^{before} [1]	SDSS J	C_{band}^{before} [1]	$\overline{C}_{band}^{before}$ [2]	$\overline{C}_{band}^{after}$ [3]
1	004240.65+141529.6	0.908	003408.61+134839.0	0.986	0.984±0.015	1.000±0.015
			003448.91+134439.3	0.955		
			003441.35+153517.8	1.055		
			003651.49+145035.9	0.986		
			003854.02+143742.9	0.969		
			003707.21+155552.5	0.951		
2	132750.44+001156.8	1.286	132456.66−010534.6	1.185	1.177±0.012	1.000± 0.010
			132304.59+000924.5	1.119		
			132634.99−011108.2	1.127		
			132730.91−011024.8	1.218		
			132404.47−004428.8	1.179		
			132510.57−003233.6	1.202		
			133136.77+001959.3	1.206		
3	095106.32+541149.8	1.188	094420.28+540810.2	1.193	1.172±0.029	1.000±0.025
			094659.80+544546.7	1.191		
			094920.08+543803.2	1.030		
			095003.13+541821.7	1.217		
			095253.45+550957.7	1.231		
4	120802.64+630328.9	1.264	115510.14+624653.5	1.048	1.047±0.002	1.000±0.002
			120039.52+623428.5	1.113		
			121642.58+623405.9	0.978		
			121425.49+623009.0	1.050		

Note. — We use the rest-frame wavelength bands at 1260−1285Å, 1318−1380Å, 1430−1525Å and 1580−1620Å, ensuring no prominent emission lines at the chosen regions in four quasars.

[1]Flux ratio C_{band}^{before} of each object before recalibration using the method of Yip et al. (2009).

[2]Mean of C_{band}^{before} of the compact objects in each group before recalibration using the method of Yip et al. (2009).

[3]Mean of C_{band}^{after} of the compact objects in each group after applying the recalibration.

Table 2. BEL and continuum flux measurements for four quasars after recalibration using surrounding compact objects.

		MJD			$\Delta\tau$		$\lambda L_{1300\AA}$	HSN-epoch				LSN-epoch			
	SDSS J	HSN	LSN	z_{em}	(days)	r	(ergs s^{-1})	$F_{Ly\alpha}$	$F_{c1300\AA}$	F_{CIV}	$F_{c1600\AA}$	$F_{Ly\alpha}$	$F_{c1300\AA}$	F_{CIV}	$F_{c1600\AA}$
	(1)	(2)	(3)	(4)	(5)	(6)	(7)	(8)	(9)	(10)	(11)	(12)	(13)	(14)	(15)
1	004240.65+141529.6	51817	51884	3.70	14.08	19.20	7.72×10^{45}	6.15±0.11	4.55±0.05	1.77±0.08	3.87±0.06	4.52±0.10	4.28±0.06	1.49±0.07	3.78±0.05
2	132750.44+001156.8	51959	51663	2.53	83.88	18.44	9.71×10^{45}	9.93±0.23	17.56±0.14	0.83±0.15	13.93±0.10	7.43±0.23	15.55±0.15	0.84±0.16	13.20±0.11
3	095106.32+541149.8	54530	52282	2.69	609.65	18.89	8.59×10^{45}	23.28±0.18	12.45±0.09	6.29±0.11	9.71±0.08	18.69±0.21	12.37±0.12	5.26±0.16	9.93±0.11
4	120802.64+630328.9	52337	54525	2.57	612.65	17.70	3.31×10^{46}	46.93±0.31	48.48±0.17	16.59±0.22	36.96±0.12	47.78±0.37	59.65±0.20	17.68±0.24	43.64±0.15

Note. — All flux units are in 10^{-17} erg s^{-1} cm^{-2} Å^{-1}.

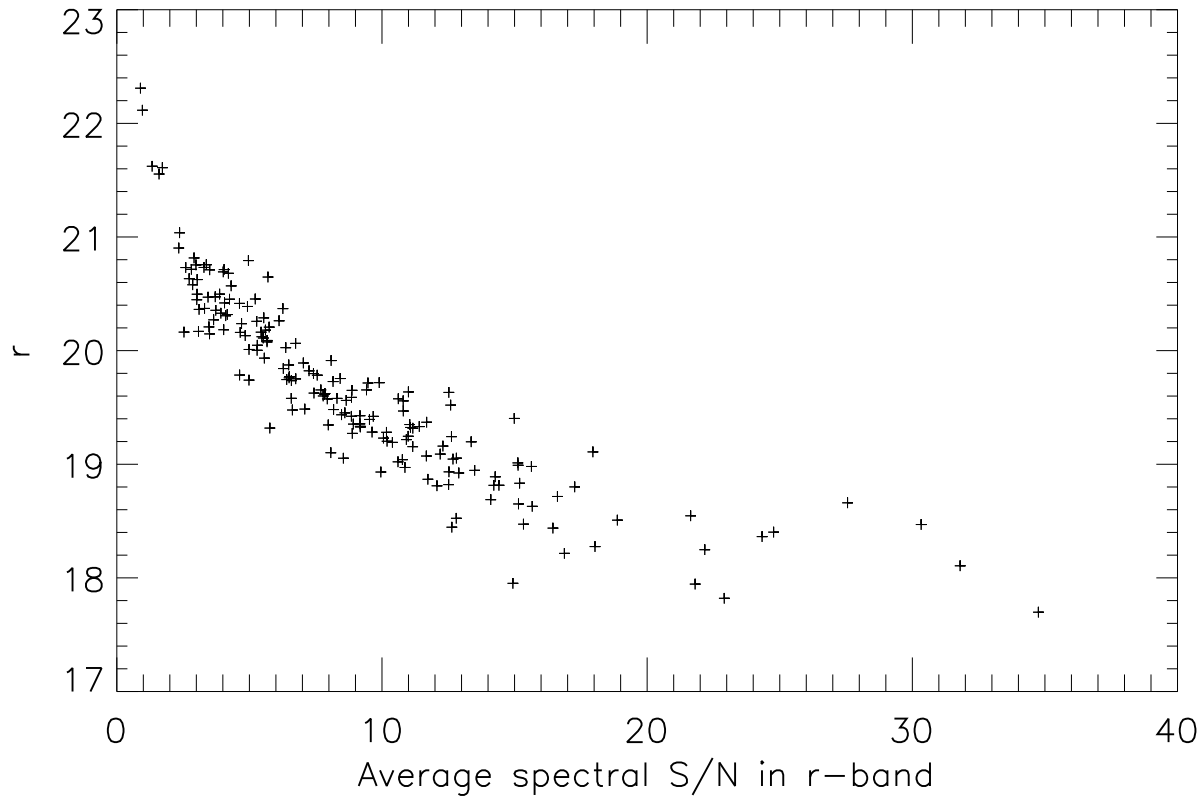

Figure 7 Average SDSS $r-$band magnitude measured from the spectra at two epochs versus average spectral S/N. Objects with $S/N < 10$ and r fainter than ~ 19.7 mag are eliminated from the final sample to avoid possible false-positive results on variability due to sky subtraction residuals.

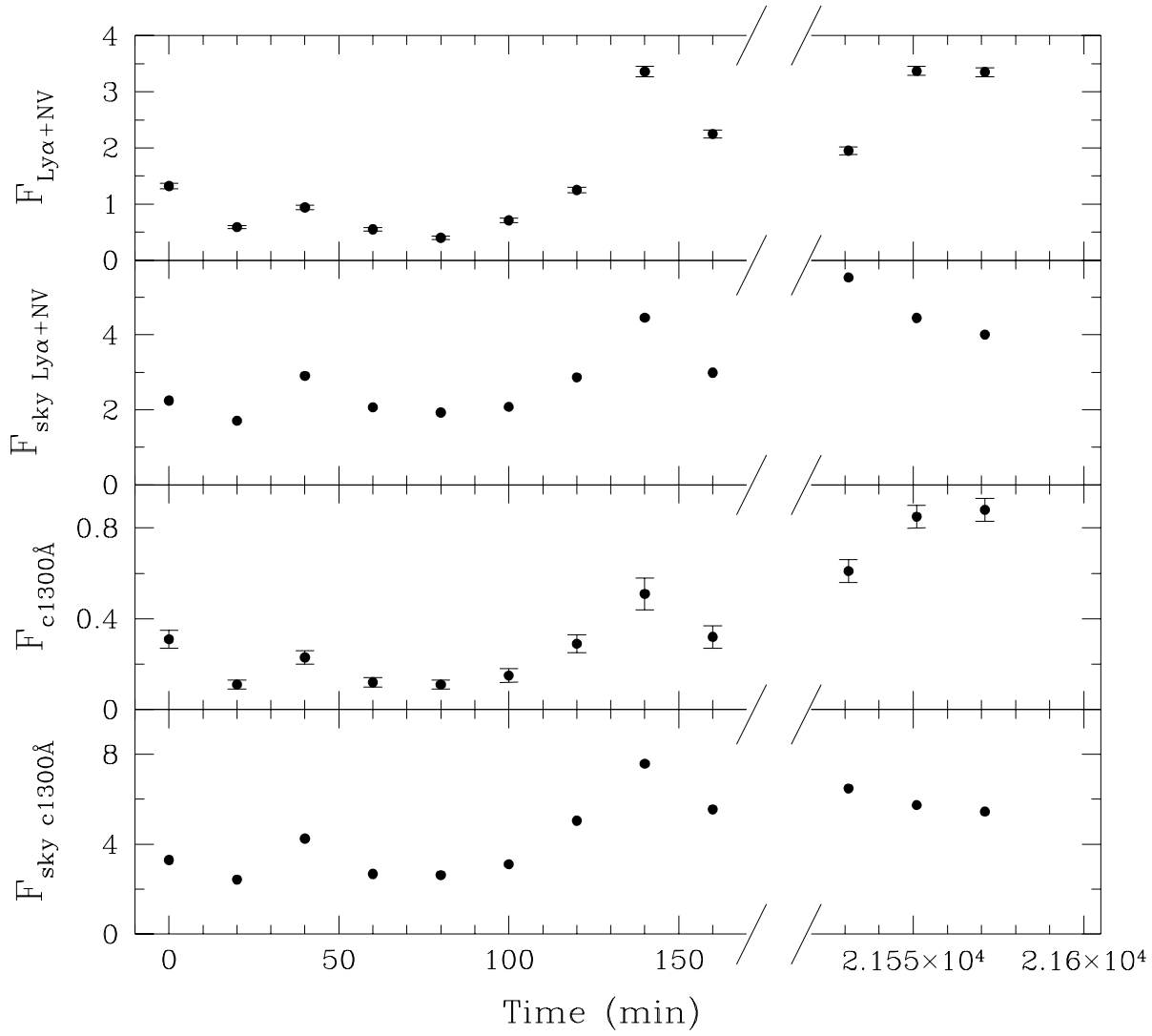

Figure 8 Faint quasar SDSS J101840.46+285000.7 with flux variations correlated to sky fluctuations in Lyα + Nv BEL regions (top two) and nearby continuum regions (bottom two), respectively, over 12 sub-exposures. The unit of flux is $10^{-17}\,\mathrm{erg\,s^{-1}\,cm^{-2}\,\AA^{-1}}$.

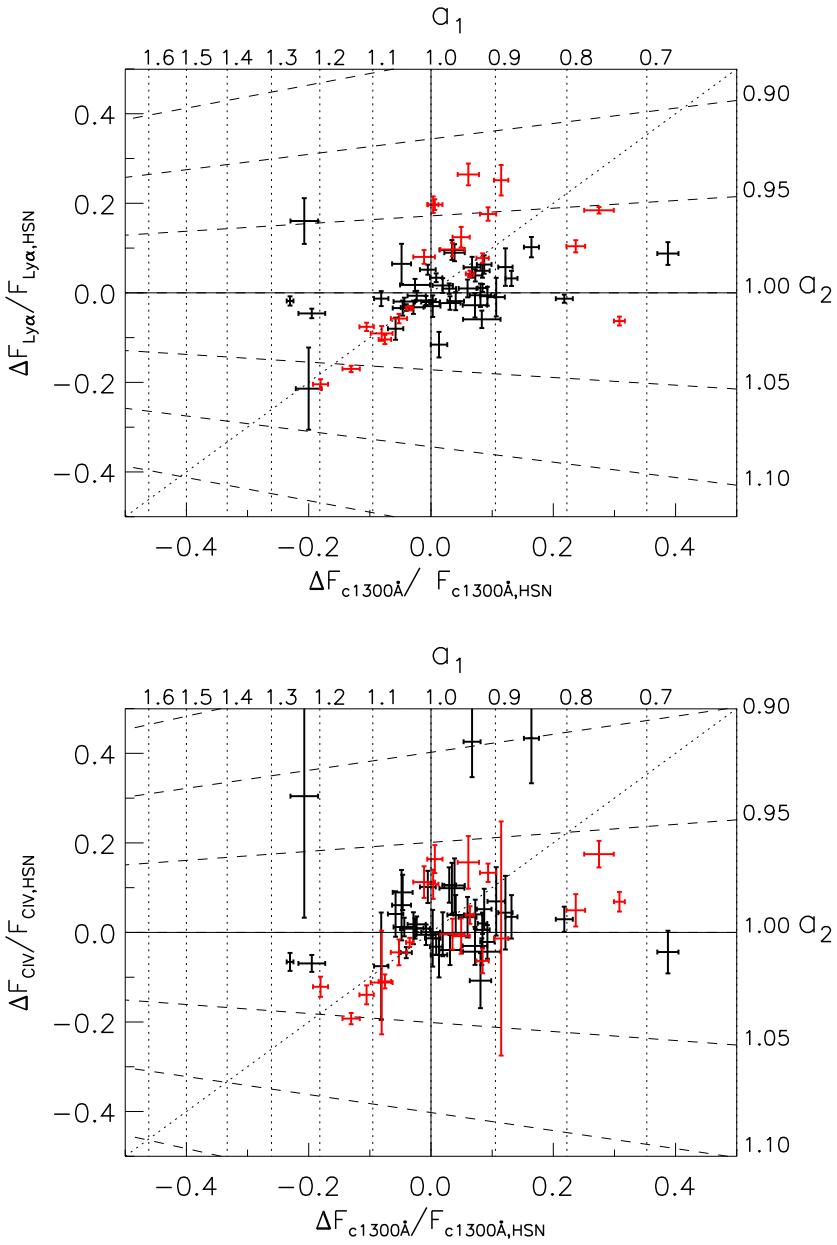

Figure 9 Top: The distribution of normalized Lyα BEL flux changes vs. normalized continuum flux changes for 63 quasars. Twenty-one quasars (red points) exhibit Lyα BEL flux variations at a significance level $> 5\sigma$. Bottom: The distribution of normalized CIV BEL flux changes vs. normalized continuum flux changes for 63 quasars. The data shown in red are the same data as above. We have parameterized flux changes in a hypothetical Lyα BEL profile and the associated nearby continuum in the parameter space of a_1 and a_2. See the details in the text.

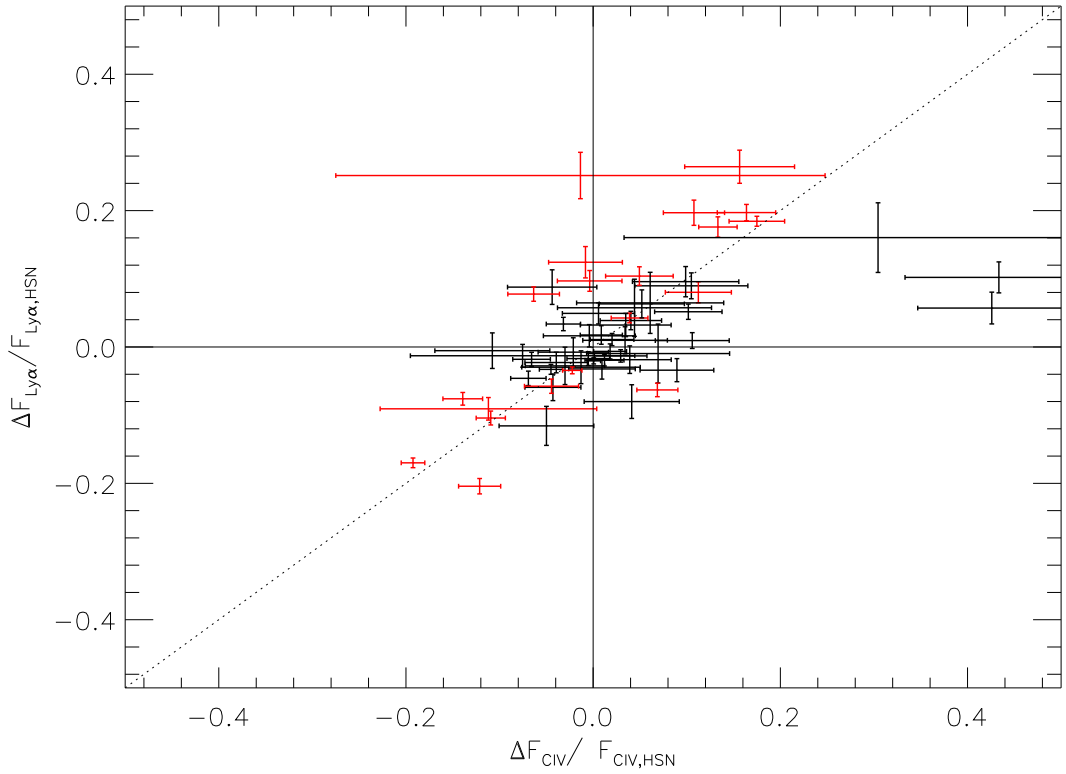

Figure 10 Fractional change in Lyα BEL flux vs. fractional change in CIV BEL flux between two epochs. As in Figure 9, the red points are those with Lyα BEL flux changes $> 5\sigma$.

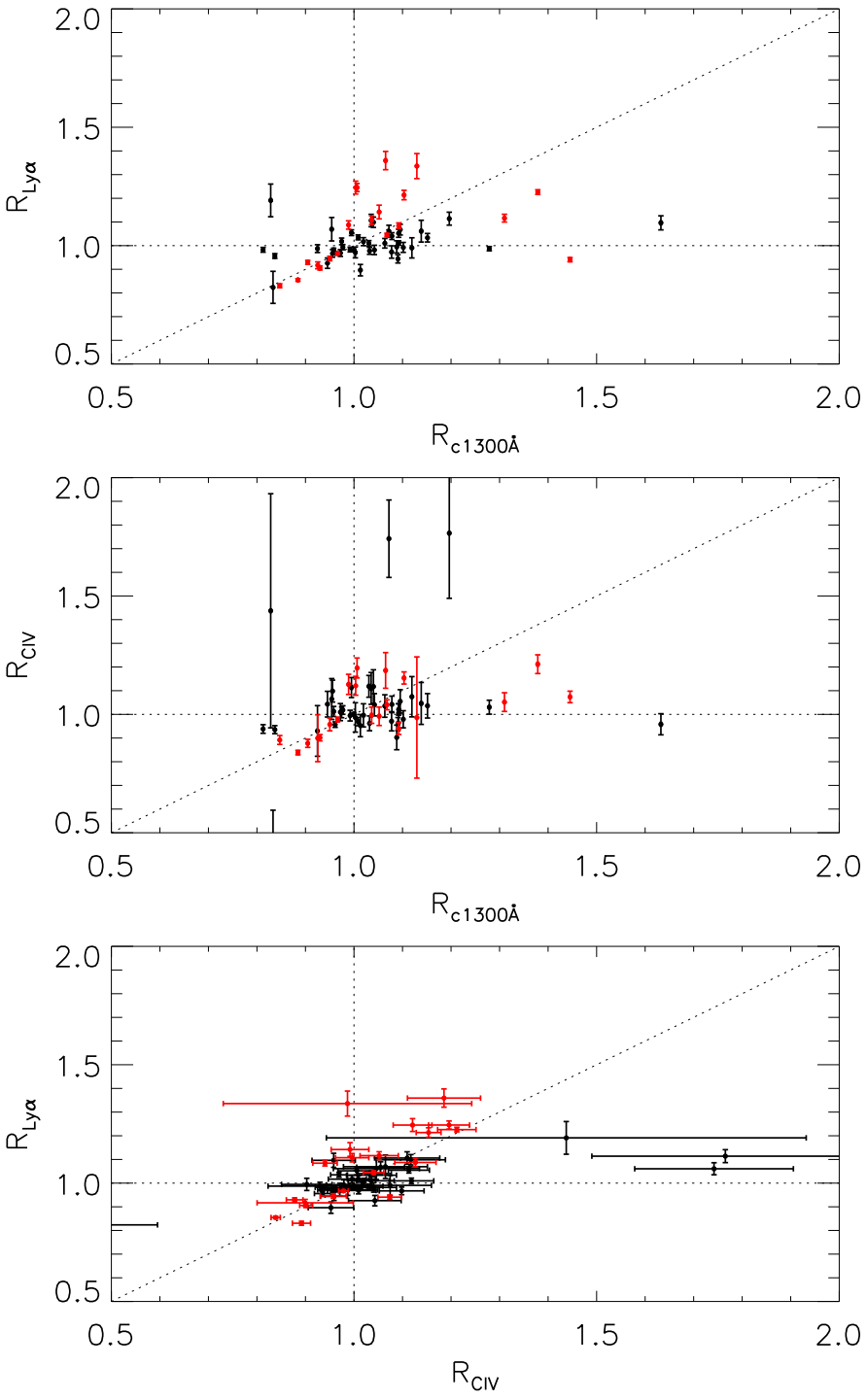

Figure 11 Top: Lyα BEL flux ratio vs. continuum flux ratio. Middle: CIV BEL flux ratio vs. continuum flux ratio. Bottom: Lyα BEL flux ratio vs. CIV BEL flux ratio. As in Figures 9 and 10, the red points are those with Lyα BEL flux changes $> 5\sigma$.

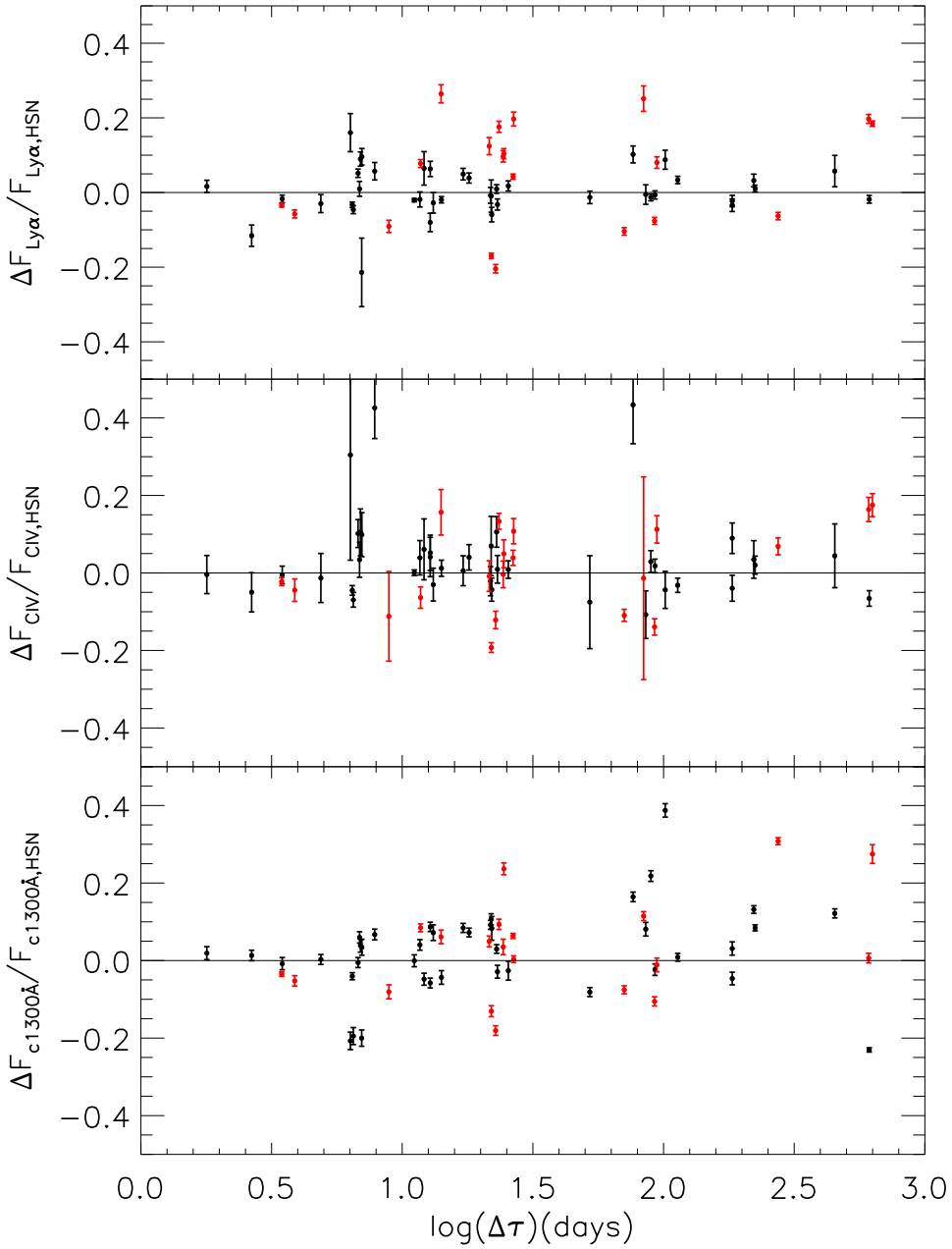

Figure 12 Top: Fractional change in Lyα BEL flux as a function of time between observation epochs in the quasar rest frame in logarithmic scale, $\log(\Delta\tau)$. Middle: Fractional continuum changes vs. $\log(\Delta\tau)$. Bottom: Fractional CIV BEL flux vs. $\log(\Delta\tau)$. As in Figures 9–11, the red points are those with Lyα BEL flux changes $> 5\sigma$.

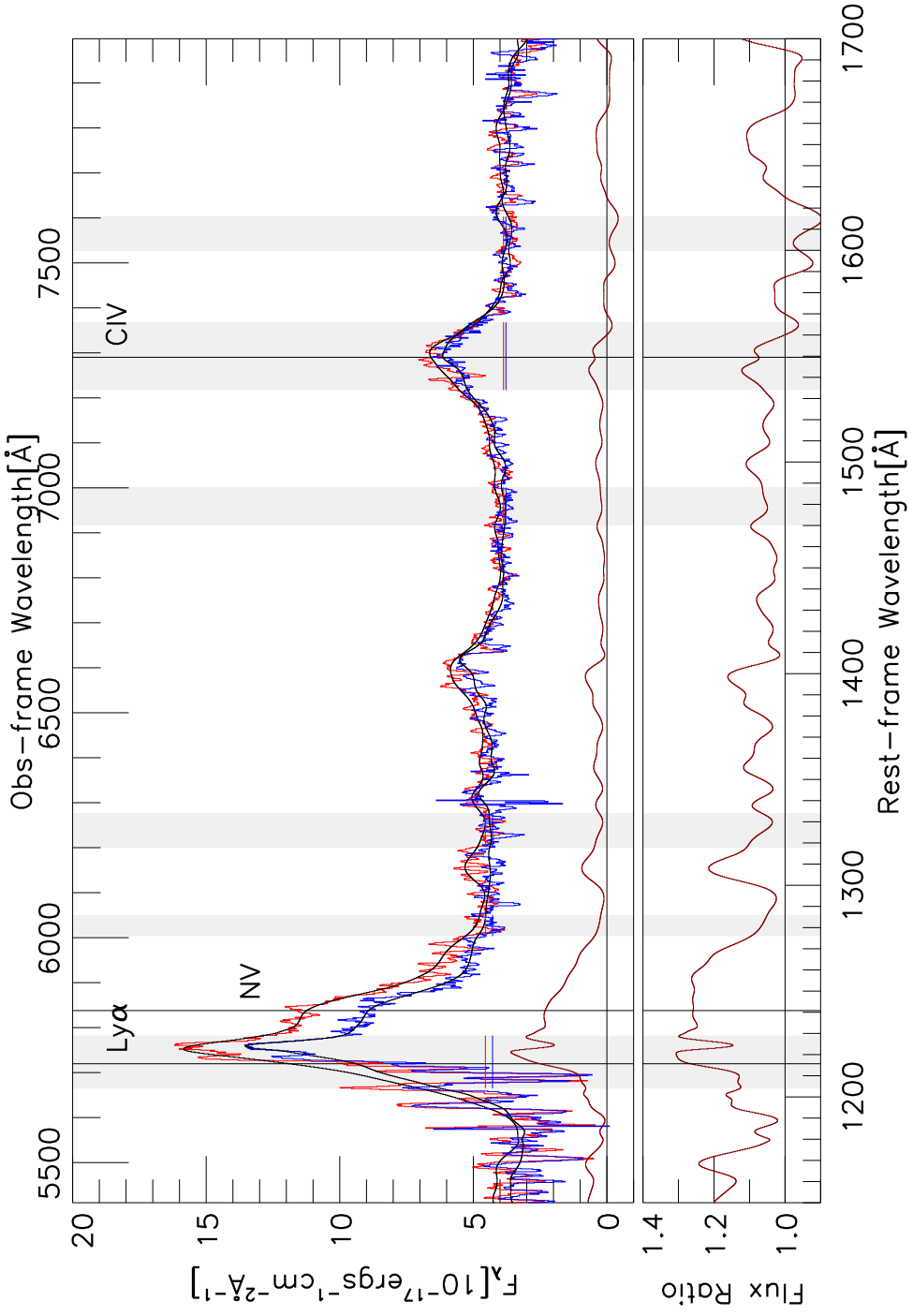

Figure 13 (1) Top: Spectra of SDSS J004240.65+141529.6 at the first HSN-epoch (red) and the second LSN-epoch (blue), and their difference (dark red). Bottom: ratio spectrum.

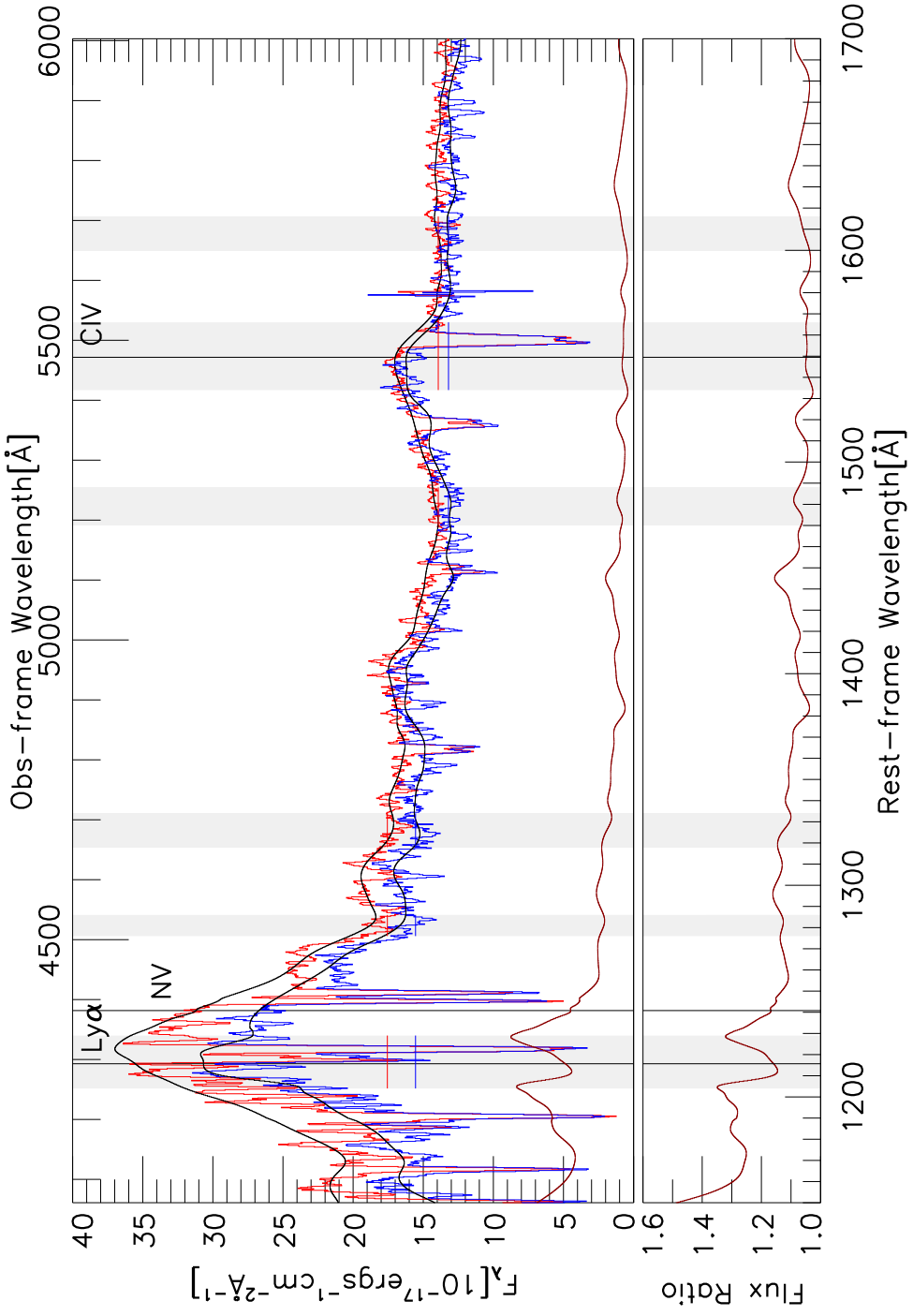

Figure 14 (2) Top: Spectra of SDSS J132750.44+001156.8 at the first LSN-epoch (blue) and the second HSN-epoch (red), and their difference (dark red). Bottom: ratio spectrum.

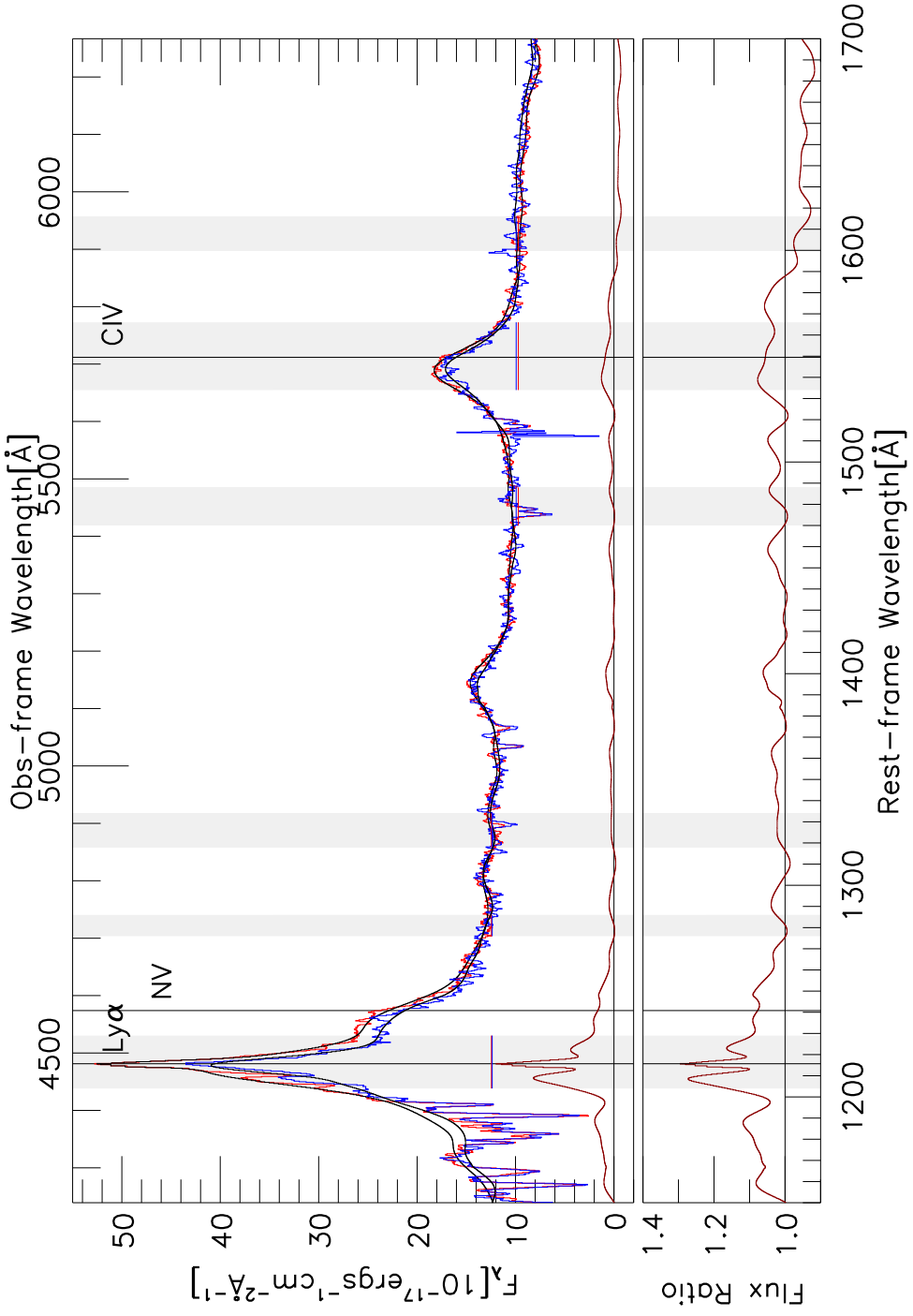

Figure 15 (3) Top: Spectra of SDSS J095106.32+541149.8 at the first LSN-epoch (blue) and the second HSN-epoch (red), and their difference (dark red). Bottom: ratio spectrum.

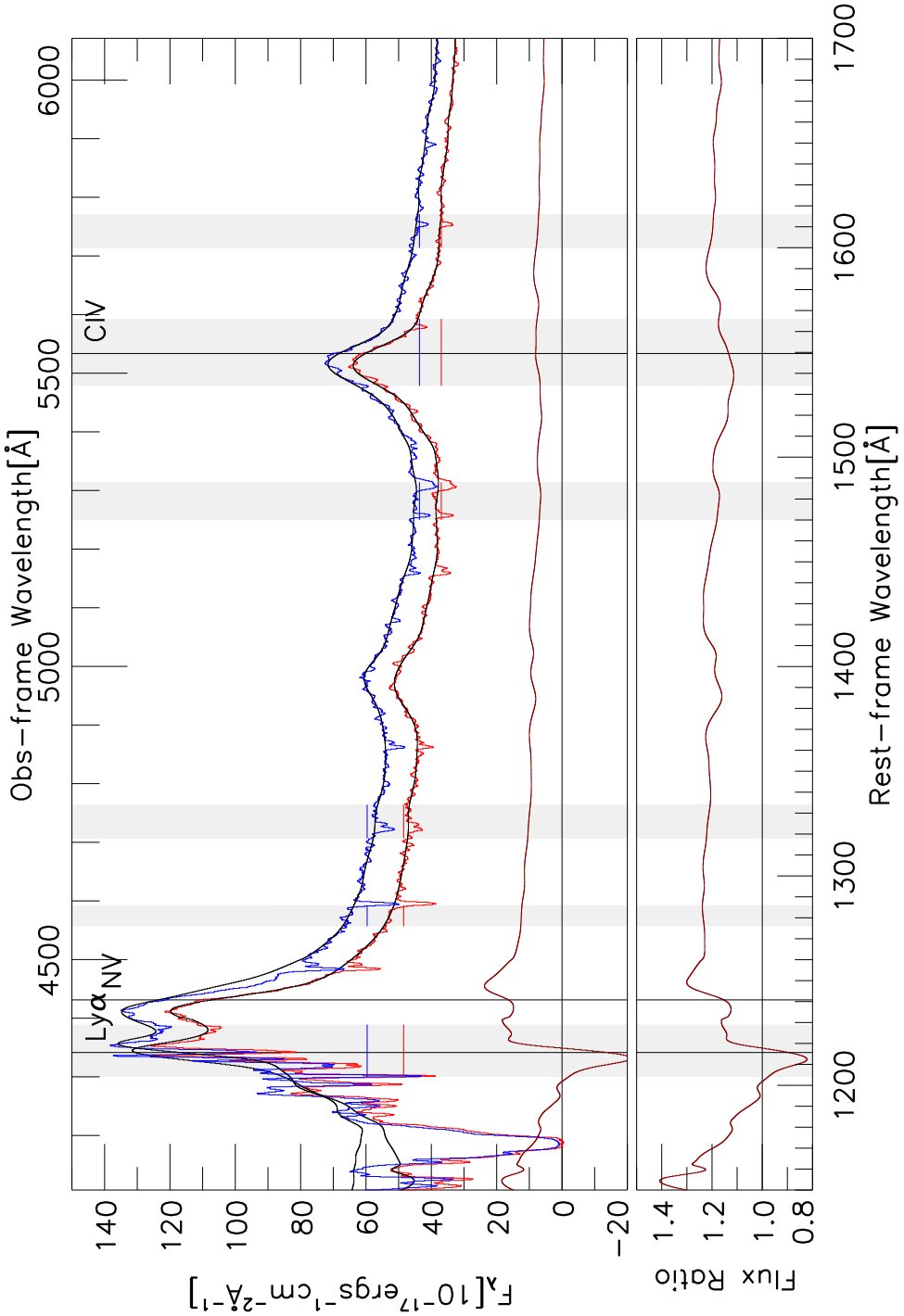

Figure 16 (4) Top: Spectra of SDSS J120802.64+630328.9 at the first HSN-epoch (red) and the second LSN-epoch (blue), and their difference (dark red). Bottom: ratio spectrum.

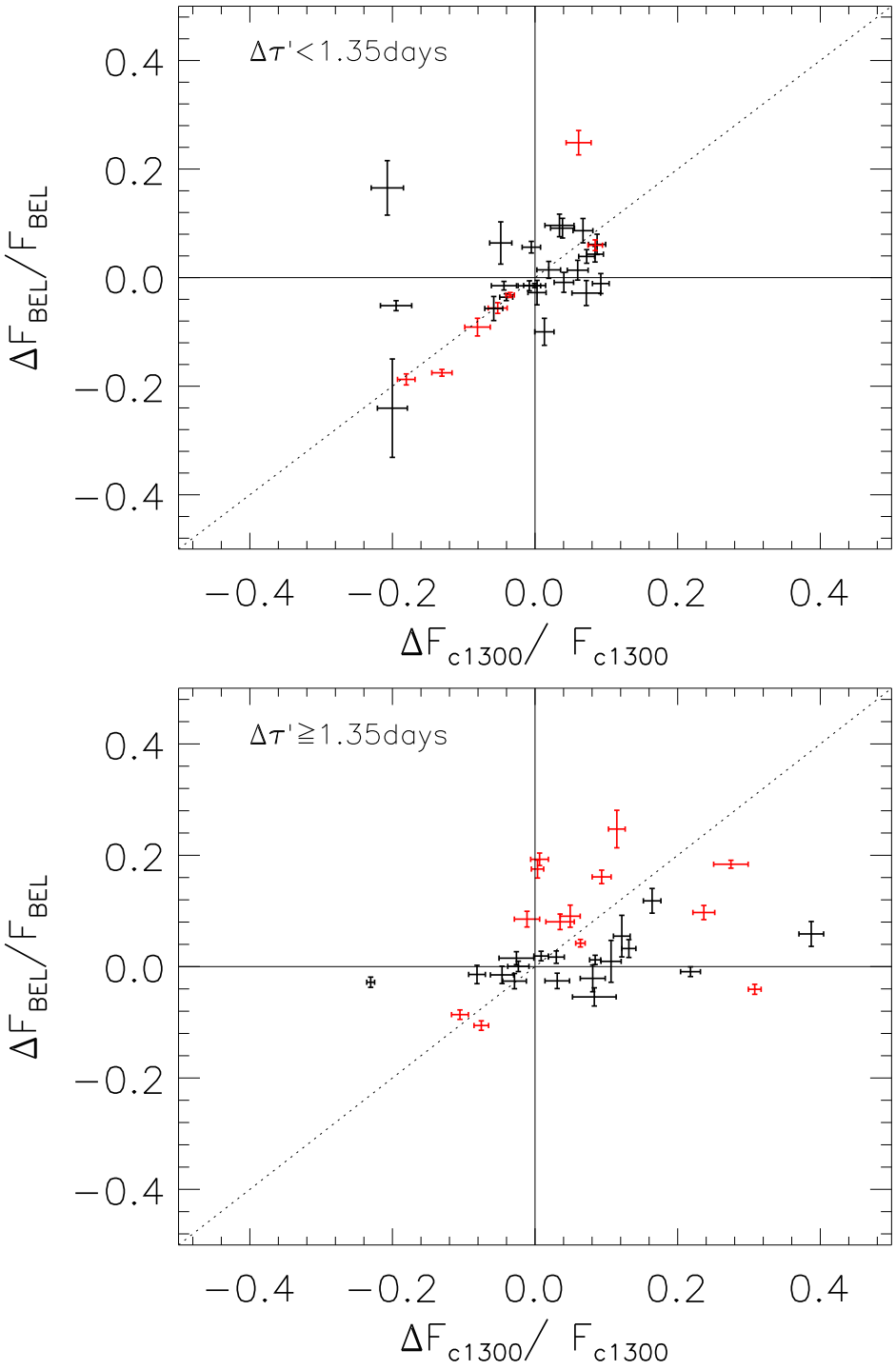

Figure 17 Top: Fractional change in BEL flux vs. fractional change in continuum between two epochs for 30 quasars with $\Delta\tau' < 1.35$ days. Bottom: same as above for 33 quasars with $\Delta\tau' \geq 1.35$ days. As in Figures 9–12, the red points are those with Lyα BEL flux changes $> 5\sigma$.

5.0 EMPIRICAL MODEL

In Chapter 4 I verified that there is a strong correlation between Lyα BEL variability and CIV BEL variability, suggesting that these BELRs are at similar distance from the central source. Combining the findings with results on CIV BELR distance for high luminosity, high redshift quasars from Kaspi et al. (2007), I was able to constrain the BELR size scale for the Lyα BEL in high-luminosity, high-redshift quasars and subsequently constrain the size scale of the NV BALR.

In this Chapter, to understand the geometrical relationship between the BELRs and the accretion disk (AD), I build the empirical model composed of three components: the continuum emission in the optical/UV from the accretion disk, the BELR from the accretion-disk wind, and the outflowing BALR. I extensively explore the free parameters in the simulation of each component. Based on the knowledge that the size scale of the Lyα BELR is similar to the reverberation distances of CIV BELRs, the three-component model can put constraints on the size scales of the continuum emitting region and BELRs for a SMBH with a typical mass of $\sim 10^8 M_\odot$. Given the fact that the BALR lies outside the BELR, in particular, the absorption trough of NV BEL is able to occult the continuum and the Lyα BELR, I can constrain the location of the NV BALR relative to the continuum emission and BELRs. Moreover, using the physical conditions of the BALRs from classical and other intrinsic absorbers, such as the electron density, ionization parameter and covering factor, the minimum distance of the BALRs from the central source can be inferred.

In the empirical model described here, a number of free parameters have to be constrained by making several assumptions and these will be discussed in context. The inclination angle i of the disk to the observer's line of sight is the most crucial parameter; it determines the amount of flux from the BELR that reaches the observer and also the strength of all

relativistic effects in the BELR. Larger fluxes are obtained when the observer views a nearly a face-on disk as opposed to an edge-on disk, whereas the relativistic effects will be more prominent if a disk is viewed at a high inclination (i.e., an edge-on view). For instance, with the viewing angle at 60° from the disk axis, the observed BELR flux will decrease by a factor of 2 compared to the flux when viewed face-on. Therefore, I am interested in investigating how the inclination effect is responsible for the properties of the emission lines appearing in the spectra as well as the slope of the continuum emission of a quasar. Different inclination angles (i.e., i=0°, 15°, 30°, 45°, 60°, and 75°) will be tested thoughtfully. In the unified model of AGNs, a torus is suggested to lie in the disk plane. It provides the obscuration of the disk when the observer's sightline intersects it. Such toroidal obscuration can place a lower limit of the viewing angle, which is the opening angle of the torus.

5.1 DISK CONTINUUM

5.1.1 Relativistic Accretion Disk Emission Formalism

The optical to UV continuum emission of quasars is often called the "big blue bump". It arises in the AD surround the SMBH (Koratkar & Blaes 1999; Shields 1978; Sun & Malkan 1989; Laor 1990, and references therein). The AD is assumed to be geometrically thin, optically thick, Keplerian, stationary, and axisymmetric. In the simplest model, the continuum flux in the optical/UV can be calculated by treating the entire AD as a multi-temperature blackbody, where the temperature is a function of distance from the SMBH; each surface element of the AD emits the Planck radiation B_ν at the local effective temperature $T_{\rm eff}(R)$ as a function of radius R of the disk. As such the specific luminosity of the AD is

$$L_\nu = 4\pi^2 \int_{r_i}^{r_o} B_\nu(T_{\rm eff}(R)) R \, {\rm d}R, \tag{5.1}$$

where r_i and r_o are the inner and outer radii of the AD, respectively.

With knowledge of the physical size and temperature structure of the AD, the total continuum flux can be computed. In accretion disk physics, the accreting material loses the

angular momentum through local viscous friction, and converts gravitational energy into heat and that raises the disk temperature. In this process, Shakura & Sunyaev (1973) introduced the simple α-model to describe how the AD radiates through the turbulent viscosity of the disk. Here α refers to an assumed constant of proportionality between the accretion stress and total pressure. Under the assumption that the generated radiation flows vertically inside a thin disk, the surface flux F with effective temperature $T_{\rm eff}$ as a function of distance R is then formulated as

$$F = \sigma_S T_{\rm eff}^4(R) = \frac{3GM_{\rm BH}\dot{M}_{acc}}{8\pi R^3} \times f(r_i, a_*). \tag{5.2}$$

The temperature only depends on the physical parameters of the accretion system: the BH mass M_{BH}, and the accretion rate $\dot{M}_{acc}$, with no knowledge of the internal disk structure and magnetic/turbulent viscosity. The boundary condition $f(r_i, a)$ is a correction factor that depends on assumptions about the torque at the innermost stable circular orbit of the disk r_i and the angular momentum per unit BH mass a_*. At the inner boundary of the AD, the innermost stable circular orbit is also determined by the rotation of the BH. Wherein zero stress is assumed to be exerted on the disk, such that material falls directly into the BH with less or no radiation given out.

For a Newtonian thin disk, the correction factor is simply $1 - \sqrt{r_i/R}$, which approaches unity at large radii R but achieves zero at the innermost radius. For a nonrotating (Schwarzschild) BH, the innermost edge is $r_i = 6GM_{BH}/c^2$, while for a rapidly rotating (Kerr) BH, the innermost edge is roughly smaller by a factor of five, i.e., $r_i = 1.23GM_{BH}/c^2$, thus leading to more prominent gravitational effects. Since the accreting matter spins up the central BH (Bardeen 1970), the latter case is preferable as well as more realistic.

Due to the strong gravity of the SMBH, Newtonian physics is unlikely to be a good approximation to the spectrum at each radius, and relativistic effects must be included. The radial structure of the AD and thus the disk temperature will be modified. Gravitational light bending will change the flux distribution through absorption and reprocessing, as will flaring or warping of the outer disk. In this empirical model, we adopt the relativistic radial disk structure equations of Novikov & Thorne (1973, hereafter NT73) and Page & Thorne

(1974, hereafter PT74) to calculate the emergent flux F produced by the AD at each radius R. Equation (5.1) for the surface flux is modified to become

$$F(R) = \frac{3GM_{\rm BH}\dot{M}_{acc}}{8\pi R^3}\frac{Q}{BC^{1/2}}, \tag{5.3}$$

where B, C and Q are the general relativistic correction factors defined in NT73 and PT74, and all of the factors are approaching 1 at the Newtonian limit at $R >> r_i$. The integrated disk spectrum is obtained by summing the local emergent flux from a series of radii each with $T_{\rm eff} = [F(R)/\sigma_S]^{1/4}$ and correction factors:

$$\begin{aligned}
B &= 1 + a_*/x^3 \\
C &= 1 - \frac{3}{x^2} + 2\frac{a_*}{x^3} \\
Q &= \frac{1 + a_* x^{-3}}{(1 - 3x^{-2} + 2a_* x^{-3})^{1/2}}\frac{1}{x}\left[x - x_0 - \frac{3}{2}a_* \ln\left(\frac{x}{x_0}\right) - \frac{3(x_1 - a_*)^2}{x_1(x_1 - x_2)(x_1 - x_3)}\ln\left(\frac{x - x_1}{x_0 - x_1}\right)\right. \\
&\quad \left. - \frac{3(x_2 - a_*)^2}{x_2(x_2 - x_1)(x_2 - x_3)}\ln\left(\frac{x - x_2}{x_0 - x_2}\right) - \frac{3(x_3 - a)^2}{x_3(x_3 - x_1)(x_3 - x_2)}\ln\left(\frac{x - x_3}{x_0 - x_3}\right)\right],
\end{aligned}$$

where $-1 \leq a \leq +1$, $x = (R/r_g)^{1/2}$ where $r_g = GM_{BH}/c^2$, and x_1,x_2,x_3 are the three roots of $x^3 - 3x + 2a_* = 0$.

Figures 18 and 19 show the disk temperature as a function of the radius in a Schwarzschild geometry (i.e., $a_* = 0$) and a Kerr geometry (i.e., $a_* = 0.988$), respectively. Knowing the temperature structure of the relativistic case, I use blackbodies to describe the local emergent fluxes and calculate the spectra of the disk at different viewing angles, which are then corrected for the propagation of photons as influenced by the strong gravitational field of the SMBH (Cunningham 1975). Based on the Cunningham (1975) formalism for the general relativistic effects, Speith et al. (1995) developed an open-source code to compute the continuum emission from a relativistic AD through a transfer function that embodies photon transport under the influence of relativistic effects, including Doppler boosting, gravitational redshifts and gravitational focusing. Users can define a specific intensity I_ν, an angular momentum a_* of the BH, and the disk inclination i to the observer's line of sight in the code, and then the total flux of continuum emission can be computed. In this part of the calculation, I employ the Speith et al. (1995) code with a slight modification. I divide the

disk into 20 concentric annuli and compute the emission flux for individual annuli. From this stimulated result for the continuum flux we can estimate the size scale of the AD where the optical/UV emission mainly originates. However, fitting detailed spectral slopes to individual observed spectral energy distributions (SEDs) remains a challenge.

5.1.2 Parameters for the Accretion Disk Model

In the stimulation, there are three crucial parameters to be defined: $\dot{m}$, a_* and r_o, which are explored extensively, and are discussed as follow:

1. The parameter $\dot{m}$ is the normalized accretion rate used with the SMBH mass to determine the disk temperature structure, which defines the shape of UV to optical spectra.[1] In the SED of a typical quasar, the optical tail has a slope of $F_\nu \propto \nu^{1/3}$, and the UV emission indicates a turnover toward short wavelengths. The simplest thin AD models around a SMBH of $M \geq 10^6 M_\odot$ do not often produce the expected slope throughout the optical/UV region. In order for the disk not to produce so much radiation pressure that it becomes geometrically thick, the accretion mass rate is limited to about 0.2–0.3 times the Eddington mass rate. With this limit, however, I demonstrate that the SED in the optical/UV can be significantly redder than the $\nu^{1/3}$ prediction, particularly when viewed face-on as shown in Figures 20 and 21. These figures show that the disk is so cool that the short wavelength ultraviolet turns down at $\sim 1000\,\text{Å}$, resulting in a red slope. It is noted that the turn-over peak is shortward of Lyα which is the spectral region we are interested in investigating later. When we adjust the accretion rate to be the Eddington limit, the optical/UV continuum will get harder as shown in Figures 22 and 23. Therefore, varying the maximum temperature by varying the accretion rate will change the overall slope of the spectrum. However, in most luminous quasars, such disks accreting at the Eddington limit are probably not sufficiently luminous. Alternatives to address the deficiencies of standard accretion disk models have been explored by Koratkar & Blaes (1999, and reference therein). Additional emissions, dust reddening,

[1] For a black hole of mass M_{BH}, it is useful to scale R with the gravitational radius $r_g \equiv GM/c^2$ and $\dot{M}_{acc}$ with $\dot{M}_{Edd} \equiv L_{Edd}/c^2 = 4\pi GM/(c\kappa_{es})$, where κ_{es} is the electron scattering opacity per mass. The scalings are $\dot{m} \equiv \dot{M}_{acc}/\dot{M}_{Edd}$ and $r = R/r_g$

reprocessing, nonstationary accretion disks, slim disks, and truncation of the inner disk can substantially alter the observed slope (Blaes 2004). Nevertheless, the standard AD assumption is still valid for our stimulation that provide an initial assessment of the location of the optical/UV continuum emission from the AD. We expect that continuum emission should be mostly from the inner portion of the AD, with a scale that is a factor of ~ 100 times smaller than the broad emission-line region.

2. The parameter $a_* = cJ/GM^2$ is the black hole spin parameter, which determines the relativistic effects. There are two extreme cases: a non-rotating (Schwarzschild) BH with $a_* = 0$, and a maximally rotating (Kerr) BH with $a_* = 0.988$. Unfortunately the distribution of a_* is highly uncertain. Estimates for a_* in AGN are limited to a handful of bright, relatively nearby sources with broad Fe Kα lines, as the line shape is sensitive to the spin of the BH (Laor 1991). Observations infer very high values of a_* with unity, for example, MCG−6-30-15 (Tanaka et al. 1995). Although there are considerable uncertainties, a combination of empirical and theoretical arguments seem to favor $a_* \sim 0.9$ (Gammie et al. 2004). Given the large uncertainties, we simply choose the Kerr case which is more realistic, since the accreting matter soon spins the BH up to this limiting value (Bardeen 1970).

3. The parameter r_o is the outer radius of the disk, and thus influences the amount of the computed flux. Computationally, a higher disk luminosity can be obtained by defining a larger disk surface. In thin-disk models, this distance corresponds to a radius where the disk becomes gravitationally unstable and the BELR is produced above (Collin & Huré 2001; Kawaguchi et al. 2004). The authors suggested the location of the unstable disk region at few thousands of gravitational radius r_g. Morgan et al. (2010) found similar results for the AD size from observations. Therefore, in the simulation, we consider the outer boundary of the AD to be $2 \times 10^4 r_g$, and we also verify that the total flux is increased by less than 1% by increasing the outer radius by 10% in the Schwarzschild and Kerr cases shown in Figures 24 and 25.

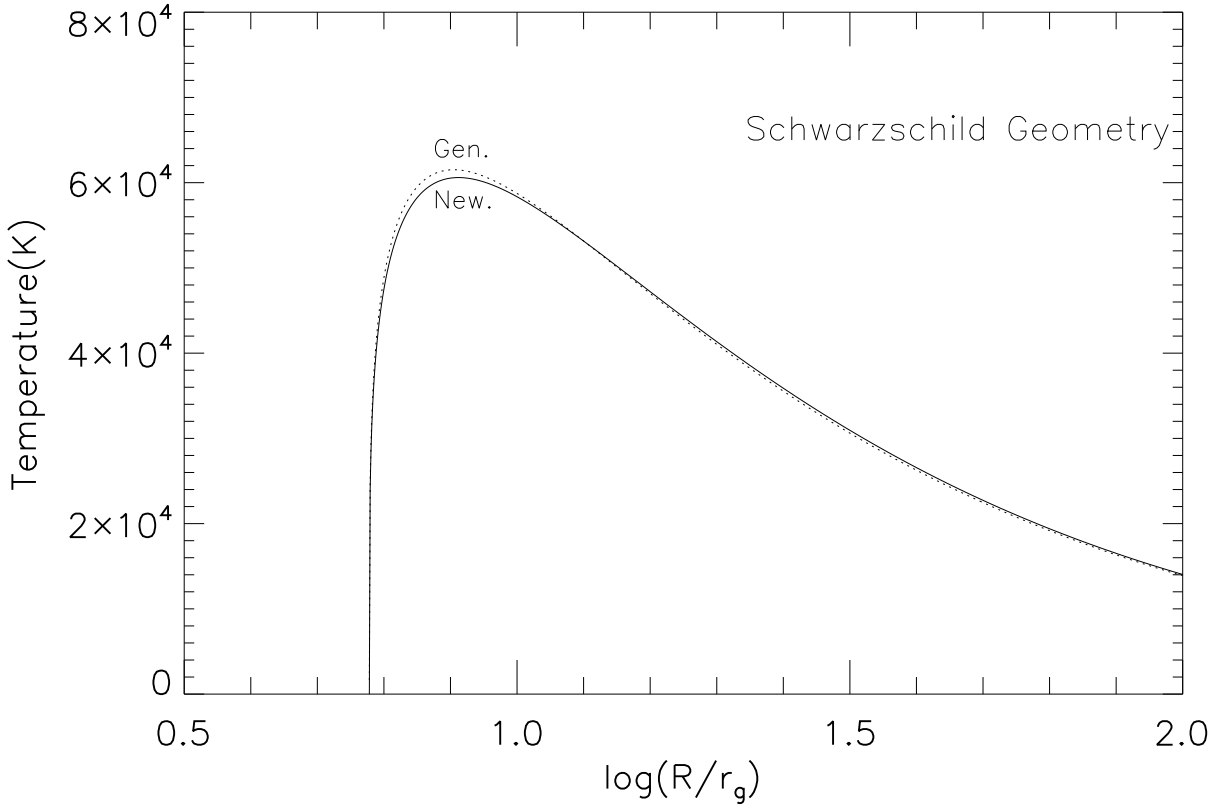

Figure 18 The disk temperature as a function of the radius in a Schwarzschild geometry, where Gen. refers to General Relativity and New. refers to Newtonian.

5.2 BROAD EMISSION LINES

5.2.1 BELR Geometry

Together with the well defined reverberation mapping distance of the BELRs mentioned in Chapter 3, the emission line profiles can be simulated by making appropriate assumptions for the geometry of the BELRs. Due to their broad widths the BELs are widely believed to arise from a rapidly rotating AD in the vicinity of a SMBH. As such these emission lines are often expected to be double-peaked, wherein their cores are suppressed and their wings are enhanced due to the lower projected rotation velocity at the near ($\phi' = 0°$) and far ($\phi' = 180°$)

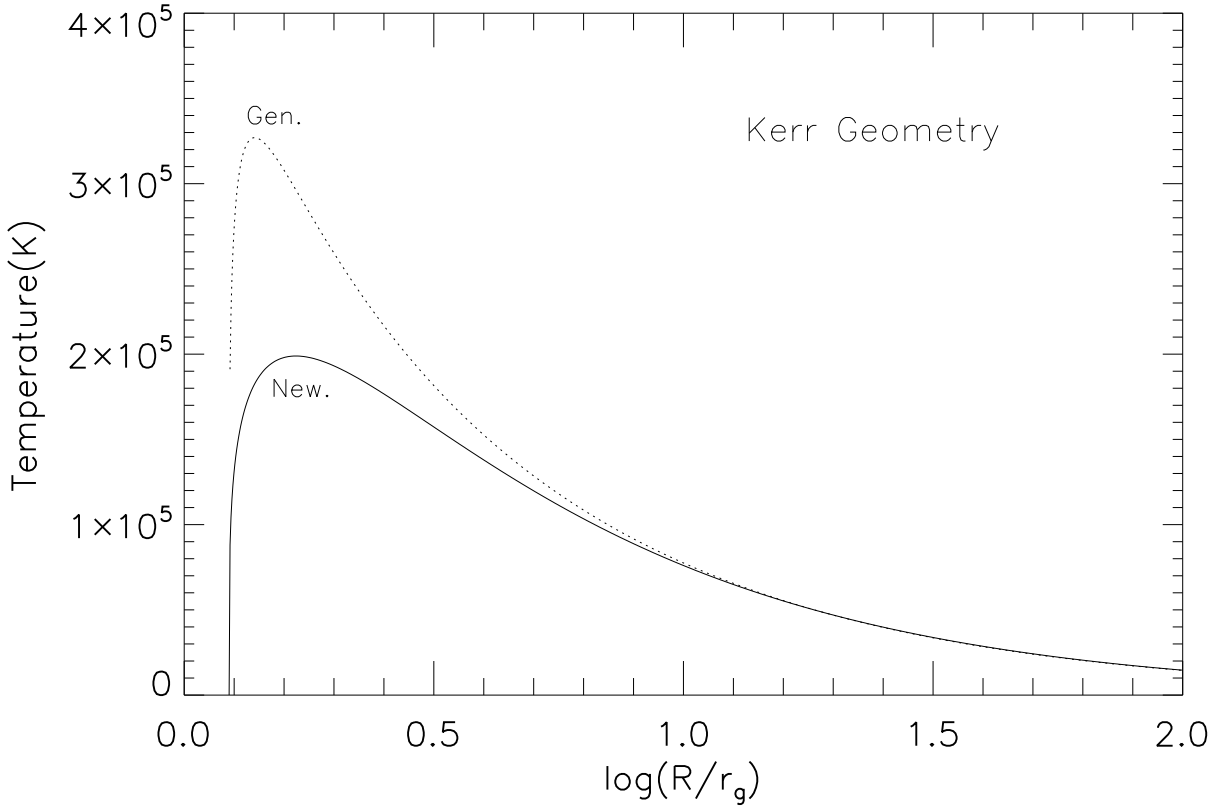

Figure 19 As in Figure 18 but for the disk temperature as a function of the radius in a Kerr geometry.

side of the disk along the observer's line of sight.[2] However, the double-peaked phenomenon is usually not observed in quasar spectra. Only a small fraction of AGN (3%-5%) with low-ionization Hydrogen Balmer BELs shows clear double-peaked profiles (Strateva et al. 2003), while the high-ionization emission lines (e.g., CIV and Lyα) are generally single-peaked. To explain the usually often-observed single-peaked emission lines with a rotating AD, two models to produce single-peaked BELs have been proposed; e.g., the two-component BELR model (Bon et al. 2009b) and the disk-wind model (Murray & Chiang 1997). In these models, in addition to the disk emission component, the former introduces isotropic velocity clouds above and below the AD to enhance the flux in the line cores, while the latter proposes a wind launched from the AD that increases the chance of line photons escaping from the near-

[2]The BELR geometry is defined in the Appendix.

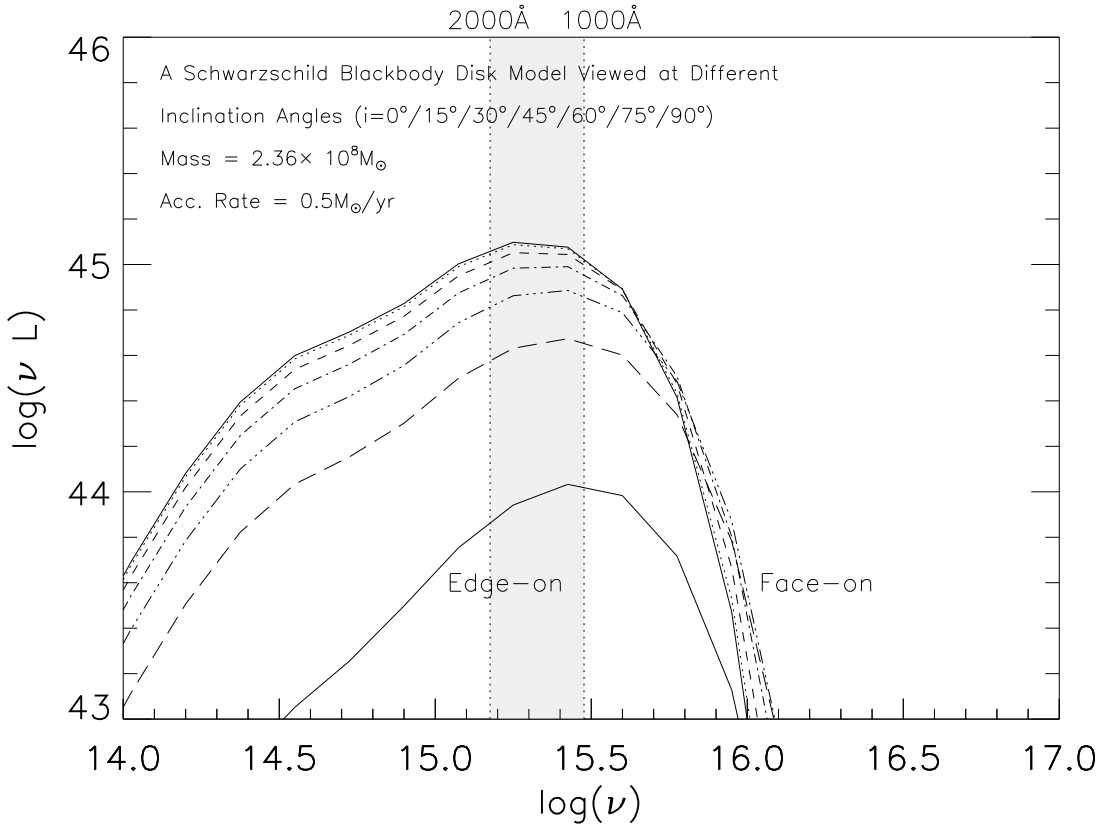

Figure 20 The observed spectrum of a single Schwarzschild blackbody disk with typical black hole mass and mass accretion rate, but viewed from seven different inclination angles. At low frequencies, the disk luminosity fades classically as $\cos i$. In contrast, at frequencies above 10^{16} Hz, the spectrum appears harder as the disk axis is titled away from the line of sight.

and far-side of the disk along the observer's line of sight, hence enhancing the contribution to the line cores rather than the wings in the BEL profiles.

Although both models are able to reproduce the observed single-peaked BEL profiles, nature probably tends to support continuous flows such as disk-wind models rather than discrete random cloud models (Arav et al. 1997, 1998). First, early spectroscopic observations of AGN showed that the BELs rise from the dense region with a small volume filling factor where the emission is anisotropic. Second, the observed BEL profiles are in general smooth. Third, reverberation mapping of Type 1 Seyfert galaxies showed that the BEL gas motions are predominantly Keplerian (Peterson 1998). Furthermore, from the spectral analysis of

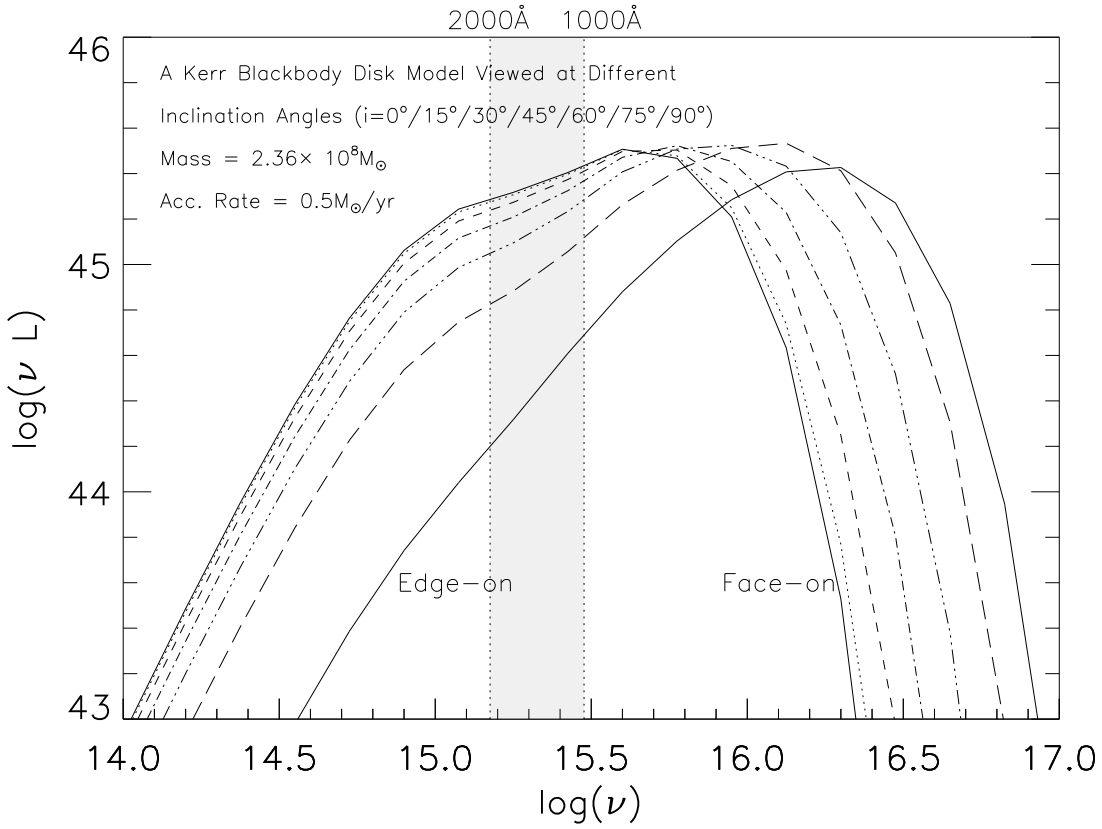

Figure 21 The observed spectrum of a single Kerr blackbody disk with typical black hole mass and mass accretion rate, but viewed from seven different inclination angles. At low frequencies, the disk luminosity fades classically as $\cos i$. In contrast, at frequencies above 10^{16} Hz, the spectrum appears harder as the disk axis is titled away from the line of sight.

their two-component BELR model, Bon et al. (2009b) concluded that the line flux emitted from random rotating clouds is dominant (at least larger than 50%) relative to the total line flux needed to reproduce the observed line profiles, which conflicts with the argument of an anisotropic region of line emissivity. On the other hand, the disk-wind model is favored because BELs form naturally at the base of the continuous disk wind, providing a single origin for the BELRs without additional emission sources. Therefore, I adopt the disk-wind model as the test model to compute BEL profiles.

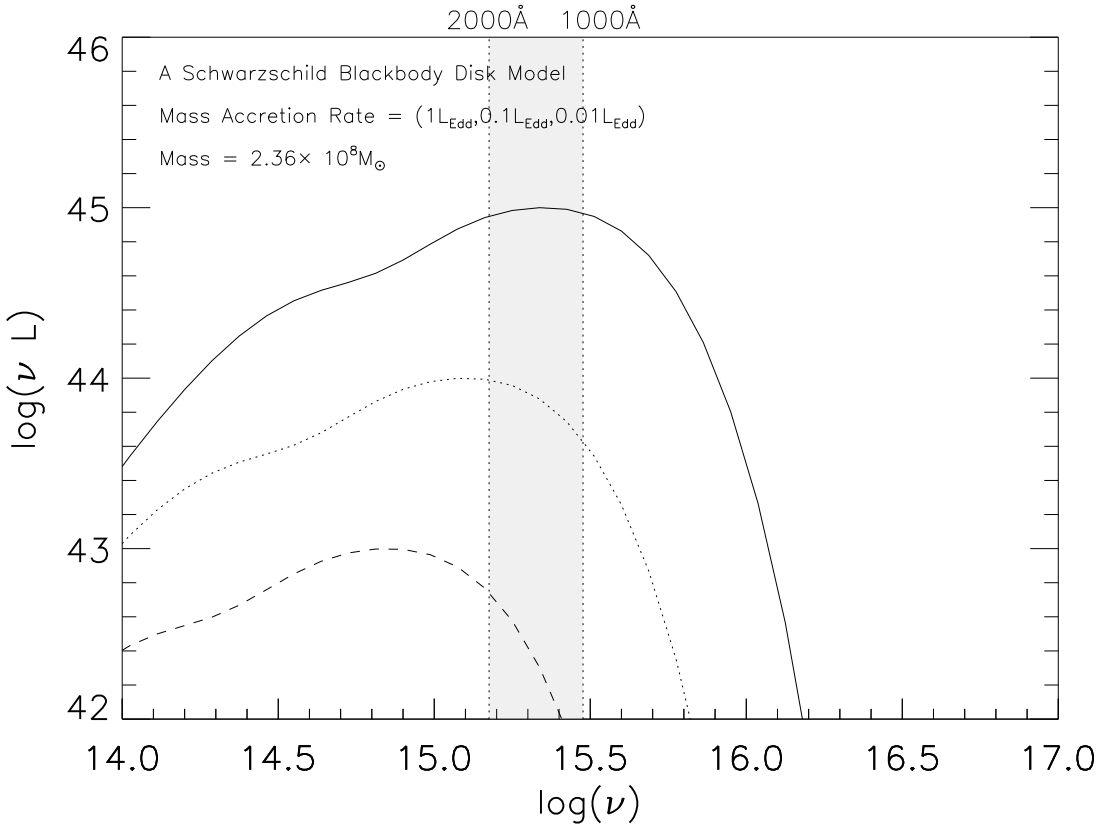

Figure 22 The observed spectrum of a single Schwarzschild blackbody disk with a typical black hole mass, but different mass accretion rates in terms of the Eddington limit.

5.2.2 Relativistic Disk-Wind Formalism

In this section I will briefly describe the formalism I use to reproduce the normally-observed single-peaked BELs, and to explore the origin of blueshifted peaks and asymmetries found commonly in high-ionization BELs, particular in the Lyα and CIV BELs. I primarily adopt the Flohic et al. (2012) prescription that combines the analytic radiative transfer effect in the Murray & Chiang (1997) disk-wind model and the Chen et al. (1989) calculation of relativistic Keplerian AD emission to compute the single-peaked emission line profiles.[3] In

[3]Flohic et al. (2012) state that their model does not apply to high-ionization lines (e.g., CIV or other UV resonance lines) because these lines are produced in a highly ionized layer that has a much larger vertical extent than the Balmer line emitting zone and also has a substantial vertical velocity and a non-Keplerian azimuthal velocity. However, current reverberation mapping results confirm that the location of the high-ionization BELRs are farther out than the distance proposed for Balmer lines. With the unclear wind velocity

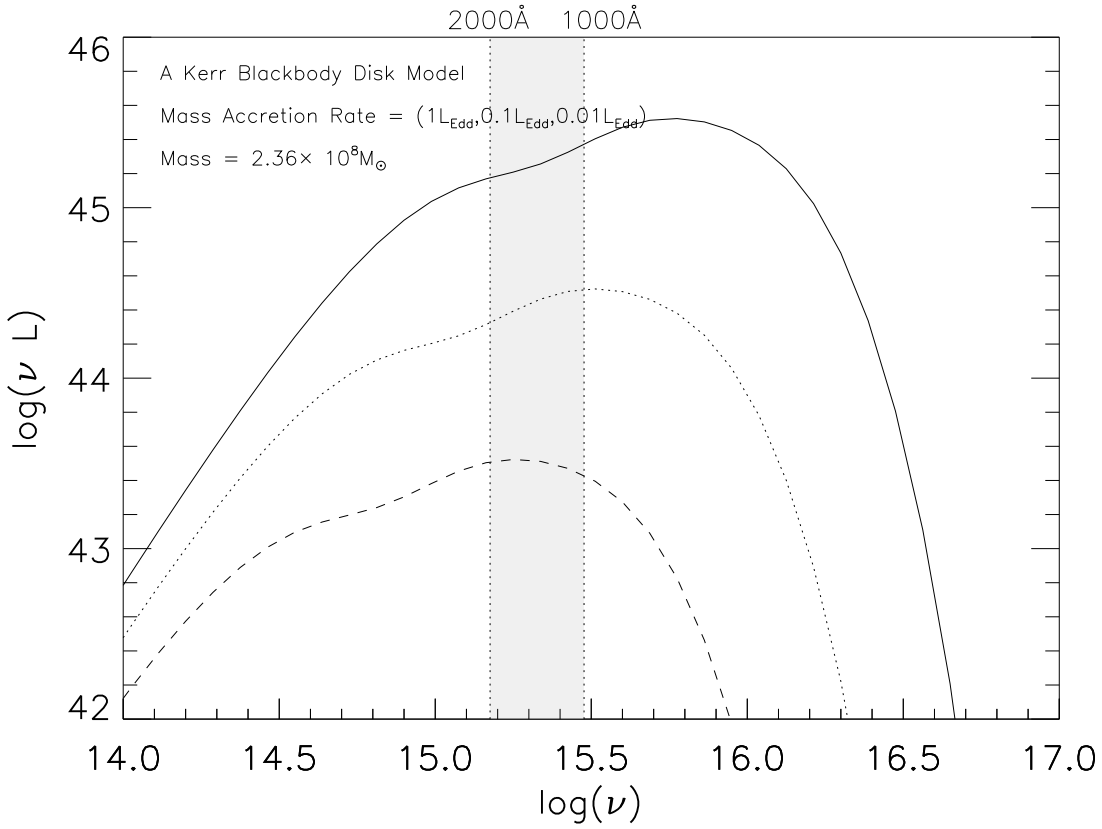

Figure 23 The observed spectrum of a single Kerr blackbody disk with a typical black hole mass, but different mass accretion rates in terms of the Eddington limit.

order to achieve the often-observed blueshifts and asymmetries seen in the BELs, I implement several wind situations (i.e., wind velocity fields) to test the feasibility of the disk-wind model. Also, a number of the free parameters introduced in the relativistic disk-wind model will be examined extensively and discussed in Section 5.2.3.

Given the fact that reverberation mapping distances of BELRs in luminous AGN (i.e., in the vicinity of a SMBH) are typically of order thousands of times the gravitational radius, it is not necessary to take into account relativistic effects. Chen et al. (1989) and Chen & Halpern (1989) provided the calculation for thin Keplerian disk emission including relativistic effects. In this case, the expression for emission per unit frequency ν interval for a BEL is

structure and larger distance of CIV BELR, I argue that their formalism is still valid for high-ionization BELs by adopting appropriate constraints.

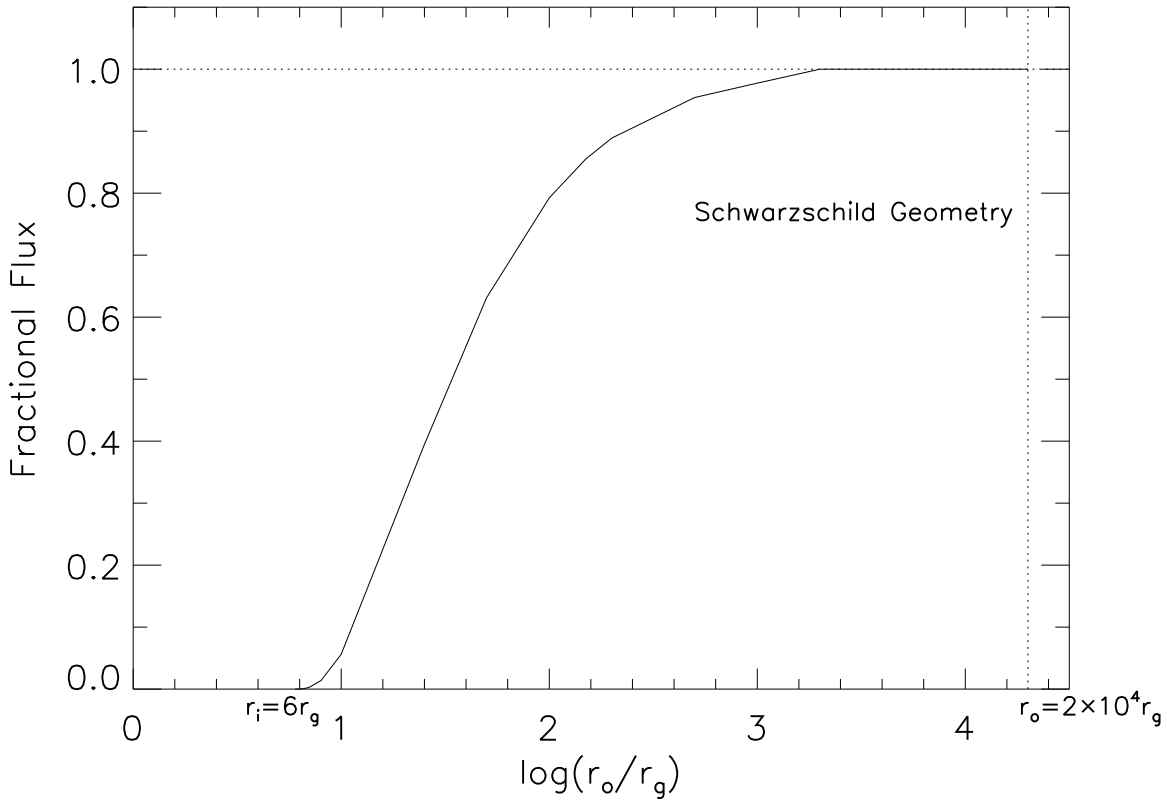

Figure 24 The fractional flux as a function of the accretion disk size r_o in a Schwarzschild geometry.

(see Appendix for details of the calculation):

$$f_\nu = \frac{r_g^2}{d^2} \int_0^{2\pi} \int_{\xi_1}^{\xi_2} I_{\nu_e}(\xi, \phi', \nu) D^3(\xi, \phi') \Psi(\xi, \phi') \, \xi \, d\xi \, d\phi' \tag{5.4}$$

where ϕ' is the azimuthal angle in the disk frame to be integrated over, and ξ is the dimensionless disk radius from the central back hole in units of the gravitational radius r_g, integrated between characteristic inner and outer radii, ξ_1 and ξ_2, of the BELR, respectively. The first term, $I_{\nu_e}(\xi, \phi', \nu)$, is the specific intensity from the BELR shown in Equation 5.7. The second term, $D(\xi, \phi') = \nu/\nu_e$, is the relativistic Doppler factor, indicating the strength of the emitted frequency ν_e relative to the observed frequency ν under the influence of the

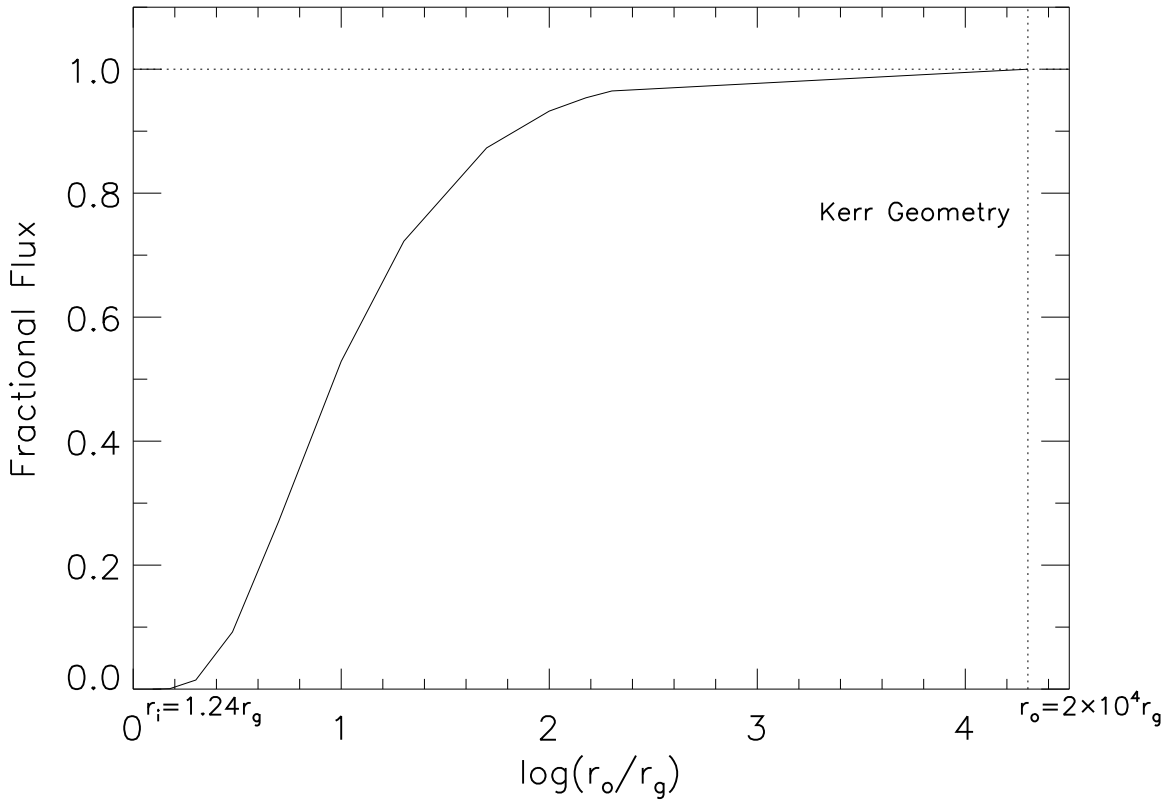

Figure 25 The fractional flux as a function of the accretion disk size r_o in a Kerr geometry.

gravitational potential of a SMBH. In the weak-field approximation,

$$D(\xi, \phi') = \left(1 - \frac{3}{\xi}\right)^{1/2} \left(1 + \xi^{-1/2} \sin i \sin \phi'\right)^{-1} \tag{5.5}$$

where i is the disk inclination to the observer's line of sight measured from the rotation axis of the disk. The third term, $\Psi(\xi, \phi')$,[4] is the correction of the gravitational redshift and light bending effects derived as

$$\Psi(\xi, \phi') = \left(1 + \frac{1}{\xi} \frac{1 - \sin i \cos \phi'}{1 + \sin i \cos \phi'}\right). \tag{5.6}$$

To present the intensity of the BELR, the Murray & Chiang (1997) disk-wind model is adopted, which includes radiative transfer effects through winds. In their model, the bulk of

[4]The notation $\Psi(\xi, \phi')$ was introduced by Flohic et al. (2012). This corresponds to the function $g(D)$ used by Chen & Halpern (1989) where their function $g(D)$ is related to $\Psi(\xi, \phi')$ via $g(D) = 1/2[\Psi(\xi, \phi') + \Psi(\xi, \pi - \phi')]$ (Eracleous et al. 1995).

a BEL is expected to originate at the base of the wind where the density is highest, so these lines can be formed by collisional excitation or recombination.

These winds are characterized by some important general features. First, they have a small opening angle relative to the equatorial plane of the AD. Second, the motion of the BELR is predominantly Keplerian, even though the wind is also outflowing with its launch velocity less than the sound speed. Third, the velocity gradient along the wind is much larger than the radial gradient of the azimuthal velocity (i.e., the Keplerian rotation velocity). The last property is particularly important in the context of predicting the BEL profiles, since it affects the radiative transfer of the line photons though the wind. More specifically, the apparent optical depth is suppressed in regions of the wind that have a large projected velocity gradient along the observer's line of sight.[5] As a result, the emissivity of the disk is not axisymmetric, with regions at low projected Keplerian velocity appearing brighter. Thus, in this situation, the profiles of the emerging BELs appear single-peaked because their cores are enhanced and their wings are suppressed.

The specific intensity of a BEL including this radiative transfer effect, is defined as

$$I_{\nu_e}(\xi, \phi', \nu) \propto \frac{1 - e^{-\tau}}{\tau} \epsilon(\xi) \exp\left[-\frac{(\nu_e - \nu_0)^2}{2\sigma^2}\right]. \tag{5.7}$$

The first term, $(1 - e^{-\tau})/\tau$, represents the probability for a photon to escape the wind in the direction of the observer, which depends on the optical depth along the observer's line of sight, τ_{ν_e} (Hamann et al. 1993). The second term, $\epsilon(\xi)$, is the emissivity of the disk, which is taken to be the simplest power law with index q (i.e., $\epsilon(\xi) = \epsilon_0 \xi^{-q}$). The last exponential function is the local broadening of the line, which is assumed to be a Gaussian function, characterized by the line broadening parameter σ, where the emitted frequency of the photon is ν_e and the rest frequency is ν_0. Using the Sobolev approximation for flows whose component to the line of sight is non-monotonic, the optical depth is defined as (Rybicki & Hummer 1978)

$$\tau = \frac{\kappa \rho \sigma}{|\hat{n} \cdot \Lambda \cdot \hat{n}|} \tag{5.8}$$

[5]In the Sobolev approximation, the optical depth is proportional to the inverse of the velocity gradient along the observer's line of sight $\hat{n}$ (i.e., $\tau \propto 1/|d\vec{v}/dn \cdot \hat{n}|$ for the one-dimensional case). The larger the velocity gradient the smaller the optical depth, so that a photon has a higher chance to escape along the observer's line of sight.

where κ is the line absorption coefficient, ρ is the density of the emitting material, σ is its thermal velocity, $\hat{n}$ is the line of sight vector and Λ is the symmetric strain tensor. Given the assumption that the density ρ behaves like a power law of the normalized distance ξ with the power index η, the optical depth can then be rewritten as

$$\tau = \xi^{\eta} \frac{\tau_0}{|\hat{n} \cdot \Lambda \cdot \hat{n}|} \tag{5.9}$$

where τ_0 is the characteristic optical depth.

Given knowledge of the disk wind's velocity structure, the optical depth τ can be evaluated, yielding the line-emission intensity. It is well known that the disk wind is accelerated by some radiative pressure from the inner region of the disk. However, the true acceleration mechanism is still not well understood. Murray et al. (1995) formulated the analytical velocity structure of the disk wind to calculate $|\hat{n} \cdot \Lambda \cdot \hat{n}|$ defined as a Q-value. They proposed that the disk wind is in helical motion; near the surface of the disk, the motion is primarily rotational, with $v_{\phi'} \sim 10,000\,\mathrm{km\,s^{-1}}$. For a typical quasar of mass $\sim 10^8 M_\odot$, the wind emerges at $r \sim 10^{16}\,\mathrm{cm}$ from the disk, then accelerates rapidly and radially. So the radial velocity is given by

$$v_r = v_\infty \left(1 - \frac{\xi_f}{\xi}\right)^{\beta} \tag{5.10}$$

where ξ_f is the launching radius of the streamline of the wind, v_∞ is the terminal velocity of the wind and β is the power of the velocity law. These are the physical properties to describe the nature of the disk wind, which can be solved analytically or numerically. Typically, for a mass of $10^8 M_\odot$ for the central black hole, $\beta = 1$ and $v_\infty \sim 30,000\,\mathrm{km\,s^{-1}}$ are adopted.

As a result, the double-dot product of the strain tensor becomes

$$\begin{aligned} Q \;=\; & \frac{v_\infty}{\xi} \left[\sin^2 i \left(\cos^2 \phi' + \frac{3}{2} \frac{v_{\phi'}}{v_\infty} \sin\phi' \cos\phi' \right) \right. \\ & \left. + \cos i \left(\frac{\sin i \cos\phi'}{\sin\lambda} + \cos i + \frac{v_{\phi'}}{v_\infty} \frac{\sin i \sin\phi'}{2\sin\lambda} \right) \right]. \end{aligned} \tag{5.11}$$

where λ is the opening angle of the wind from the surface of the disk, i is the inclination angle of the disk to the observer measured from the rotating disk axis, and ϕ' is the azimuthal angle in the disk frame. The azimuthal velocity of the disk, $v_{\phi'}$, is taken to be Keplerian.

Throughout this chapter, we use the Lyα BEL as our working example. All the line profiles in this chapter are normalized so that $\int F_\nu \, d\nu = 1$, unless noted otherwise.

5.2.3 Parameters for the Disk-Wind Model

As noted in Murray et al. (1995), the disk-wind model can fit the line profiles of BELs, but it is too poorly defined to constrain the physical parameters, i.e., the disk-wind model includes many parameters (the size of the emitting region, the disk emissivity, the disk inclination, etc.). Therefore, in order to do numerical tests, one needs to introduce some constraints and approximations. The double dot product of the strain tensor Q in Equation 5.11 is used in the first attempt.

1. Figure 26 illustrates the effect of optical depth in Equation 5.9 on disk-wind line profiles. The parameters of the profiles are as follow: $\xi_1 = 1320 r_g$, $\xi_2 = 10\xi_1$, $i = 45°$, $\lambda = 15°$, $\eta = -2$ and $q = 3$. The solid line ($\tau_0 = 10^6$) is the profile for an optically thick line $\tau \sim 10^4$ at the inner radius, the dashed-dot-dot line ($\tau_0 = 10^3$) has $\tau \sim 10$, while the dotted line ($\tau_0 = 0.01$) is for an optically thin line with $\tau \sim 10^{-4}$. Optically thin lines are double-peaked, since the escape probability is nearly independent of ϕ'. Increasing τ_0 from 10^4 does not alter the appearance of the line profile significantly, so the profiles at $\tau_0 \geq 10^6$ are nearly identical. It is concluded that as the optical depth of the disk-wind increases, the line profiles appear to be single-peaked.
2. The power index η in Equation 5.9 describes how the density of the BEL material drops across the distance of the disk. In the photoionization model, η has to be -2 in order to preserve the ionization parameter (Hamann et al. 1993). Moreover, for a disk-wind with the fixed mass-loss rate, the density has the from $\rho \propto 1/(r^2 v)$, thus η is in the range of -2 to -1.5. Figure 27 shows the simulated line profiles for different values of η. It clearly demonstrates that this parameter is not sensitive for the line shape but for the peak of the line. The single-peaked line profiles with very sharp peaks have $\eta = -2$, which is the value I adopt throughout this work.
3. The emissivity function ϵ in Equation 5.7 is taken to be any analytical function from the simplest power law of radius given by $\epsilon = \epsilon_0 r^{-q}$, where q is the emissivity index. Conventionally, an isotropic central source illuminating a thin disk gives $q = 3$ (Mardaljevic et al. 1988). It means the illuminating flux falls as r^{-2} from the central source, and the flux falling per radius increment on the disk decreases as r^{-1} due to geometric effects.

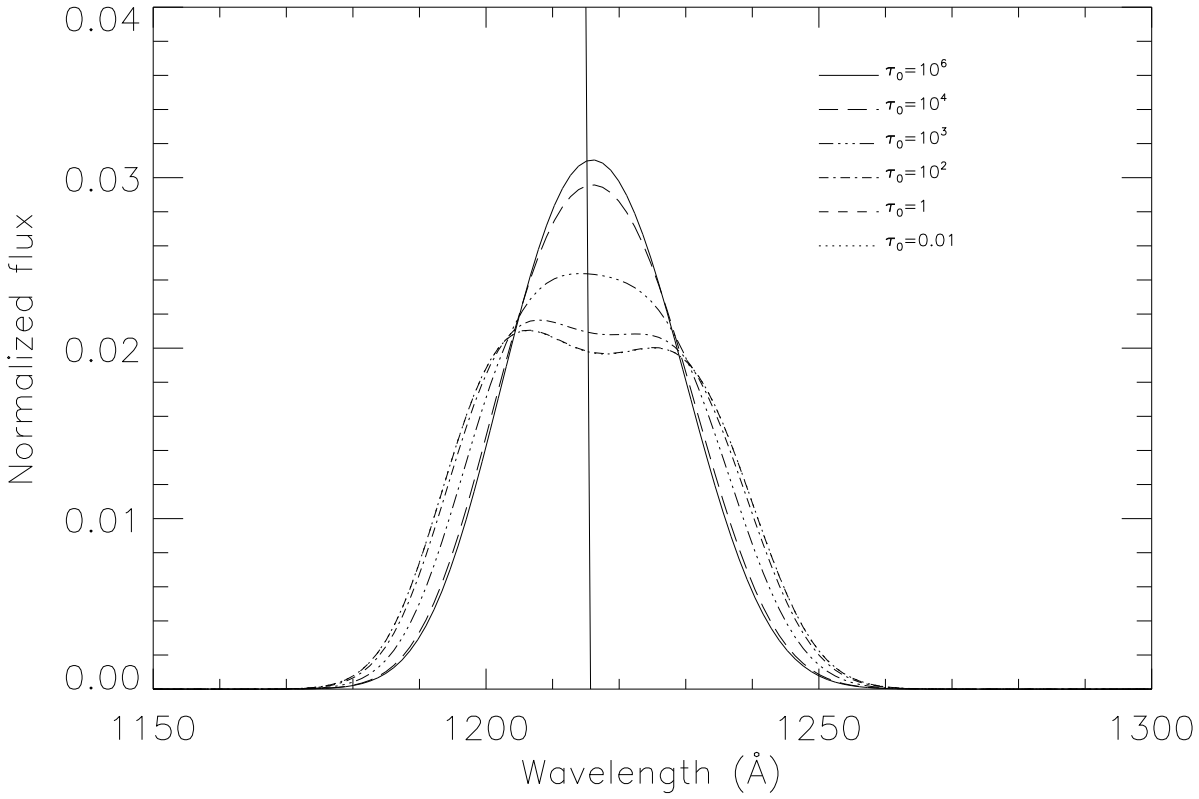

Figure 26 Profiles of the Lyα BEL for $\tau_0 = 0.01, 1, 10, 10^2, 10^3, 10^4$. The other parameters adapted for the calculation are: $\xi_1 = 1320 r_g$, $\xi_2 = 10\xi_1$, $i = 45°$, $\lambda = 15°$, $\eta = -2$ and $q = 3$. Note that the profiles at $\tau_0 = 1$ and $\tau_0 = 0.01$ are identical.

As the emissivity q can be found from fitting the observed line profile, $q \sim 3$ is adopted as a reasonable approximation at least for Hα (Eracleous & Halpern 2003). Also, Cao & Wang (2006) verified that $q \sim 2 - 3$ is required by models fitted to double-peaked line profiles. Furthermore, I have simulated the influence of the emissivity to the disk line profile shown in Figure 28 and found that it only slightly affects the normalized disk line profiles. Throughout this work, the assumption of $q = 3$ is adopted.

4. Some other parameters are the inner and outer radii, ξ_1 and ξ_2, of the emission region. The time delays of BEL variations in response to continuum changes in high luminosity quasars limits the inner radius of the BELR to $\xi_1 > 1000 r_g$. Consequently, the model given by Chen et al. (1989) can be properly used and it is not necessary to include a

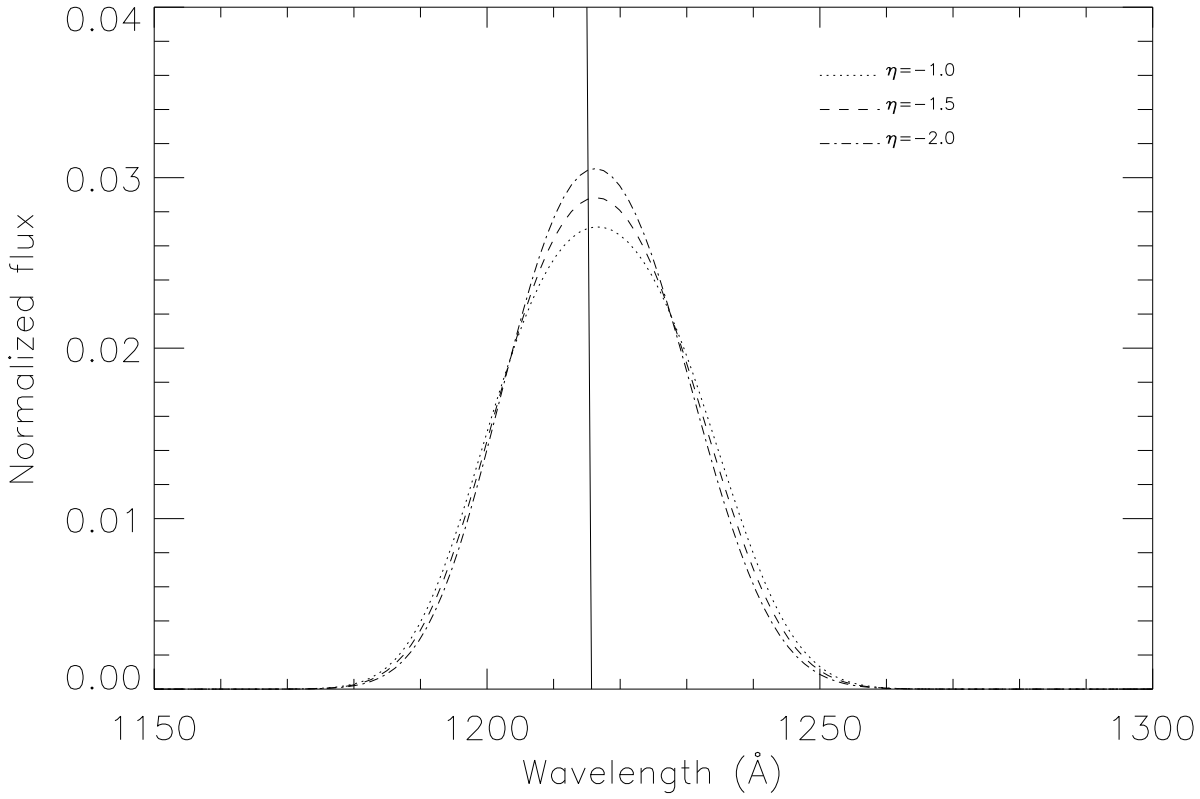

Figure 27 Profiles of the Lyα BEL for $\eta = -1, -1.5, -2$. The other parameters adapted for the calculation are: $\xi_1 = 1320 r_g$, $\xi_2 = 10\xi_1$, $i = 45°$, $\lambda = 15°$, $\tau_0 = 10^3$ and $q = 3$.

full relativistic calculation (Jovanović & Popović 2008). Unfortunately, the reverberation mapping technique cannot estimate the outer radius of the emission region. However, the results show that the low-ionization BELRs are farther out than the high-ionization BELRs. The low-ionization BELRs are at several thousands r_g, which corresponds to a distance where the thin disk becomes gravitationally unstable. This happens when the self-gravity of the disk begins to dominate over the vertical gravity of the black hole (Shlosman & Begelman 1987; Goodman 2003). Thus, to limit the outer radius of high-ionization BELRs, I assume it to be ten times its inner radius (i.e., $\xi_2 = 10\xi_1$). In any case, shown in Figure 29, the amount of BELR disk emission is not very sensitive to the outer radius of the disk.

5. The most crucial parameter is the inclination angle i measured from the rotation axis of

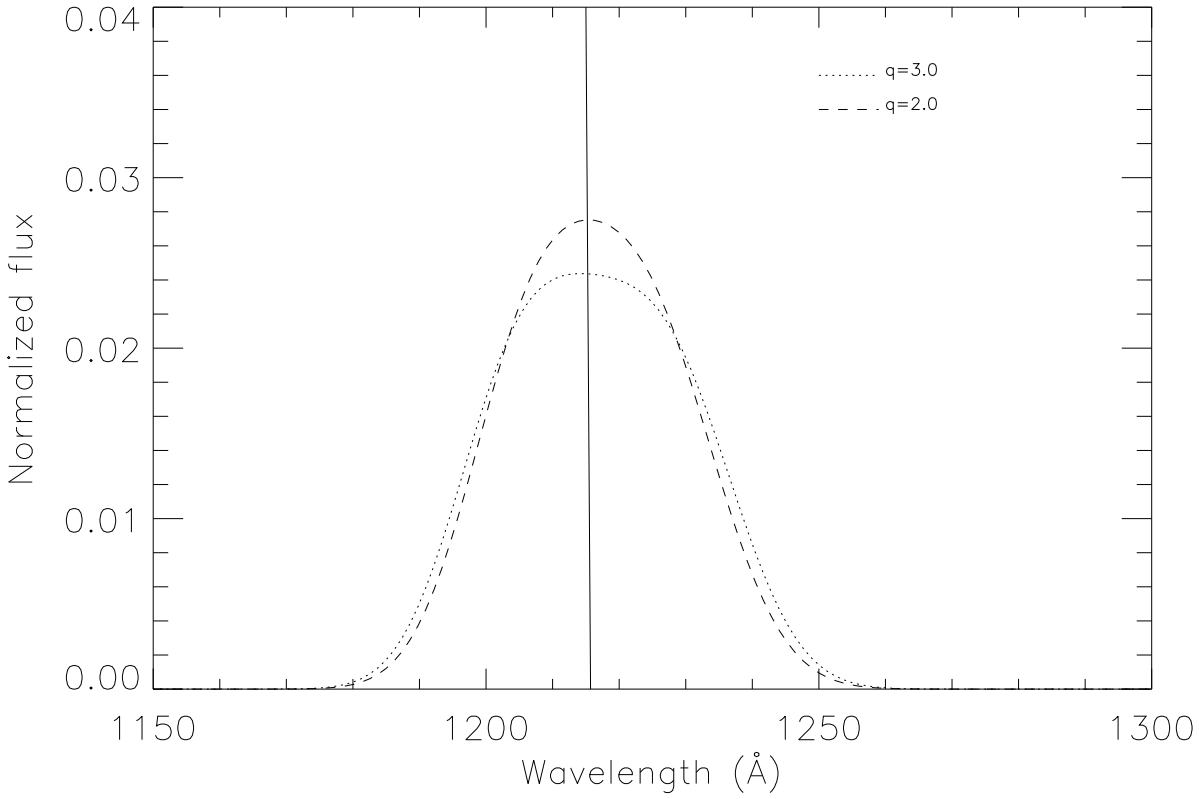

Figure 28 Profiles of the Lyα BEL for $q = 2, 3$. The other parameters adapted for the calculation are: $\xi_1 = 1320 r_g$, $\xi_2 = 10\xi_1$, $i = 45°$, $\lambda = 15°$, $\tau_0 = 10^3$ and $\eta = -2$.

the disk to the observer's line of sight. The disk inclination affects the emission obtained from the disk and also determines the strength of all relativistic effects on the emission lines. For example, in the case of viewing at low inclination (i.e., a face-on disk), the line profiles show more flux towards the red due to the gravitational redshift. While viewing at high inclination (i.e., an edge-on disk), the line profiles show more flux in the far wings due to the Doppler boosting. Given the evidence for a dusty torus along the equatorial plane of the disk, the inner disk region would be obscured from direct observation when viewed at high inclination. The most recent report suggests that the obscuring torus is at a radius of a few hundred parsec with an opening angle $\sim 67°$ measured from the rotation axis of the disk (Polletta et al. 2007). This places a limit on the inclination angle to the observer. As there is no direct observation to measure the disk inclination,

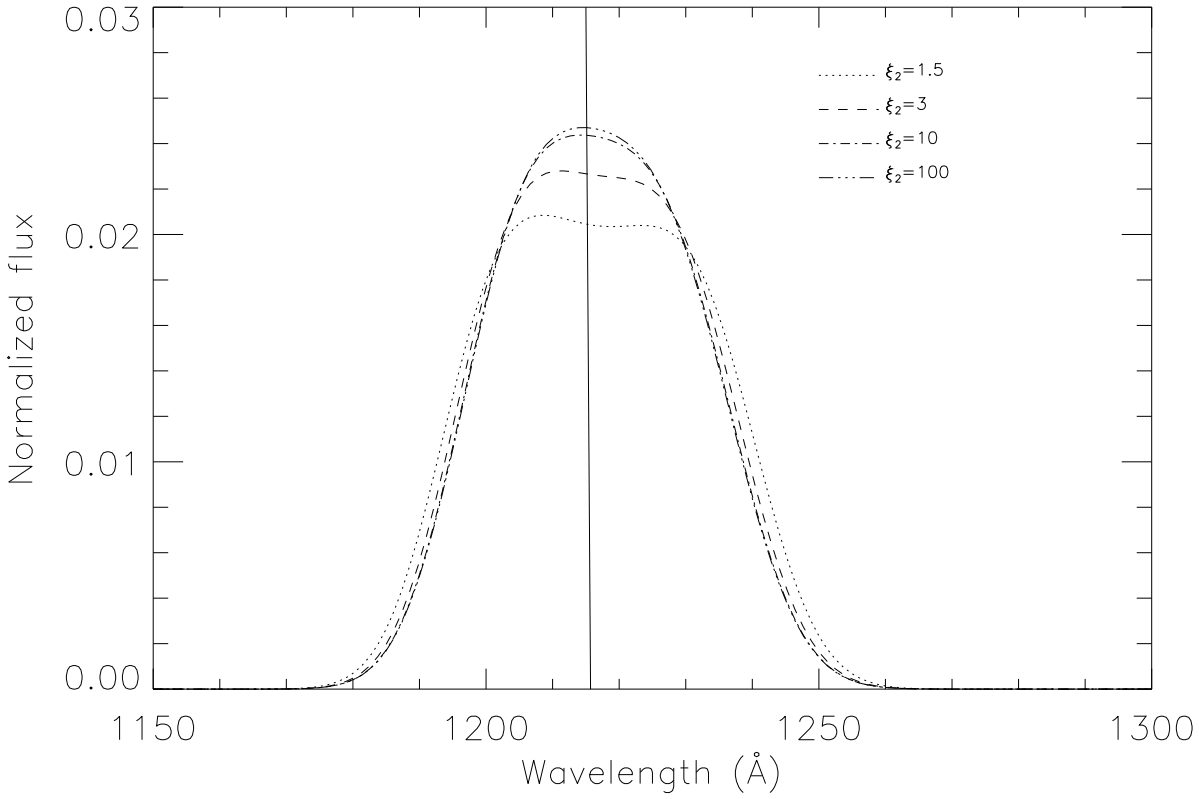

Figure 29 Profiles of the Lyα BEL for different values of outer radius $\xi_2 = 1.5, 3, 10, 100\xi_1$ where $\xi_1 = 1320 r_g$. The other parameters adapted for the calculation are: $i = 45°$, $\lambda = 15°$, $\tau_0 = 10^3$, $\eta = -2$ and $q = 3$.

for the first attempt I choose the average inclination to be $i = 45°$.

6. Particularly in the disk-wind model, one free parameter λ is the outflow angle of the wind launched from the AD measured from the surface of the disk. It determines the escape probability of line photons along the observer's line of sight, but cannot be constrained observationally. As such, Elvis (2000) suggests that luminosity-dependent effects are directly related to changes in the wind geometry. A higher luminosity quasar would weaken the wind and it would have a smaller wind opening angle. With a combination of the outflow angle and inclination angle, a blueshifted and asymmetric emission line can be achieved (Hall & Chajet 2010). Figure 30 and Figure 31 demonstrate a series of emission line profiles with a number of combinations of the disk inclination angle i

and wind launch angle λ from the surface of the AD. In our study, the combination of the two angles can slightly modify the physical shape (i.e., FWHM and peak) of the line profiles. However, we find that varying the two angles does not provide enough flexibility to produce line profiles with very blueshifted peaks and high asymmetries.

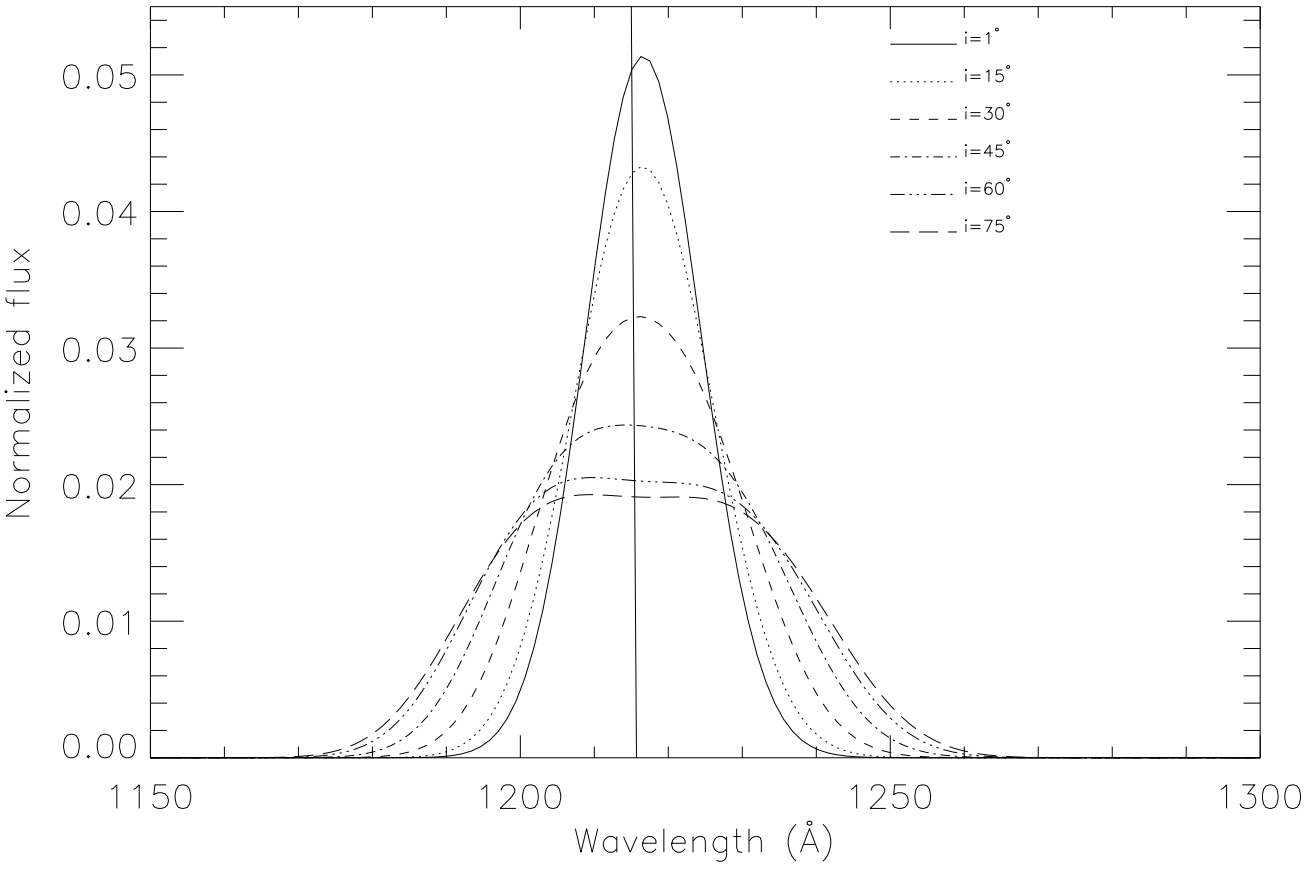

Figure 30 Profiles of the Lyα BEL for different inclinations i between the AD rotation axis and the observer's line of sight, with a disk-wind opening angle at $\lambda = 15°$ relative to the AD surface. The other parameters adapted for the calculation are: $\xi_1 = 1320 r_g$, $\xi_2 = 10\xi_1$, $i = 45°$, $\lambda = 15°$, $\tau_0 = 10^3$, $\eta = -2$ and $q = 3$.

5.2.4 Peak Offsets, Normalized Line Widths, and Asymmetry Parameters of BELs

As mentioned in Section 1.2.1, in additional to being single-peaked, high-ionization BELs (e.g., CIV) are often blueshifted with respect to low-ionization BELs (e.g., MgII). Also,

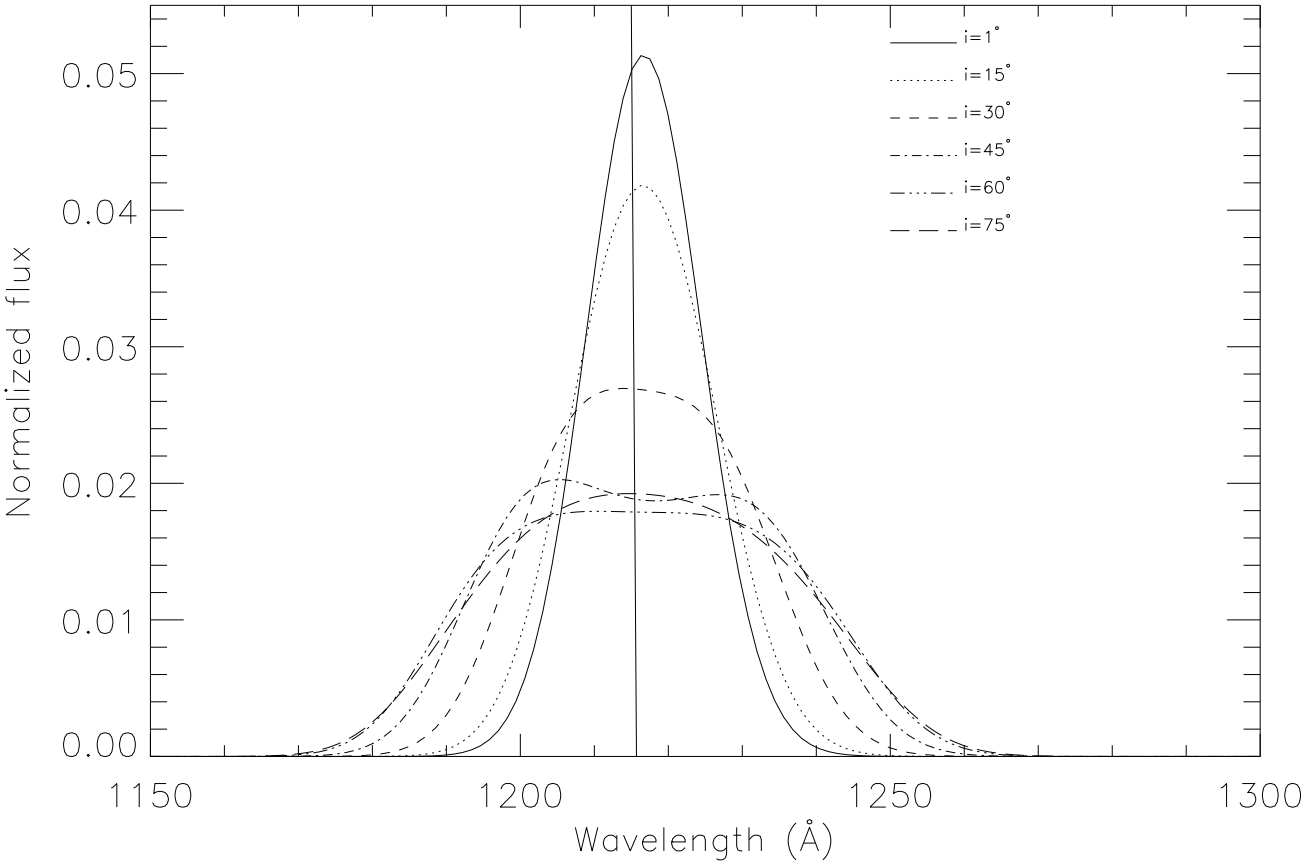

Figure 31 Same as Figure 30, but for $\lambda = 85°$.

these high-ionization lines often show significant asymmetry with excess flux in the blue wing. This raises the question of whether the blueward asymmetry could be associated with the accretion disk. The disk-wind model with relativistic effects is attractive because it can produce single-peaked BELs and, in the parameter study of the simulated line profiles in Section 5.2.3, it can give rise to BEL asymmetries. However, the asymmetries are mostly redward (i.e., excess flux in the red wing), and blueshifted peaks are rarely produced. We will investigate if blue offsets and asymmetries can be produced in high-ionization BELs. The investigation of relativistic effects in the BELRs and the double dot strain tensor Q will be discussed here.

5.2.4.1 Relativistic Effects In Figure 32, I show a grid of Lyα BEL profiles computed using the expression for Q in Equation A.36 with the model parameters mentioned in Sec-

tion 5.2.3. They are $\eta = -2$, $q = 3$, $\tau_0 = 10^3$. The inclination angles are investigated from 0° to 75° in steps of 15°. To illustrate how relativistic effects influence the line profile, the line emitting material should be at regions close to the central back hole. In the test case, its inner radius is assumed to be $\xi_1 = 132 r_g$ and the outer radius is constrained to be ten times the inner radius (i.e., $\xi_2 = 10\xi_1$). Each panel shows the line profile without relativistic effects (dotted line) and with relativistic effects (solid line). Relativistic effects shift the line profile towards the red and make it slightly asymmetric, with more flux in the red wing. The effects of relativity appear more pronounced at lower inclination. To simulate the line profile of the Lyα BEL, I adopt the distance of the Lyα BELR inferred from the recent reverberation mapping results (see Chapter 4 for details). Typically, for high-ionization BELs in luminous AGN, their distances are $\sim$ thousands of times the gravitational radius, hence an inner radius of $\xi_1 = 1320 r_g$, and an outer radius of $\xi_2 = 10\xi_1$ are adopted with a black hole mass of $10^8 M_\odot$. Using this choice of parameters, Figure 33 shows another grid of Lyα BEL profiles demonstrating the effects of relativity with increasing inclination. With this choice of parameters, the line profiles have less flux in the wings and a smaller FWHM. Comparing the two figures, the lines in the former figure have a very large FWHM and the inclusion of relativistic effects significantly redshifts the line profile. For the case of increasing the distance of the emitting material shown in Figure 33, the impact of relativistic effects on the line profile decreases. Therefore, if we wish to maintain consistency with the reverberation mapping results, we conclude that the relativistic effects do not strongly influence the shapes of the BEL profiles.

In conclusion, disk-wind models with relativistic effects alone cannot explain the blueward profile asymmetries sometimes observed in the high-ionization BELs of quasars nor can they explain the $\sim 10^2 - 10^3\,\mathrm{km\,s^{-1}}$ blueshifted peak, so an additional mechanism acting on the line emission is required. Corbin (1997) suggested that electron scattering from x-ray−heated winds may be one possibility. Moreover, Gaskell & Goosmann (2008) show that the blueshifting can be produced from electron scattering from an inflowing medium. Alternatively, in addition to the disk-wind component, an additional emission component causing blueshifted or blue asymmetric profiles may be present (Marziani et al. 2003).

5.2.4.2 Q-value The Q-value is the double dot product of the strain tensor $|\hat{n} \cdot \Lambda \cdot \hat{n}|$, which is angle dependent. In wind models, different wind dynamics will modify the value of Q, which leads to a change in the escape probability of photons from different parts of the AD, resulting in different profile shapes. In Section 5.2.3, I adopted the Murray et al. (1995) analytical velocity structure for the first estimate:

$$v_r = v_\infty \left(1 - \frac{r_f}{r}\right) \tag{5.12}$$

$$v_{\theta'} = -v_r \sin\lambda(r) \tag{5.13}$$

$$v_{\phi'} = \left(\frac{GM}{r_f}\right)^{1/2} \frac{r}{r_f}. \tag{5.14}$$

Their model suggested that the geometry of the disk wind is equatorial and the path of the wind is helical. In the disk atmosphere where the wind lifts off from the disk, it primarily shares the Keplerian velocity of the disk with little radial velocity (i.e., $v_r \sim 0$). Subsequently it is accelerated radially by the radiation from the central region of the disk and eventually reaches the terminal velocity. The wind opening angle λ is constrained to be small and the wind is driven along the surface of the disk. Because the real geometry of the disk wind is still unknown, the constraint of small λ can be relaxed in order to test whether or not an asymmetric line profile with a peak offset is achievable. To allow the wind to launch at a larger λ, the velocity field of the polar component is modified to $v_\theta = -v_r \tan\lambda(r)$, and its Q-value is shown in Equation A.36. Figures 34–36 demonstrate the fact that no matter what the combination of the disk inclination angle i and the opening angle λ is adopted, it lacks the flexibility to produce the often-seen features of the line profiles.

Hall & Chajet (2010) suggested that in order to have blueshifts which are comparable to those that are sometimes observed in CIV BEL profiles, the wind launch velocity at each radius equals the Keplerian velocity at that radius and the streamlines are straight with constant poloidal angle λ. The radial velocity becomes

$$v_r = v_\infty \left(1 - \frac{r_f}{r}\right)^\beta + v_{\phi'} \cos\lambda. \tag{5.15}$$

Its Q-value is shown in Equation A.38. Figures 37–39 demonstrate that the line profiles do not have the ability to produce the often-seen features with different combinations of the

disk inclination angle i and the opening angle λ. It is concluded that the asymmetry of BELs weakly depends on Q-value, which is inconsistent with the results of Hall & Chajet (2010). However, Hall & Chajet (2010) may have implemented a different velocity law than the one given in Equation 5.15.

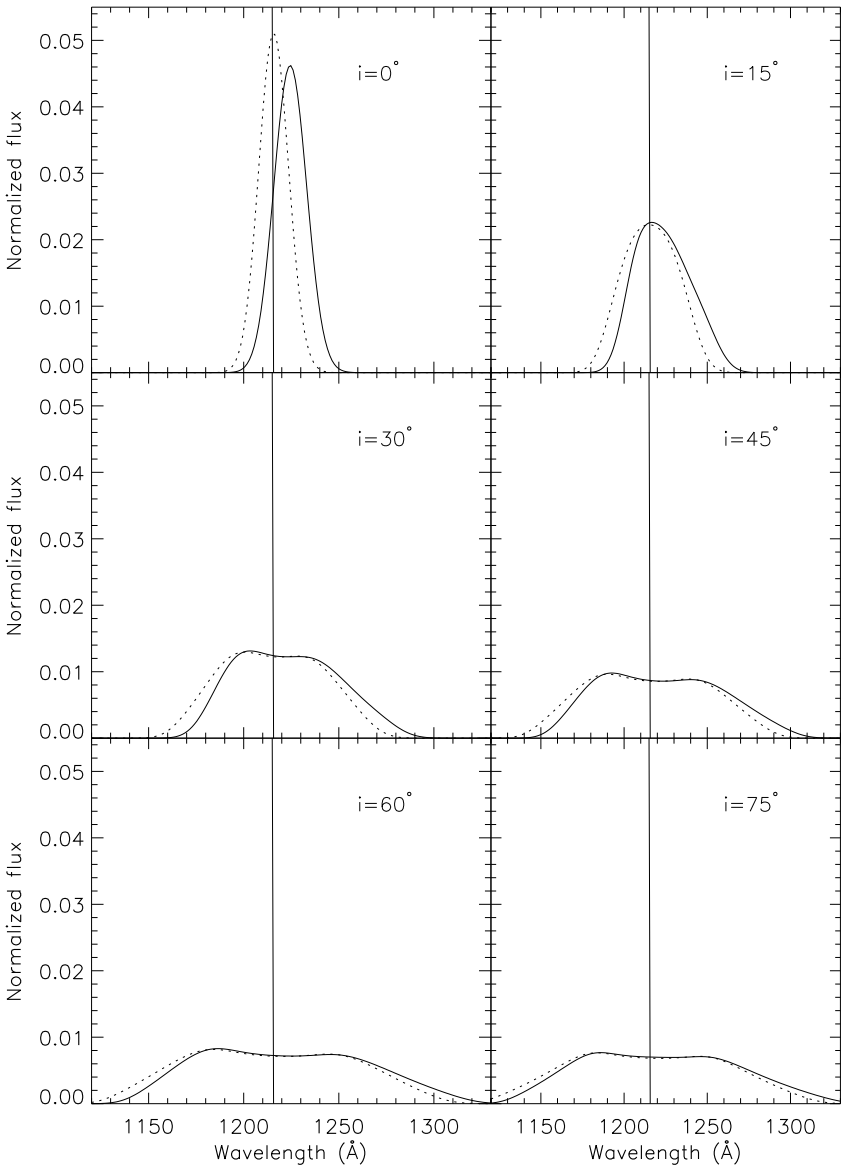

Figure 32 Grid of profiles of the Lyα BEL without relativistic effects (dotted) and with relativistic effects (solid). From one panel to the other, only the inclination varies. All the other model parameters have been mentioned in Section 5.2.3, namely $\xi_1 = 132 r_g$, $\xi_2 = 1320 r_g$, $\eta = -2$, $q = 3$, $\lambda = 15°$, and $\tau_0 = 10^3$.

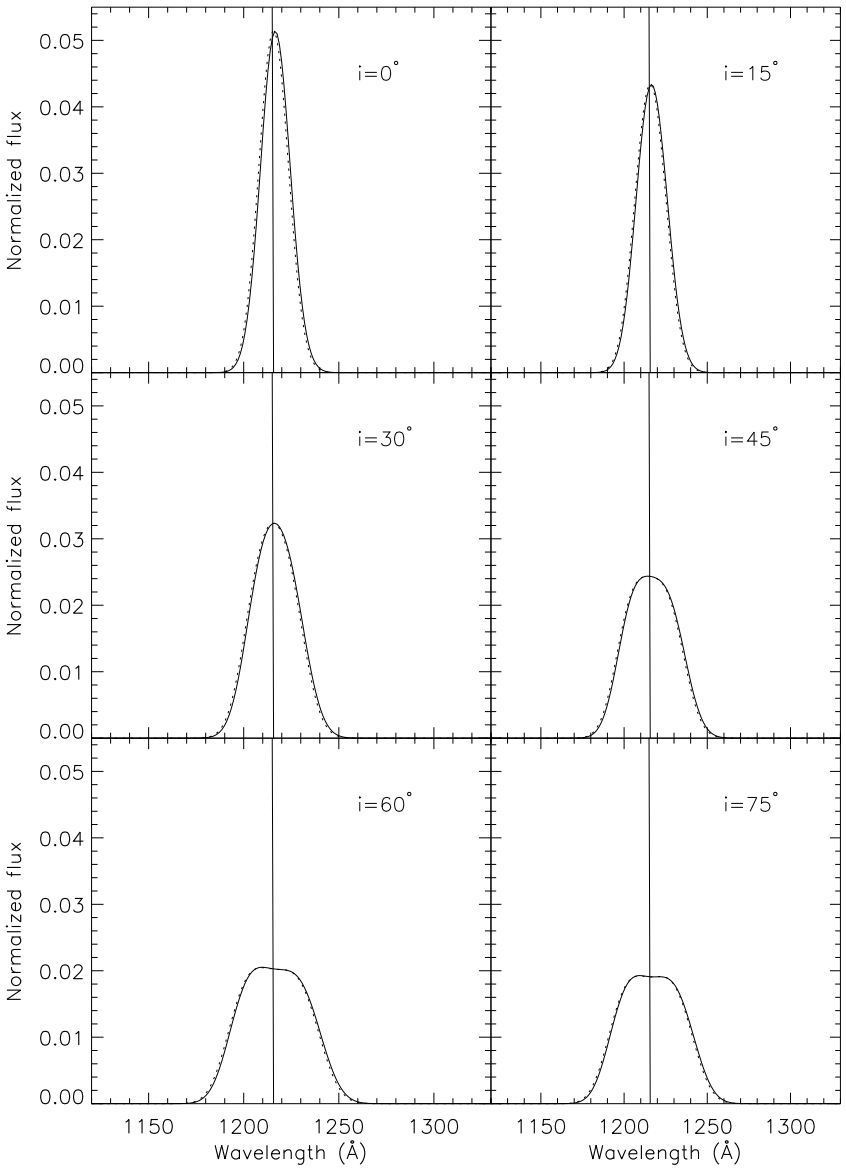

Figure 33 Grid of profiles of the Lyα BEL without relativistic effects (dotted) and with relativistic effects (solid). From one panel to the other, only the inclination varies. All model parameters are the same as in Figure 32, except $\xi_1 = 1320 r_g$ and $\xi_2 = 13200 r_g$.

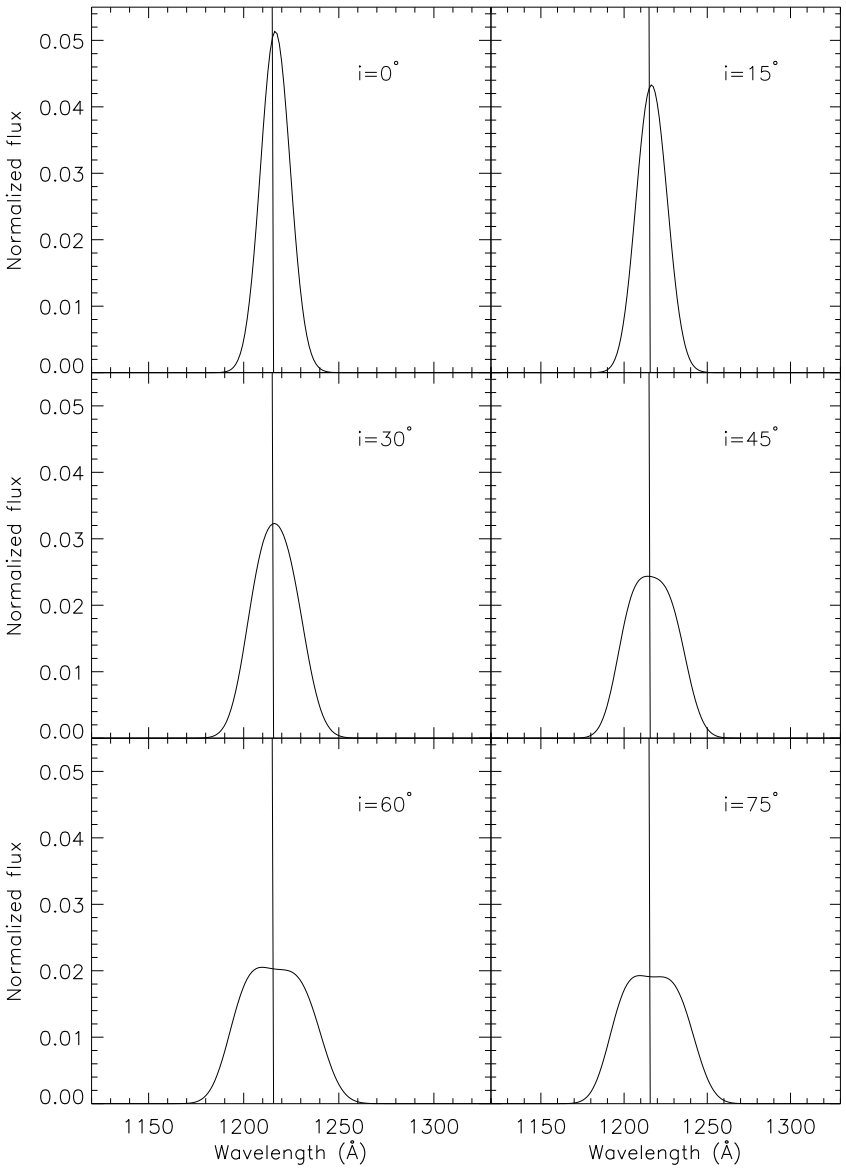

Figure 34 Grid of profiles of the Lyα BEL with relativistic effects. From one panel to the other, only the inclination varies, with the wind opening launch angle at $\lambda = 15°$ with the Murray et al. (1995) Q-value.

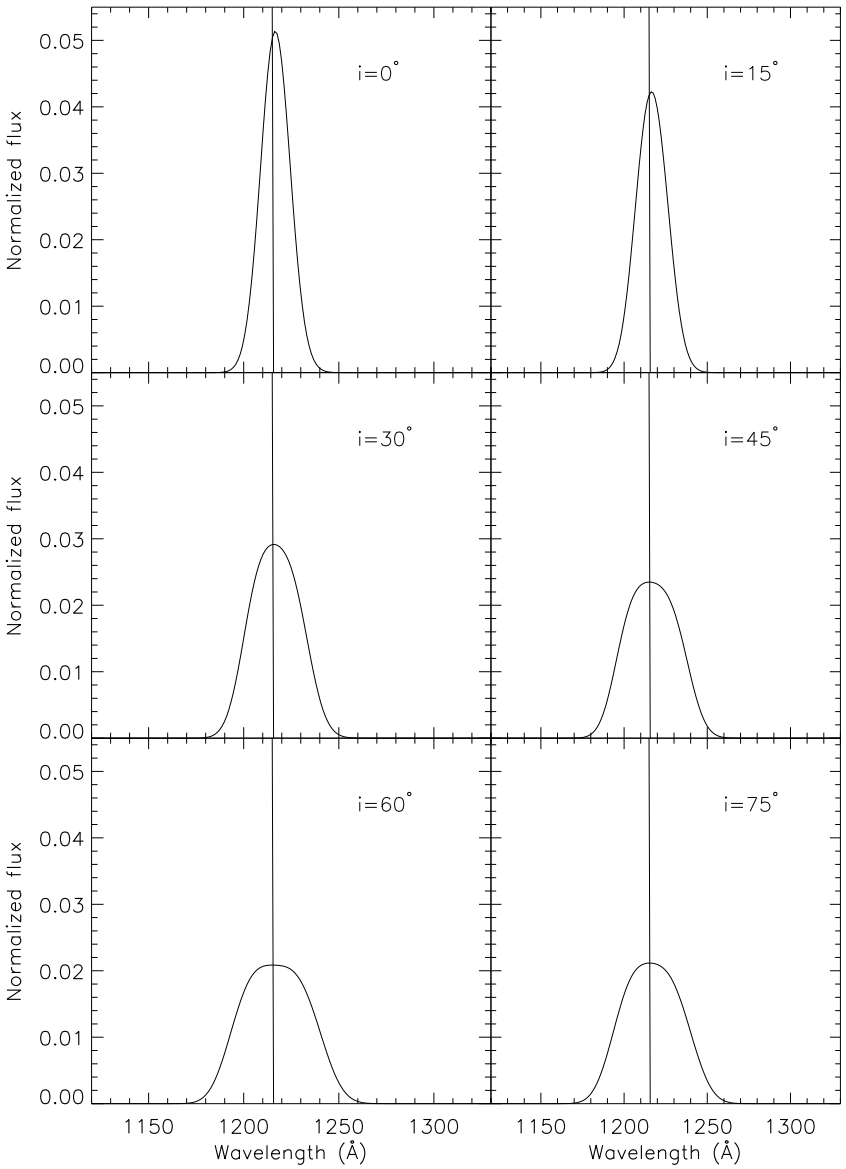

Figure 35 Grid of profiles of the Lyα BEL with relativistic effects. From one panel to the other, only the inclination varies, with the wind opening launch angle at $\lambda = 45°$ with the Murray et al. (1995) Q-value.

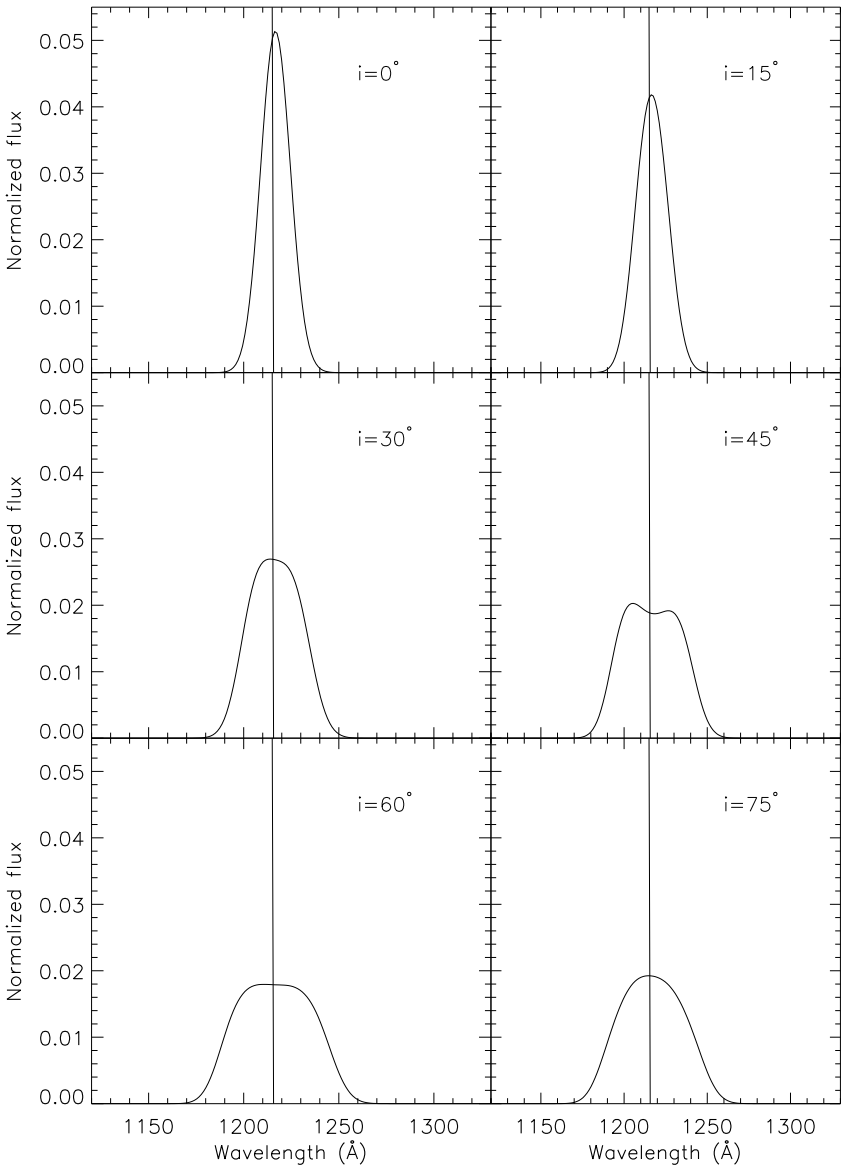

Figure 36 Grid of profiles of the Lyα BEL with relativistic effects. From one panel to the other, only the inclination varies, with the wind opening launch angle at $\lambda = 85°$ with the Murray et al. (1995) Q-value.

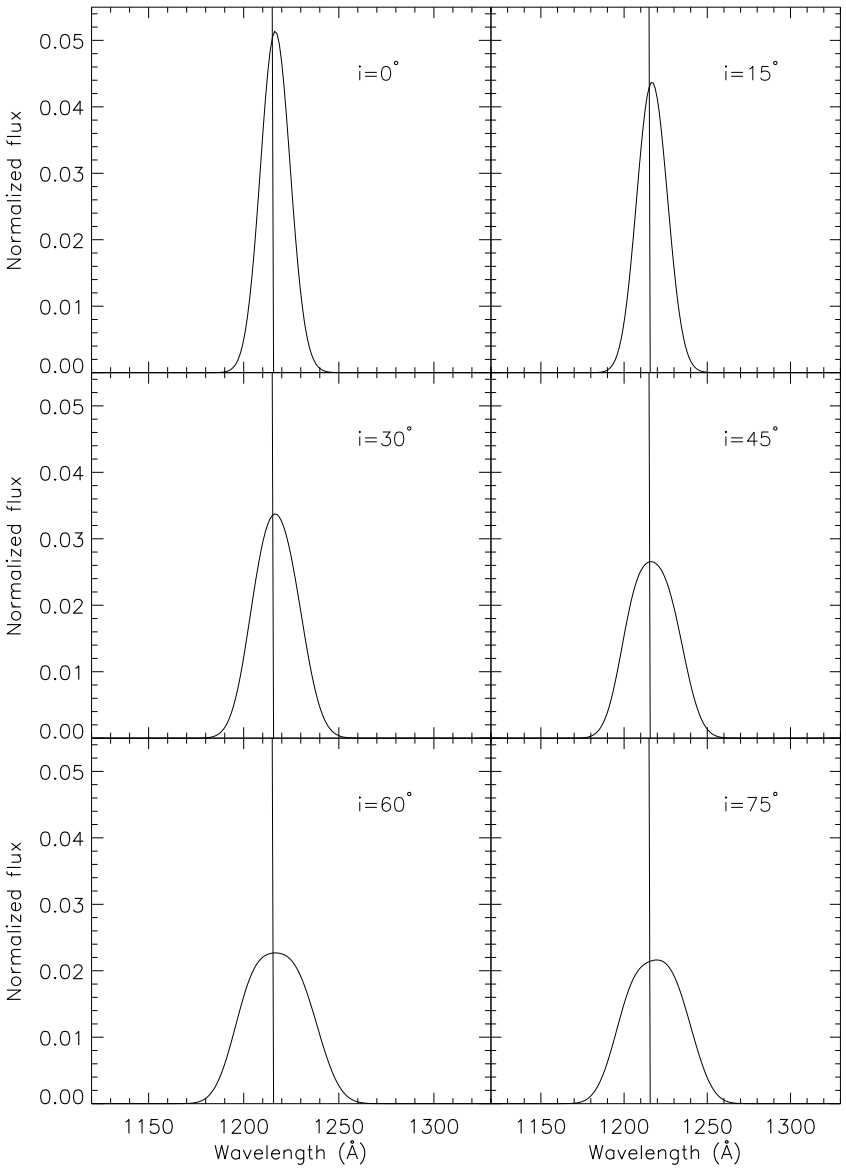

Figure 37 Grid of profiles of the Lyα BEL with relativistic effects. From one panel to the other, only the inclination varies, with the wind opening launch angle at $\lambda = 15°$ with the Hall & Chajet (2010) Q-value.

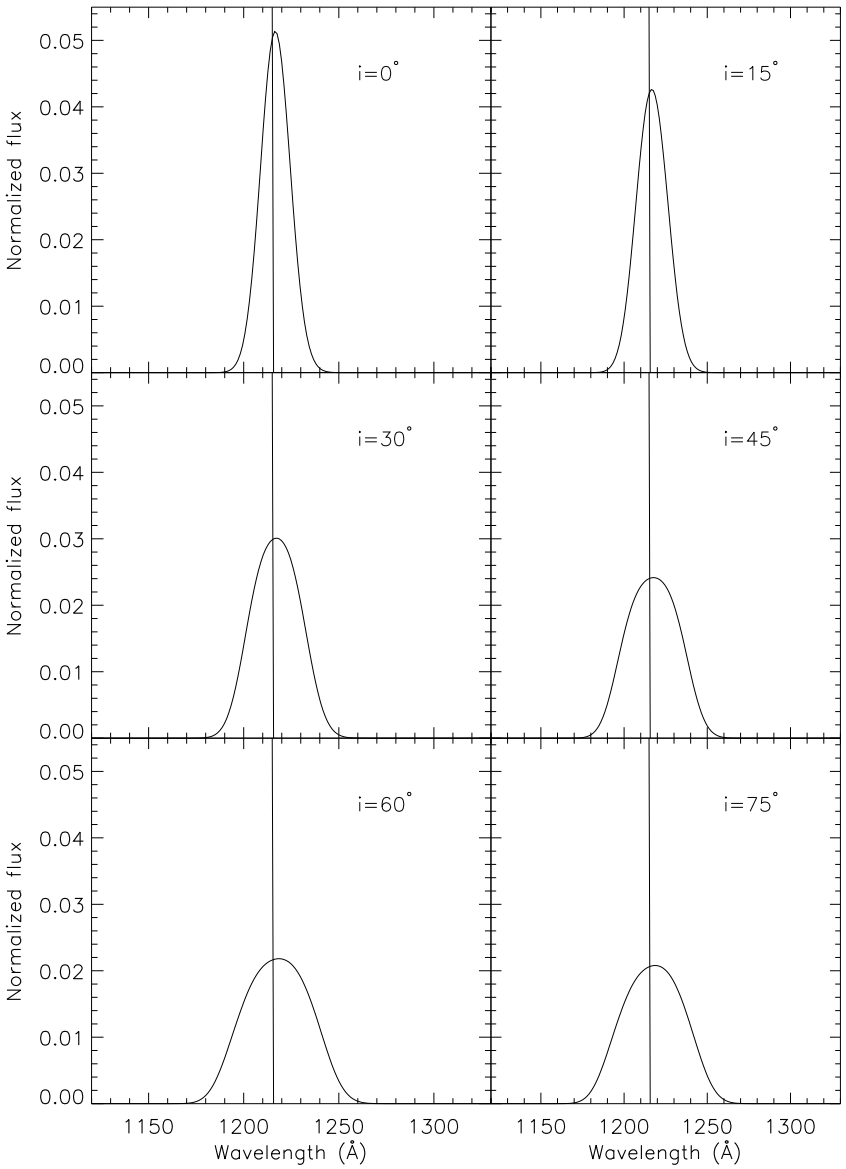

Figure 38 Grid of profiles of the Lyα BEL with relativistic effects. From one panel to the other, only the inclination varies, with the wind opening launch angle at $\lambda = 45°$ with the Hall & Chajet (2010) Q-value.

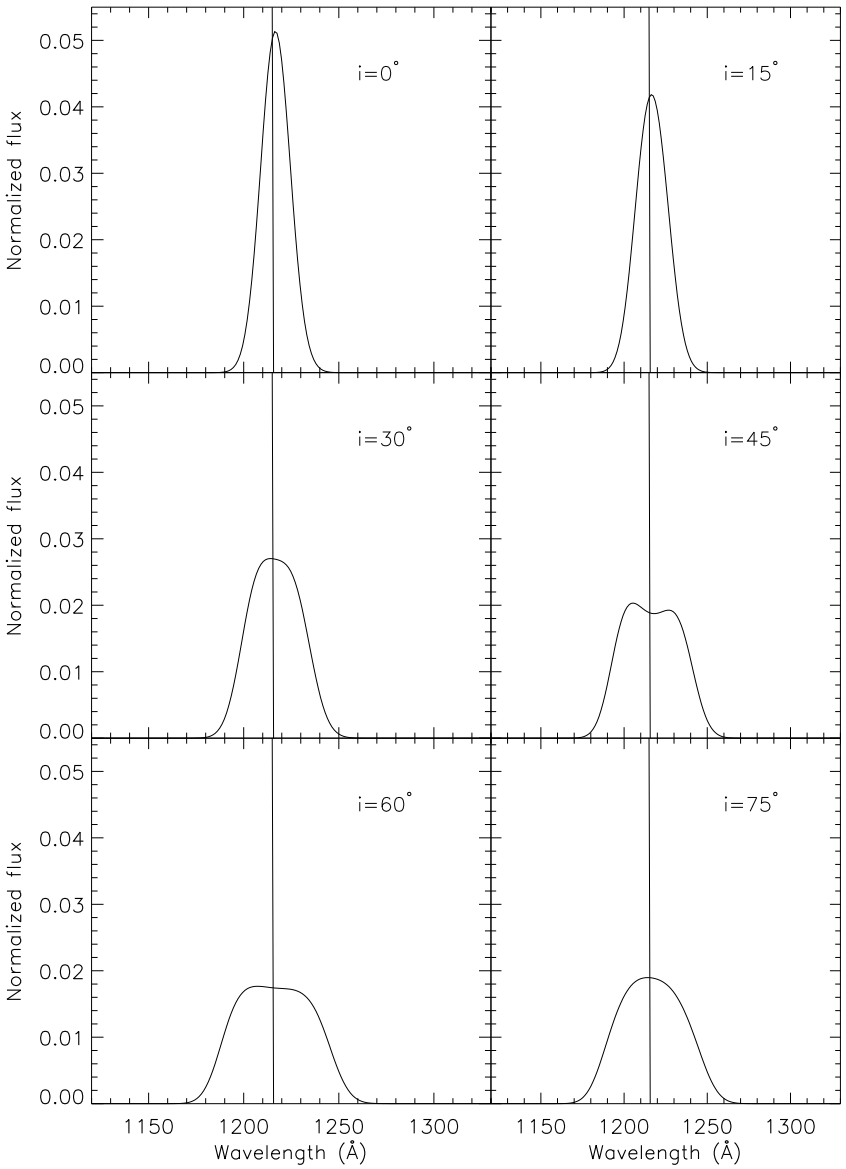

Figure 39 Grid of profiles of the Lyα BEL with relativistic effects. From one panel to the other, only the inclination varies, with the wind opening launch angle at $\lambda = 85°$ with the Hall & Chajet (2010) Q-value.

5.3 BROAD ABSORPTION LINE REGIONS

The classic BALs are defined as those having velocity widths which are contiguous with velocities >2000 km s^{-1} at absorption depths > 10% below the continuum emission (Weymann et al. 1991). The features of BALs are very diverse. One common feature is blueshifted absorption with respect to the adjacent emission. The absorption may occult the continuum emission and BEL if it is attached to the BEL. These BAL troughs are sometimes saturated even if they are not black. Regardless of diversity, it is evident that BALs occur in the outflows on a scale larger than the size of continuum source and the BELRs. The outflow could be a smooth continuous flow, or a flow of many individual clouds. In either case, the line profiles of these absorptions are influenced by source coverage factors and optical depth effects in velocity space. A simple situation to consider is one in which the absorber has a constant optical depth independent of velocity τ across the projected area of an extended emission source along the observer's line of sight. However, the general expression for the observed intensity of BAL profiles at some particular velocity v depends on τ_v and is

$$I_v = q_v I_{o,v} e^{-\tau_v} + (1 - q_v) I_{o,v} + q'_v I_{BEL,v} e^{-\tau_v} + (1 - q'_v) I_{BEL,v} \tag{5.16}$$

where $I_{o,v}$ is the intensity of the continuum emission source at velocity v, $I_{BEL,v}$ is the intensity of the BEL at velocity v, q_v is the fraction of the central continuum source covered by absorbing material as seen along our line of sight at velocity v, and q'_v is the fraction of the BELR covered. Here it is assumed that τ_v is uniform over the region it occults, but is otherwise zero. In order to obtain significant absorption the viewing angle of the distant observer may play an important role.

Also, the depth and equivalent width can vary over time, which provides a means to constrain the physical parameters of absorbers. Usually these are studied in a continuum region of the spectrum where no BEL is present, and we can neglect the last two terms in Equation 5.16. Time variability of these absorption troughs, such as changes in its absorption strength as a function of velocity, and the emergence of BAL outflows, are believed to be caused by a change of ionization state, and/or motion of the absorbing gas across the line of sight. These possible causes of variability are useful for determining the change in

electron density and covering factor along the observer's line of sight. In the former case, the variability timescale $t_{\rm var}$ provides an estimate of electron density, $n_e = \frac{1}{\alpha \times t_{\rm var}}$, where α is the recombination coefficient (e.g., Hamann et al. 1997; Narayanan et al. 2004). In the latter case, the variability timescale corresponds to the time it takes the absorbers to cross the background continuum source. If we suppose that the absorbers have sharp edges, the minimum value of crossing velocities can be determined as $v_{\rm cross} \geq [C_{\rm f}(2) - C_{\rm f}(1)] \times D/t_{\rm var}$, where $v_{\rm cross}$ is the crossing velocity, D is the size of the continuum, and $C_{\rm f}(1)$ and $C_{\rm f}(2)$ are covering factors in the variation time interval $t_{\rm var}$ (Misawa et al. 2005).

Reports of time-variable absorption have been relatively common in quasar BALs. Such variability can even include the extreme cases of the appearance or disappearance of absorption. Studies suggest that the time variability of BAL profiles has a time scale of years in the absorber's rest frame (Hamann et al. 1997). In all cases (i.e., Ma 2002; Hamann et al. 2008; Krongold et al. 2010; Rodriguez Hidalgo et al. 2012), the most favored explanation is the transverse motion of the absorbing gas across the continuum. Given the variability time scale of BALs with the transverse velocity, the structure of BALRs can be estimated.

Despite the observed variability in BALs, outflow velocity shifts between epochs indicate insignificant acceleration of the outflowing gas along our line of sight. For example, Vilkoviskij & Irwin (2001) reported the outflow velocity of CIV BAL in Q1303+308 had increased in magnitude by $55\,{\rm km\,s^{-1}}$ over 6 years, corresponding to an acceleration of $\sim 0.03\,{\rm cm\,s^{-2}}$. Hall et al. (2007) found evidence in the quasar SDSS J024221.87+004912.6 for an average acceleration of CIV BAL trough of $0.15\,{\rm cm\,s^{-2}}$ over 1.4 years. Although the authors claimed to detect a change in line strength between two epochs (a shift of three pixels in SDSS spectra, corresponding to a velocity shift of $68\,{\rm km\,s^{-1}}$), it is worth noting that such a change in BAL strength could also be interpreted as a change in optical depth. Nevertheless, the observational results favor that the absorbing gas and clouds are compact and patchy in their distribution and, there is a lack of acceleration along the observer's line of sight. The BAL outflows could be clumpy or filamentary.

6.0 ANALYSIS

The empirical model we built integrated the work in Chapter 5. For example, it allows us to study the size scale of the BALR. To minimize the number of free parameters in the model, we employed the constraints from spectral analysis and photoionization calculations. First, we chose the object SDSS J114548.38+393746.6 as a test case for the empirical model. The quasar has an emission redshift $z = 3.1045$. In this quasar the BELs show no apparent peak offsets in the rest frame. We measured the FWHM of the CIV BEL and the monochromatic luminosity at 1350 Å. Combining these with the overall source spectrum and the reverberation mapping results from Equations 3.8 and 3.11, we were able to deduce a mass of $2 \times 10^8\, M_\odot$ for the SMBH, and a minimum distance of $\sim 1320 r_g$ for the CIV BELR from the center of the SMBH, where the gravitational radius is defined as $r_g = GM_{BH}/c^2$.

Using the reverberation mass and the formalism for the standard radial disk structure of a relativistic thin α-disk in Section 5.1, we computed the continuum flux from the accretion disk. There are a few free parameters needed to be defined (details in Section 5.1.2). First, the normalized accretion rate $\dot{m}$ is used with the SMBH mass to determine the disk temperature, which defines the shape of the UV to optical continuum. Davis et al. (2007) concluded that the slope generally decreases as $M_{\rm BH}$ increases at a fixed disk luminosity, implying a constant $\dot{m}$. To estimate the continuum slope of J114548.38+393746.6, we adopted the reverberation mass and adjusted the value of $\dot{m}$. We found a result similar to Collin et al. (2002), i.e., that the accretion rate is close to the Eddington limit in most luminous quasars if the optical luminosity is emitted by a steady, optically thick, geometrically thin accretion disk. Second, the black hole spin parameter $a = cJ/GM^2$ is used to determine the strength of relativistic effects. In our case, we chose the rapidly rotating black hole with a=0.998, which is more realistic since the accreting disk material will spin up the black hole.

Third, the inner and outer radii of the disk influence the amount of computed luminosity. A higher luminosity for the disk can be obtained with a larger disk surface. An outer radius of $2 \times 10^4 r_g$ is usually taken and appropriate. This large radius corresponds to a distance where the self-gravity of the accretion disk begins to dominate over the gravity of the black hole, and the disk becomes gravitationally unstable (Collin & Huré 2001). With all the parameters reasonably defined, we divided the disk into 20 concentric annuli and computed the flux emission for each individual annulus. In the calculation we found that over 95 percent of the total continuum flux comes from the inner $\sim 125 r_g$ region shown in Figure 25.

The next step was to compute the often-observed single-peaked BELs. We adopted the Murray et al. (1995) disk-wind model with relativistic effects described in Section 5.2. The location of the BELRs can be estimated using results from reverberation mapping studies as discussed in Chapter 3. Studies show that size scales of high-ionization BELs are formed closer to the central source than those of low-ionization BELs. For example, in quasars, the high-ionization CIV BEL is formed at a region roughly three times smaller than that of the MgII BEL, while the lower-ionization Hβ BELR is at a distance three times farther than the MgII BELR. In our simulation, the inner radius of the BELR ξ_1 was taken from the reverberation mapping distance, $\xi_1 = R_{BELR}$, while the outer radius was assumed to be $\xi_2 = 10 R_{BELR}$ so that the outer region is less ionized with negligible emission. In our test case, the distance of the CIV BEL from reverberation mapping results is $R_{BELR} \sim 1320 r_g$, and the distance of the Lyα BELR is similar. In the BELRs, an emissivity of $q = 3.1$ was adopted. In the first calculation we chose an inclination angle $i = 45°$ measured from the disk axis. A lower inclination (i.e., face-on) tends to smear the double peak feature by diminishing the Doppler boosting of a rapidly rotating disk, while for a higher inclination (i.e., edge-on) at $i > 67°$ the line emission tends to be occulted by the dusty torus at the equatorial plane. Technically, we found that the presence of disk emission in J114548.38+393746.6 is difficult to detect in the profiles where the far wings are not prominent and blend with the continuum, which causes difficulty in determining the inclination angle as well. In our model, we extensively explored the combination of opening angle λ of the wind launched from the accretion disk and the inclination angle i to the observer. We are able to produce the often-observed single-peaked profile but it is difficult to produce any highly-asymmetric

and blueshifted profiles, which are seen in some observations. The width of a line profile (e.g., the Lyα BEL) is mainly due to disk rotation. Assuming the rotation is counterclockwise, we map out the intensity of the Lyα BEL flux from each part of the disk for seven wavelengths on the Lyα line profile as shown in Figures 41 and 42 for wind opening angles of $\lambda = 15°$ and $\lambda = 85°$, respectively. The inner small grey filled circle represents the region with 95% of the continuum emission.

Using the specific flux maps of the continuum and BELR, we are able to determine the BALR size using the result that classical BALs occult the BELs. To understand the structure of the BALR, partial coverage of the continuum emission by parts of the BALR plays an important role. We placed some constraints on the physical properties of the outflow by making a few reasonable assumptions. One of them is from the studies of investigating variability in high-ionization BALR species such as CIV and SiIV (e.g., Barlow et al. 1992b; Lundgren et al. 2007; Gibson et al. 2008; Hamann et al. 2008; Gibson et al. 2010). These findings are consistent, and they suggest that BAL variations are due to the motion of absorbing gas across the line of sight. The characteristic time-scales of the gas crossing the continuum source are measured to be in the range of 1-5 years. If the outflowing gas is located just beyond the continuum region, and it has a transverse speed equal to the Keplerian disk rotation speed, given the crossing time-scale and the photoionization results, we can estimate the physical distance and size scale of the absorbers.

We employed the earlier results on the continuum and BELRs to derive some basic physical parameters of the BALRs. Adopting the continuum luminosity at 1350 Å in the quasar rest frame, $\lambda L_\lambda \sim 2 \times 10^{46}\,\mathrm{erg\,s^{-1}}$, and the FWHM of the CIV BEL of $\sim 4000\,\mathrm{km\,s^{-1}}$, we calculated the SMBH mass to be $2 \times 10^8 M_\odot$ from the reverberation mapping results. This implies that the characteristic radius for the CIV BELR is $R_{BELR}(\mathrm{CIV}) \sim 0.15\,\mathrm{pc}$. In our empirical model, we computed the characteristic size of the continuum source at 1350 Å to be $D_{1350\,\mathring{A}} \sim 10^{-3}\,\mathrm{pc}$ for this quasar, with bolometric luminosity L_{Bol} of $\sim 5.6 \times 10^{46}\,\mathrm{erg\,s^{-1}}$, where L_{Bol} was determined by assuming $L_{Bol} = 4.1 \times 10^4 \lambda L_\lambda^{0.91}$ (Runnoe et al. 2012). We used a simple geometry assumption that the BALR gas with a sharp edge shares the Keplerian disk rotation speed and crosses the line of sight over a time scale of a year. Note that the strength of the BALs has been observed to become weaker and then disappear in a year. Taking the

assumption of the transit time of the absorbing gas across the continuum $D_{1350\,\mathring{A}} \sim 10^{-3}\,\mathrm{pc}$ to be a year, the transverse velocity perpendicular to the line of sight is roughly $v_{\perp} \sim 1000\,\mathrm{km\,s^{-1}}$ for gas at a distance of $R_{BALR} \sim 1\,\mathrm{pc}$ from the central source. This immediately leads to the estimate that the transverse length of a clump of absorbing gas is $l_{BALR} \sim 10^{-3}\,\mathrm{pc}$. Photoionization models suggest that the ionization parameter U is of order ~ 0.1 for absorbing gas irradiated by a "standard" AGN spectrum. Given the bolometric luminosity of the quasar and distance of the BALR, the number density of hydrogen in the absorbing gas can be estimated by $n_H \sim 10^{10} L_{46} R_{17}^{-2} U_{0.1}^{-1}\,\mathrm{cm^{-3}}$ with L_{46} being the luminosity of the central engine in units of $10^{46}\mathrm{ergs^{-1}}$, R_{17} being the size of the BALR in units of $10^{17}\,\mathrm{cm}$, and $U_{0.1}$ the ionization parameter normalized to 0.1. This indicates $n_H \sim 7 \times 10^{9}\,\mathrm{cm^{-3}}$. Estimates of the total column density of the absorbing gas are difficult to obtain due to saturation of the lines, but results on the absorption of x-rays in BAL quasars suggests that the column densities lie in the range $N_H \sim 10^{21} - 10^{23}\,\mathrm{cm}$ (Gallagher et al. 2004, and reference therein), so that the effective total thickness of the absorbing layer is $D_{BALR} = \frac{N_H}{n_H} \sim 4.8 \times 10^{-6}\,\mathrm{pc}$ after adopting the high column density of $10^{23}\,\mathrm{cm^{-2}}$. In addition, comparing the distance of the absorbing region with the thickness of the absorbing layer, we arrive at a very small filling factor for the absorbing gas if it is assumed to be spread all along the line of sight, $f_{BALR} = \frac{D_{BALR}}{R_{BALR}} \sim 5 \times 10^{-6}$. Table 3 shows the physical parameters of the BALR in quasars for a SMBH mass of $2 \times 10^{8} M_{\odot}$ and a bolometric luminosity of $\sim 7 \times 10^{45}\,\mathrm{erg\,s^{-1}}$ for three different distances of the BALR: R_{BALR} ~0.15 pc (right beyond the BELR), R_{BALR} ~1 pc, and R_{BALR} ~1 kpc (galactic-scale distance). Given the result that classical BAL outflows should lie beyond the BELR indicates that the absorbing gas is clumpy or filamentary with the clumps having a size scale of $\sim 10^{-3}\,\mathrm{pc}$.

Table 3. Physical parameters of BAL in Quasars.

	Case I	Case II	Case III
$R_{\rm BALR}$(pc)	0.15	1	1,000
$v_{\perp}$(km s^{-1})	2,300	1,000	30[1]
$l_{\rm BALR}$(pc)	2.4×10^{-3}	10^{-3}	3×10^{-5}
$n_{\rm BALR}$(cm^{-3})	3×10^{11}	7×10^{9}	6.7×10^{3}
$D_{\rm BALR}$(pc)	1×10^{-7}	5×10^{-6}	5×10^{-3}
$f_{\rm BALR}$	7×10^{-7}	5×10^{-6}	5×10^{-3}

[1]The value is calculated based on a Keplerian disk. The result of the rotation curve of spiral galaxies suggests the velocity to be 100 km s^{-1}at roughly kiloparsecs (Begeman et al. 1991).

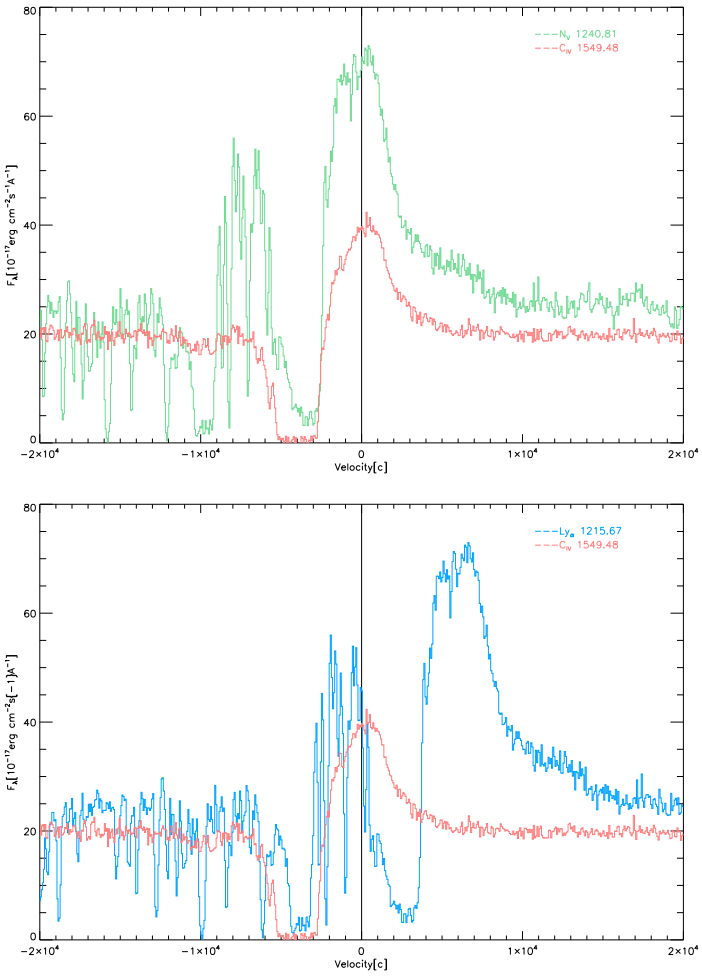

Figure 40 Spectrum of the quasar SDSS J114548+393746 in the regions of Lyα and Nv, compared to that of Civ, in velocity space.

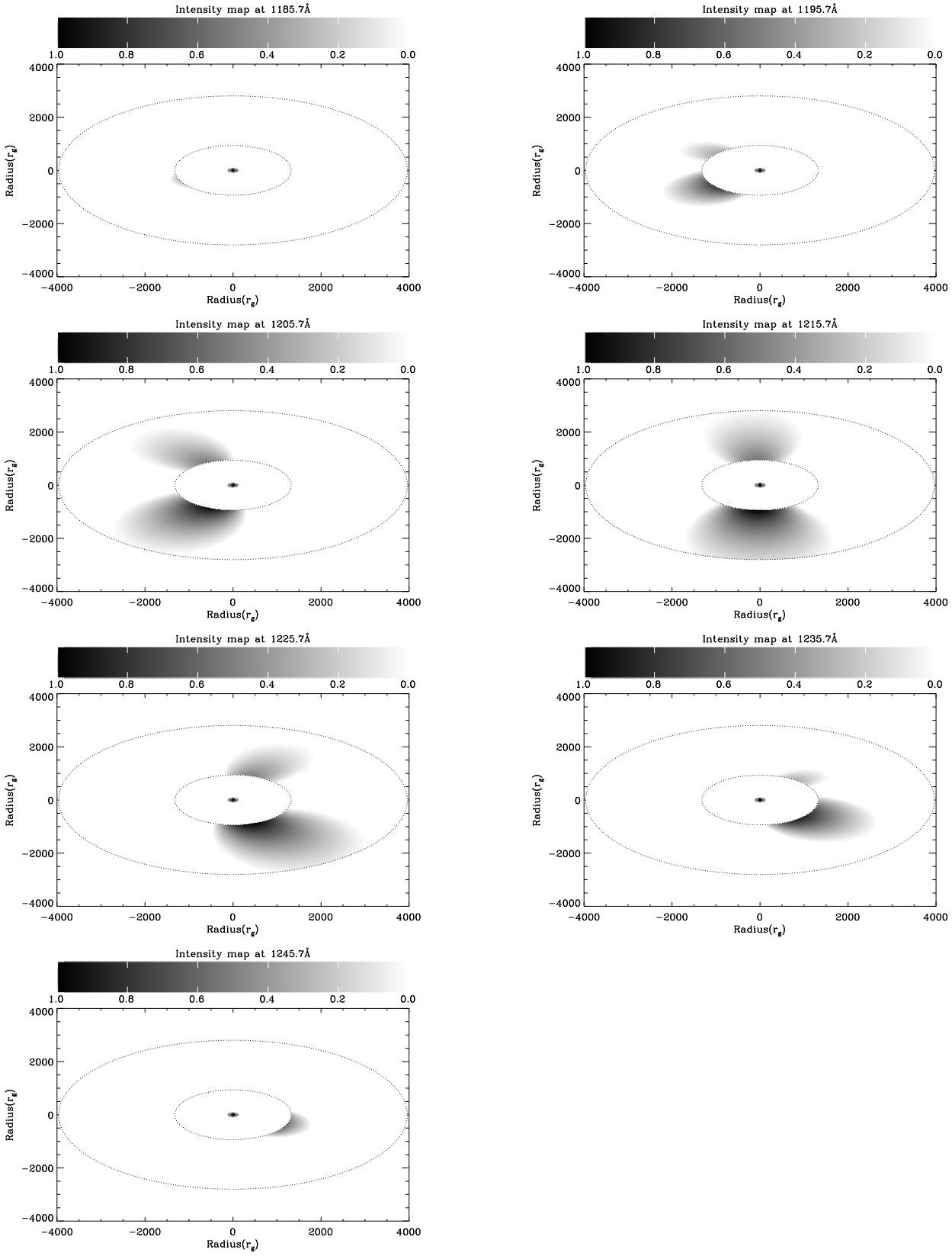

Figure 41 Log-intensity map of the Lyα BEL at the wavelengths, 1185.7 Å, 1195.7 Å, 1205.7 Å, 1215.7 Å, 1225.7 Å, 1235.7 Å, and 1245.7 Å, through the disk wind at $\lambda = 15°$.

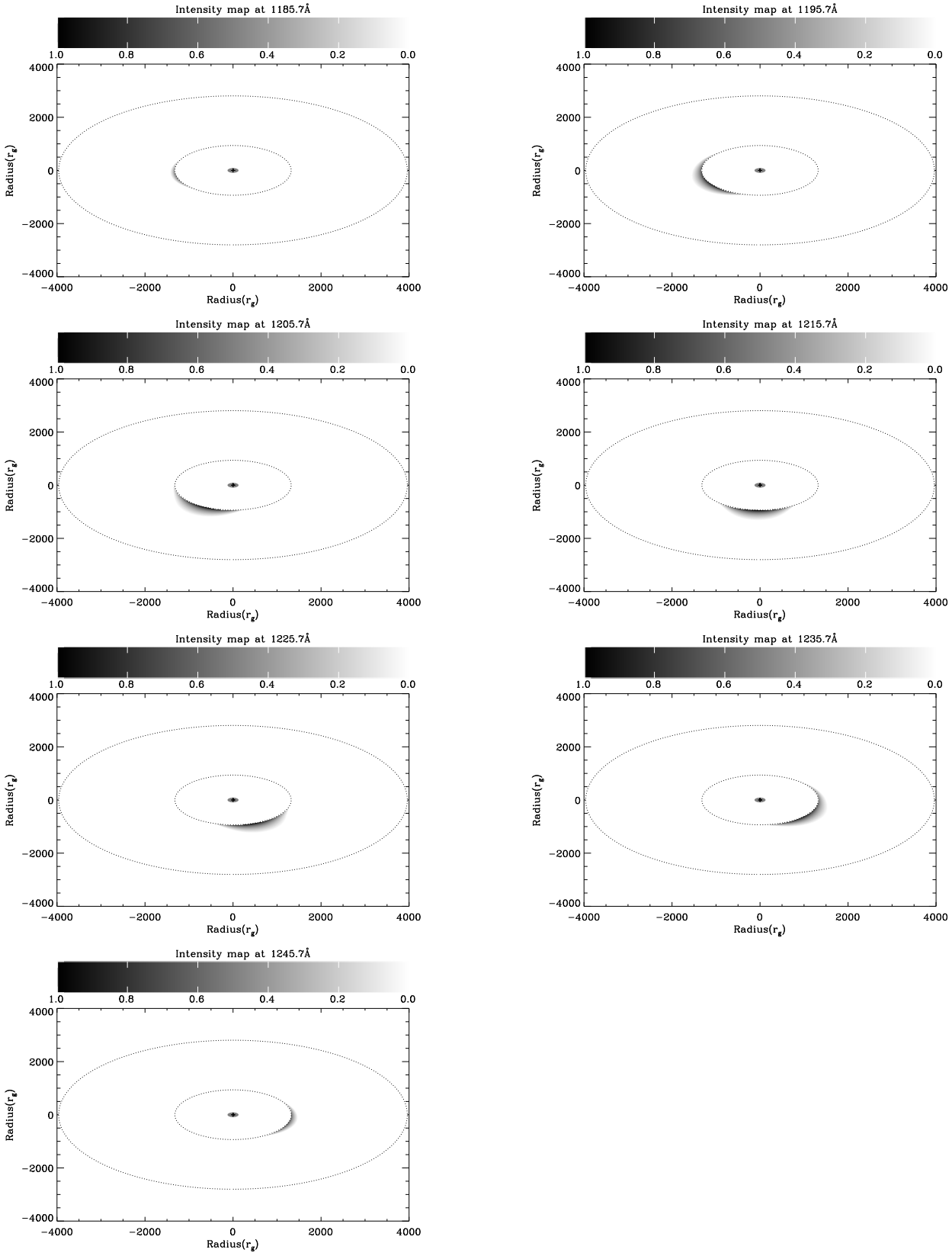

Figure 42 Log-intensity map of the Lyα BEL at the wavelengths, 1185.7 Å, 1195.7 Å, 1205.7 Å, 1215.7 Å, 1225.7 Å, 1235.7 Å, and 1245.7 Å, through the disk wind at $\lambda = 85°$.

7.0 DISCUSSION OF BALR SIZE SCALES

We have made progress on specifying an empirical model for the structure of quasars. However, there are ambiguous results on BALR size scales, so a major challenge with interpreting BALR outflows is the uncertainty in the distance between the location of the observed BALR gas and the central SMBH. Erroneous distance estimates could lead to a vast diversity in inferred physical properties (e.g., kinetic luminosity and mass flux) for BALRs, which would mislead our understanding. Most of the physically-inspired scenarios suggest that the outflows emerge from an accretion disk, and that the observed BALRs are in a wind approximately one parsec from the central nucleus. This is the scenario we have adopted in our empirical model. In contrast, however, reported distances between the SMBH and the BALR have range from ~ 0.01 pc to > 10 kpc. Furthermore, some recent studies have favored large distances. Such galactic-scale outflows could play a major role in feedback in galaxy evolution.

In the context of our work, there are three ideas for mass ejection from quasars/AGN which we will describe. One is a wind driven off an accretion disk by radiation pressure (Murray et al. 1995; Elvis 2000; Proga et al. 2000) that leads to the outflowing BALR gas sometimes seen in the optical/UV spectra of quasars. Another related model is a wind formed by photoionized evaporation from the inner edge of the torus (Krolik & Kriss 2001), which is believed to be closely aligned with the inner accretion disk. This second idea has been proposed to explain the phenomenon of warm absorbers sometimes seen in the x-ray spectra of AGN. We discuss both ideas since BALs and warm x-ray absorbers may be related in some way. The last idea is that outflows could be from galactic winds, which may be driven by supernova explosions or hot stellar winds.

7.1 ADW ORIGIN FOR THE BALR

Murray et al. (1995) proposed an accretion disk origin for the BALR gas and a model for driving the winds radially off the accretion disk. Typically, in the disk-wind structure of quasars, the BELR gas is embedded near the surface of the accretion disk and it moves with the Keplerian velocity of the disk. Using analytic arguments, Murray and collaborators found that such a wind from an accretion disk could be launched between the optical/UV continuum emitting region and the region of the disk that gives rise to BELs. Once launched, the winds are accelerated radially under radiation pressure up to velocities approaching one tenth the speed of light by the powerful optical/UV accretion disk continuum emission. The winds also have an azimuthal velocity component since they are launched off of the rapidly rotating accretion disk. Consequently, if the quasar is viewed through the wind, blueshifted BALs are observed. Likewise, Elvis (2000) has suggested that absorbing outflows initially emerge perpendicular to the accretion disk, and are then accelerated radially. BALRs form within the walls of a bi-funnel centered on the quasar's nucleus. Elvis notes that such bi-conical winds viewed at different angles may explain the many varieties of BAL features seen in quasar spectra. Despite the somewhat different wind geometries, in both scenarios BALs originate from an accretion disk wind and they are closely associated with the BELRs.

The theoretical conjecture that the BALR is not much larger than the BELR comes from consideration of the radiative acceleration mechanism, which generally requires that the outflow start at a distance comparable to or less than the size of the BELR (i.e., < 0.15 pc) in order to reach the high speeds that are sometimes observed (e.g., Arav & Li 1994). Arav & Li (1994) point out that where the outflow starts is a crucial point. They note that if gas is introduced over a range of radii by launching it upward from different parts of a disk, material launched closer to the optical/UV continuum source will be accelerated to higher velocities than the material launched further out. This could explain why BALs, once they are fully formed, appear to cover a range of terminal velocities that are no longer accelerating.

As discussed in Chapter 5, the observations indicate that the observed N V BALR can cover and occult the Lyα BELR, so the BALR generally lies outside the BELR. This favors a model in which the overall lateral extent of the observed BALR gas is at least twice the

size of the high-ionization BELR, i.e., larger than $\sim 0.3\,$pc. At the same time, the analysis of BAL time variability discussed in Chapter 6 suggests that the observed BALR is not undergoing significant acceleration and it is clumpy, with individual clumps having a lateral scale of $\sim 10^{-3}\,$pc.

7.2 TORUS ORIGIN FOR WARM X-RAY ABSORBERS

Krolik & Kriss (2001) proposed that a wind is evaporated off the inner edge of a torus, which is expected to begin at larger radii, at ~ 1 pc to ~ 10 pc scales. The x-ray radiation from the central nucleus can heat up the torus atmosphere through Compton heating, and the resulting thermal pressure can effectively launch a wind if the thermal velocity exceeds the local escape velocity. Such winds will have maximum terminal velocities on the order of a few 1000 $\mathrm{km\,s^{-1}}$, thus they do not have the characteristics of high-velocity BALs. However, they have demonstrated that such winds may successfully reproduce the observed characteristics of the so-called warm x-ray absorbers and some of the narrower low-velocity UV absorption. Krolik & Kriss (2001) suggested that the maximum distances of these absorbers are $\sim 30\,$pc. As discussed in Chapter 6, for absorbing gas farther from the nucleus the gas is spread more smoothly with a larger volume-filling factor.

7.3 GALACTIC SCALE OUTFLOWS

Galactic scale outflows have been inferred in some AGN and quasars (see e.g., Edmonds et al. 2011, and reference therein), and these outflows may be related to the outflows seen in classical BALQSOs. The evidence for galactic size scales > 1 kpc comes from weak or absent fine structure absorption in low ionization transitions, which allows one to determine or place upper limits on gas density. Photoionization analysis then allows one to determine or place lower limits on the distance of the outflowing absorbing gas from the central ionizing source, with the usual result being that the outflows are found to have galactic scales > 1

kpc from the central source. More recently, similar analyses applied to higher ionization absorption find size scales of 100 pc to 2 kpc (Borguet et al. 2013).

Outflows with size scales > 1 kpc are also suggested from studies of galactic winds, which may be driven by the kinetic energy of supernovae explosions and winds from massive stars in a starburst (Veilleux et al. 2005). Such winds are believed to play an important role in the evolution of galaxies by regulating the star formation rate, and by ejecting heavy elements to the outer parts of the galaxy and beyond.

Finally, some low ionization BALQSOs often referred to as LoBALs (e.g., see Boyce et al. 1996 and Hines et al. 1999) have properties similar to luminous and ultra luminous infrared galaxies (e.g., see Bushouse et al. 2002 and references therein) but which LoBAL outflows are in ADWs or in galactic scale winds remains to be demonstrated. It has been speculated by some that LoBALQSOs have galactic scale winds and that they are in transitional QSO stages (e.g., Lípari & Terlevich 2006).

8.0 BRIEF SUMMARY AND SOME SUGGESTED FUTURE WORK

8.1 SUMMARY

In this thesis I started in Chapter 2 by using a 2.5-dimensional hydrodynamic code to study the feasibility of driving winds off of an accretion disk with radiation pressure. The aim was to study the formation of BELs and BALs in the environment of a luminous accretion disk surrounding a SMBH (i.e., a quasar). In such a model the BELs form in the chromosphere of the accretion disk. However, launching a wind off the disk to eventually accelerate material to form observable BALs proved problematic. Yet, results from the simulation put the problem of forming BELs and BALs in context. In Chapters 3 and 4 I studied and employed the reverberation mapping technique to estimate the size scale of quasar BELRs. In Chapter 5 I introduced an empirical accretion disk wind model which integrated much of the past observational and theoretical work to explain some of the observed properties of BELs and BALs. This empirical model is an insightful bridge connecting theory and observation. It was used to explore various physical effects which could affect the observed properties of BELs. It explained the single-peaked BELs common in quasar spectra, and was used to infer, based on occultation effects, that the BALR lies beyond the inner BELR.

In Chapter 6 I employed this methodology to study the structure of the quasar SDSS J114548.38+393746.6 and some of the properties of BALRs. For this "typical" luminous quasar, most of the continuum emission in the optical/UV is emitted from the accretion disk in a region more than 100 times smaller than the BELRs, at a distance $R_{continuum} \sim 0.001$ pc from the SMBH. Reverberation mapping work suggests that the CIV and Lyα BELRs are both at roughly $R_{BELR} \sim 0.15$ pc in this object, the SMBH mass is $\sim 2 \times 10^8 M_\odot$, and the bolometric luminosity is $\sim 7 \times 10^{45}\,\mathrm{erg\,s^{-1}}$. Occultation effects indicate that the observed

BALR cannot be closer to the central continuum source than the BELR. In the analysis, I found that the typical radial distance of the BALR from the central source may be $R_{\rm BALR} \sim 1\,{\rm pc}$. However, observed variability of BALs indicates that the absorbing clouds in a BALR are very compact and have a patchy or clumpy distribution across the continuum source, with a very small filling factor along the observer's line of sight. Generally, insignificant acceleration of observed BALs is detected over time, which implies that the observed BALR gas has already been driven to terminal velocities (e.g., up to one tenth the speed of light). However, if radiation pressure line-driving alone is responsible for accelerating BAL winds up to their high terminal velocities, the winds almost certainly had to be launched closer to $R_{continuum}$ and not at $R > R_{BELR}$. Evidently the winds which become the observed BALR must be very optically thin while they are in their acceleration phase at $< R_{BELR}$, otherwise they would be observed and seen to accelerate in time-resolved spectroscopy. During such an acceleration phase they would not be able to cover the BELR even if they were optically thick in the resonance lines. With knowledge of the size-scales for the optical/UV continuum region, BELRs and dusty torus, I generated a schematic sightline to a BALQSO as shown in Figure 43 and a logarithmic schematic model of the innermost regions of a quasar as shown in Figure 44. The inclination angle between the disk axis and the observer, and the geometry of the dusty torus, play an important role in determining the observed properties of the BELs and BALs (if present) of a particular quasar.

8.2 FUTURE WORK

It would be ideal if we could use the observed properties (e.g., continuum emission, BEL properties, BAL properties, etc.) of a quasar to deduce its inclination angle relative to our sightline and determine its most fundamental parameters (e.g., black hole mass, black hole spin, kinetic luminosity, metallicity, etc.), however we are far from doing this accurately. As the investigations presented in this thesis indicate, if the accretion disk wind model is to be successfully applied to understand some of the observed properties of quasars, there are some theoretical issues which must be addressed. For example, how the winds are launched

off the surface of the disk and accelerated to terminal velocities must be explained. The work presented in Chapter 2 was unable to launch stable winds off the disk, which suggests inadequate physics (e.g., the need for magnetic fields) or numerical instabilities in the code. Once the issue of launching the BALR wind is sorted out (e.g., with radiation pressure line driving interior to the BELR), it will be necessary to understand how to accelerate the wind to terminal velocities so that it lies beyond and occults the BELR (i.e., Nv BALs occult an inner Lyα BEL). In addition, improved reverberation mapping results for the various BELRs of luminous quasars is important. Reverberation mapping was discussed in Chapters 3 and 4, and it is clear that proper spectral monitoring campaigns could lead to a detailed description of the geometry and kinematics of quasar BELRs. However, this is a long-term future goal since it would be best accomplished with dedicated telescope facilities. Finally, there are important observational clues which can not be explained, such as details of BEL shapes, velocity shifts, and asymmetries. We attempted to explain the observational characteristics of quasar BELs in Chapters 5 and 6 with some success (e.g., single-peaked profiles), but we were unable to explain some of the notable often-observed characteristics (e.g., prominent blue asymmetries) with disk emission. Addition of a scattering component might be used to give rise to Civ BELs with blue asymmetries. Addressing these and other issues in future work are important goals for achieving future progress.

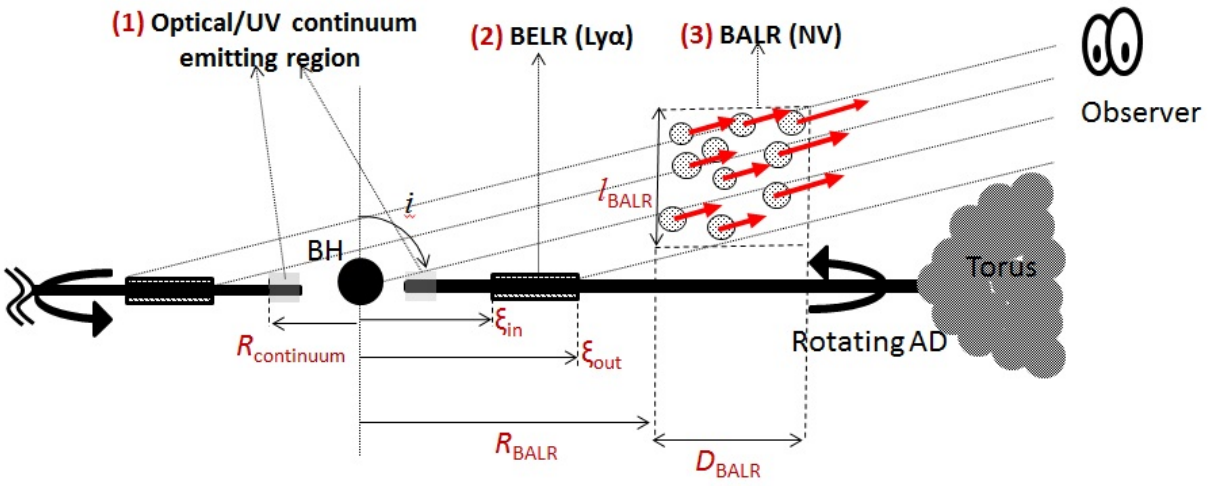

Figure 43 A picture of the sightline to a BALQSO.

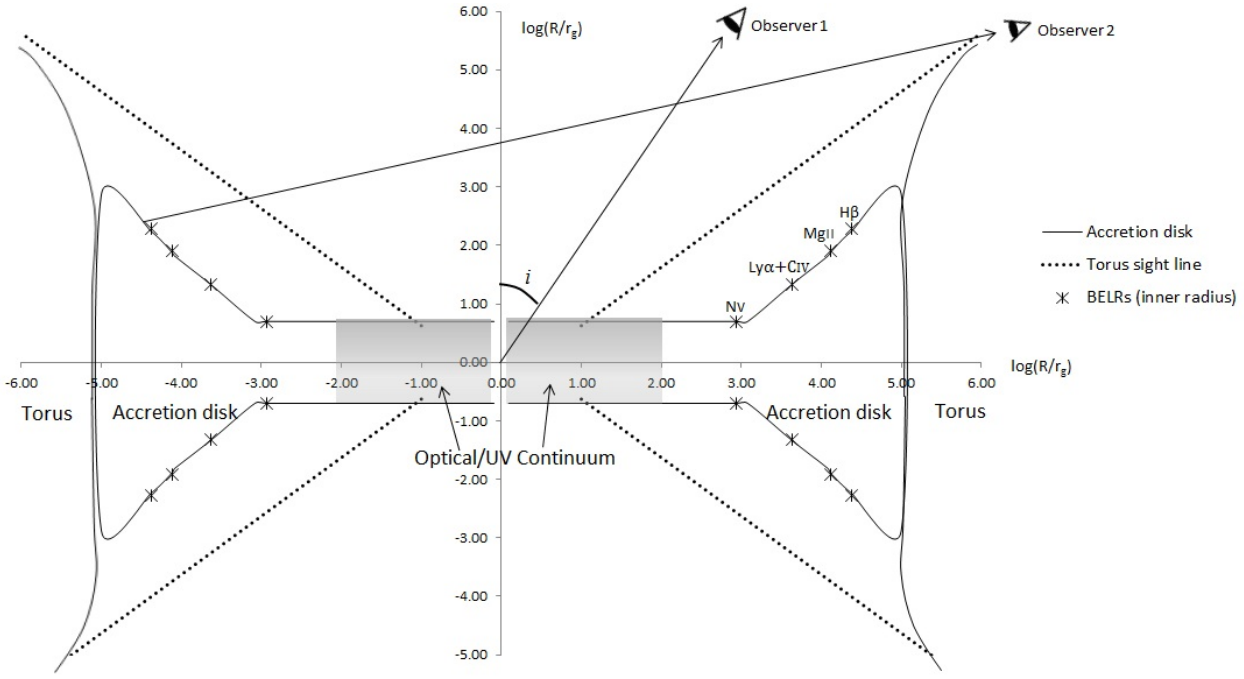

Figure 44 A picture of the innermost part of a quasar, showing the optical/UV continuum and BELRs. With different inclination angles i, the inner region of the AD can be viewed (i.e., by observer 1), while the inner region is obscured by the torus (i.e., by observer 2).

APPENDIX

SOME DETAILS OF THE CALCULATIONS

This chapter describes the Flohic et al. (2012) prescription of computing broad emission line (BEL) profiles for an accretion disk wind model with the analytic prescription of Murray et al. (1995) and Murray & Chiang (1997) to include radiative transfer in a disk wind. Their prescription adopted the Chen et al. (1989) calculation of a relativistic disk in the weak-field limit. For more details I refer the reader to Flohic et al. (2012) and Flohic (2008).

The convention adopted was the geometry defined in Chen et al. (1989) shown in Figure 45. The Cartesian coordinates (x, y, z) is the frame of the observer, and the primed axes (x', y', z') are the frame of the disk. In the calculation, the spherical coordinates (r, θ, ϕ) are used instead, where the primed angles are in the disk frame.

The simple geometry is that the accretion disk is in the $x'y'$-plane with the disk inner and outer radii, r_1 and r_2, respectively. The distant observer is along the positive z-axis at infinity. The rotation axis of the disk is along the z'-axis. The y'- and y-axes coincide, whereas the z- axis is tilted at an angle i away from the z'-axis in the xz-plane, where the angle i is the disk inclination to the observer. Conventionally, low disk inclination (i.e., $i = 0°$) is for the observer viewing a face-on disk, while high disk inclination (i.e., $i = 90°$) is for the observer viewing an edge-on disk. In the spherical coordinates, the plane of the disk is at the polar angle $\theta' = 45°$ in the disk frame. The azimuthal angles ϕ and ϕ' are measured with respect to the x- and x'-axes, respectively. Thus the nearest side of the disk to the observer corresponds to $\phi' = 0°$, while the farthest side of the disk corresponds to $\phi' = 180°$. The disk rotates in the direction of increasing ϕ'. Thus, in the observer's

perspective, the emission from the approaching side of the disk (left) should be blue-shifted, while the emission from the receding side of the disk (right) should be red-shifted.

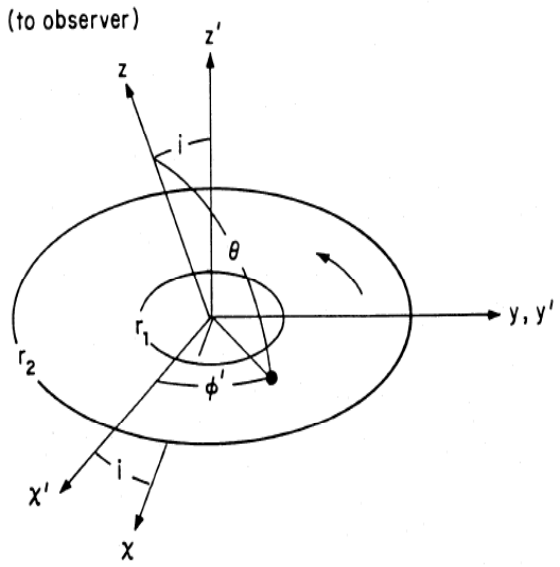

Figure 45 Disk geometry.

The relation between angles in the disk geometry has to be derived before the calculation. In the observer's frame and the disk frame, the unit vectors of a disk-element are

$$\hat{r} = \sin\theta\cos\phi\hat{x} + \sin\theta\sin\phi\hat{y} + \cos\phi\hat{z}$$

and

$$\hat{r}' = \cos\phi'\hat{x}' + \sin\phi'\hat{y}',$$

respectively, where $\hat{r} \equiv \hat{r}'$.

Use of the relations, $\hat{r}\cdot\hat{y}' = \hat{r}\cdot\hat{y}$ and $\hat{r}'\cdot\hat{z} = \cos\theta$, the angles ($\theta$, ϕ, θ', ϕ') are related:

$$\sin\phi' = \sin\theta\sin\phi, \tag{A.1}$$

$$\cos\theta = \sin i\cos\phi'. \tag{A.2}$$

The above relation between the angles will be used to convert the calculation between the observer coordinates and the disk coordinates. The following calculation is divided into two parts. One part is to depict the formalism for relativistic effects in a Keplerian disk. Another part is to describe the analytic prescription for radiative transfer effects of the disk emission.

A.1 RELATIVISTIC EFFECTS IN A KEPLERIAN DISK

The observed line flux at frequency ν is:

$$F_\nu = \int\int I_\nu \, d\Omega, \tag{A.3}$$

where I_ν is the specific intensity and $d\Omega$ is the solid angle subtended by the disk to the observer. The expression of I_ν will be discussed in Section A.2 To compute the double integral, I need to express I_ν and $d\Omega$ in the disk coordinates.

Using the invariance of I/ν^3, the specific intensity of a line in the emitting (disk) frame is:

$$I_\nu = I_{\nu_e} \left(\frac{\nu}{\nu_e}\right)^3 = I_{\nu_e} D^3, \tag{A.4}$$

where $D \equiv \nu/\nu_e$ is the Doppler factor, ν and ν_e are observed and emitted frequency, respectively. Thus, the observed line flux becomes:

$$F_\nu = \int\int I_{\nu_e} D^3 \, d\Omega. \tag{A.5}$$

In general relativity, light bends due to the gravitational potential of the central black hole. The solid angle can be expressed in terms of the impact parameter b:

$$d\Omega = \frac{b \, db \, d\phi}{d^2}, \tag{A.6}$$

where ϕ is the azimuthal angle in the observer's frame and d is the distance of the disk to the observer. The terms db and $d\phi$ are expressed in term of $d\xi$ in (A.9) and $d\phi'$ in (A.16), where ξ is the normalized radius of the line-emitting region on the disk in units of gravitational radius, i.e., $\xi = r/M$ where $G = 1$ and $c = 1$.

As a result, the observed flux is the integral of the emitting intensity I_{ν_e} over the entire disk:

$$\begin{aligned} F_\nu &= \int\int I_{\nu_e} D^3 \frac{b \, db \, d\phi}{d^2} \\ &= \frac{M^2}{d^2} \int_0^{2\pi} \int_{\xi_1}^{\xi_2} I_{\nu_e} D^3 \left(1 + \frac{1}{\xi} \frac{1 - \sin i \cos\phi'}{1 + \sin i \cos\phi'}\right) \xi \, d\xi \, d\phi' \\ &= \frac{M^2}{d^2} \int_0^{2\pi} \int_{\xi_1}^{\xi_2} I_{\nu_e} D^3 \, \Psi(\xi, \phi', i) \, \xi \, d\xi \, d\phi', \end{aligned} \tag{A.7}$$

where ξ_1 and ξ_2 are the inner and outer radii of the emitting region on the disk, respectively. The term $\Psi(\xi, \phi', i) = \left(1 + \frac{1}{\xi}\frac{1-\sin i\cos\phi'}{1+\sin i\cos\phi'}\right)$ includes gravitational redshift and light bending effects. The term D is the relativistic Doppler factor. In the Schwarzschild metric, it is derived by Chen et al. (1989):

$$D = \left(1 - \frac{3}{\xi}\right)^{1/2} \left(1 + \xi^{-1/2}\sin i \sin\phi'\right)^{-1}. \tag{A.8}$$

A.1.1 Impact Parameter

In the weak field approximation (Adler et al. 1975), the impact parameter is given:

$$\begin{aligned} b &\simeq r\sin\theta + \frac{M}{2\sin\theta}(3 - 4\cos\theta + \cos 2\theta) \\ &\simeq M\xi\sin\theta\left[1 + \frac{1}{2\xi\sin^2\theta}(3 - 4\cos\theta + \cos 2\theta)\right], \end{aligned} \tag{A.9}$$

where $\xi = r/M$, $G = 1$ and $c = 1$. The expression is needed to rewrite the result in the disk frame only. This can be done using (A.2):

$$\sin\theta = (1 - \cos^2\theta)^{1/2} = (1 - \sin^2 i\cos^2\phi')^{1/2}, \tag{A.10}$$

and

$$\begin{aligned} 3 - 4\cos\theta + \cos 2\theta &= 3 - 4\cos\theta + 2\cos^2\theta - 1 \\ &= 2(1 - 2\cos\theta + \cos^2\theta) \\ &= 2(1 - \cos\theta)^2 \\ &= 2(1 - \sin i\cos\theta')^2. \end{aligned} \tag{A.11}$$

Equation (A.9) then becomes

$$\begin{aligned} b &\simeq M\xi(1 - \sin^2 i\cos^2\phi')^{1/2}\left[1 + \frac{(1 - \sin i\cos\theta')^2}{\xi(1 - \sin^2 i\cos^2\phi')}\right] \\ &\simeq M\xi(1 - \sin^2 i\cos^2\phi')^{1/2}\left[1 + \frac{1}{\xi}\frac{1 - \sin i\cos\theta'}{1 - \sin i\cos\phi'}\right] \\ &\simeq M(1 - \sin^2 i\cos^2\phi')^{1/2}\left[\xi + \frac{1 - \sin i\cos\theta'}{1 - \sin i\cos\phi'}\right], \end{aligned} \tag{A.12}$$

and differentiating,

$$db \simeq M(1 - \sin^2 i\cos^2\phi')^{1/2}\, d\xi. \tag{A.13}$$

A.1.2 Azimuthal angle

The following calculation is needed to express the azimuthal angle ϕ in the disk frame. From (A.1) and (A.2),

$$\begin{aligned}\sin\phi &= \frac{\sin\phi'}{\sin\theta} \\ &= \sin\phi'(1-\cos^2\theta)^{-1/2} \\ &= \sin\phi'(1-\sin^2 i\cos^2\phi')^{-1/2}. \end{aligned} \tag{A.14}$$

Differentiating,

$$\begin{aligned}\cos\phi\, d\phi &= d\phi'[\cos\phi'(1-\sin^2 i\cos^2\phi')^{-1/2} \\ &\quad -\sin^2\phi'\sin^2 i\cos\phi'(1-\sin^2 i\cos^2\phi')^{-3/2}]. \end{aligned} \tag{A.15}$$

To simplify it,

$$\begin{aligned}\cos\phi\frac{d\phi}{d\phi'} &= \cos\phi'(1-\sin^2 i\cos^2\phi')^{-1/2}\left[1-\frac{\sin^2\phi'\sin^2 i}{1-\sin^2 i\cos^2\phi'}\right] \\ &= \cos\phi'(1-\sin^2 i\cos^2\phi')^{-1/2}\left[\frac{1-\sin^2 i\cos^2\phi'-\sin^2 i\sin^2\phi'}{1-\sin^2 i\cos^2\phi'}\right] \\ &= \cos\phi'\cos^2 i(1-\sin^2 i\cos^2\phi')^{-3/2}, \end{aligned} \tag{A.16}$$

Next, to express $\cos\phi$ in the disk frame,

$$\begin{aligned}\cos\phi &= (1-\sin^2\phi)^{1/2} \\ &= \left(1-\frac{\sin^2\phi'}{\sin^2\theta}\right)^{1/2} \\ &= \left(1-\frac{\sin^2\phi'}{1-\cos^2\theta}\right)^{1/2} \\ &= \left(1-\frac{\sin^2\phi'}{1-\sin^2 i\cos^2\phi'}\right)^{1/2} \\ &= \left(\frac{1-\sin^2 i\cos^2\phi'-\sin^2\phi'}{1-\sin^2 i\cos^2\phi'}\right)^{1/2} \\ &= \left(\frac{\cos^2\phi'-\sin^2 i\cos^2\phi'}{1-\sin^2 i\cos^2\phi'}\right)^{1/2} \\ &= \left(\frac{\cos^2\phi'\cos^2 i}{1-\sin^2 i\cos^2\phi'}\right)^{1/2}., \end{aligned} \tag{A.17}$$

substitute Equation (A.17) into (A.16),

$$\begin{aligned} d\phi &= d\phi' \cos\phi' \cos^2 i (1 - \sin^2 i \cos^2 \phi')^{-3/2} \left(\frac{\cos^2 \phi' \cos^2 i}{1 - \sin^2 i \cos^2 \phi'} \right)^{-1/2} \\ &= d\phi' \left(\frac{\cos i}{1 - \sin^2 i \cos^2 \phi'} \right). \end{aligned} \tag{A.18}$$

A.2 EMISSIVITY FUNCTION THROUGH A DISK-WIND

The specific intensity of a line in the disk frame including local broadening has the form of

$$I_{\nu_e}(\xi, \phi', \nu_e) = \epsilon(\xi, \phi') \exp\left[-\frac{(\nu_e - \nu_0)^2}{2\sigma^2} \right], \tag{A.19}$$

where $\epsilon(\xi, \phi')$ is the emissivity function of the disk, and the exponential function is the Gaussian distribution of the emitting frequency ν_e characterized by the rest frequency of the line ν_0 and the local broadening parameter σ. The disk wind above the disk changes the probability for a photon to escape the wind in the direction of the observer. The emissivity function is modified as

$$\epsilon(\xi, \phi') = \epsilon_0(\xi) \frac{1 - e^{-\tau}}{\tau}, \tag{A.20}$$

where $\epsilon_0(\xi)$ varies as a power law with radius, τ is the optical depth through the emitting layer along the line of sight in the direction $\hat{n}$, and the last term $(1 - e^{-\tau})/\tau$ is the escape probability of a photon. Using the Sobolev approximation for flows whose component to the line-of-sight is non-monotonic (Rybicki & Hummer 1978), the optical depth is given as

$$\tau = \frac{\kappa \rho \sigma}{|\hat{n} \cdot \Lambda \cdot \hat{n}|}, \tag{A.21}$$

where κ is the line absorption coefficients, ρ is the density of emitting material, σ is the local velocity dispersion by thermal or turbulent effects in the emitting layer, $\hat{n}$ is the observer's line-of-sight vector, and Λ is the symmetric strain tensor. As ρ can be expressed as power laws in ξ, the optical depth can then be rewritten as

$$\tau = \xi^{\eta} \frac{\tau_0}{|\hat{n} \cdot \Lambda \cdot \hat{n}|}, \tag{A.22}$$

where τ_0 is the normalized optical depth averaged over ϕ' at $\xi_{\rm min}$ of the line emitting region.

The line-emitting flux can be evaluated when τ is known. To calculate τ, the analytic velocity structure is needed to compute the double dot product of the strain tensor denoted as Q in the form of

$$Q = |\hat{n} \cdot \Lambda \cdot \hat{n}| = \sum_i \sum_j n_i n_j e_{ij}, \tag{A.23}$$

where e_{ij} are the strain tensor elements. In spherical coordinates of the disk frame, the strain tensor elements are given from Batchelor (2000):

$$e_{rr} = \frac{\partial v_r}{\partial r} \tag{A.24}$$

$$e_{\theta'\theta'} = \frac{1}{r}\frac{\partial v_{\theta'}}{\partial \theta'} + \frac{v_r}{r} \tag{A.25}$$

$$e_{\phi'\phi'} = \frac{1}{r\sin\theta'}\frac{\partial v_{\phi'}}{\partial \phi'} + \frac{v_r}{r} + \frac{v_{\theta'}\cot\theta'}{r} \tag{A.26}$$

$$e_{\theta'\phi'} = \frac{\sin\theta'}{2r}\frac{\partial}{\partial\theta'}\left(\frac{v_{\phi'}}{\sin\theta'}\right) + \frac{1}{2r\sin\theta'}\frac{\partial v_{\theta'}}{\partial\phi'} \tag{A.27}$$

$$e_{\phi' r} = \frac{1}{2r\sin\theta'}\frac{\partial v_r}{\partial\phi'} + \frac{r}{2}\frac{\partial}{\partial r}\left(\frac{v_{\phi'}}{r}\right) \tag{A.28}$$

$$e_{r\theta'} = \frac{r}{2}\frac{\partial}{\partial r}\left(\frac{v_{\theta'}}{r}\right) + \frac{1}{2r}\frac{\partial v_r}{\partial\theta'} \tag{A.29}$$

$$\tag{A.30}$$

where v_r, $v_{\theta'}$ and $v_{\phi'}$ are the velocity components of the disk wind in the disk frame.

Adopting the Murray et al. (1995) analytical disk-wind model, the velocity field is

$$v_r = v_\infty\left(1 - \frac{r_f}{r}\right)^\beta \tag{A.31}$$

$$v_{\theta'} = -v_r \sin\lambda(r) \tag{A.32}$$

$$v_{\phi'} = \left(\frac{GM}{r_f}\right)^{1/2}\frac{r}{r_f} \tag{A.33}$$

where β is taken to be 1, and r_f is the radius of the footprint of the wind stream (at the base of the wind). $\lambda(r)$ is the opening angle of the wind measured from the disk which varies with radius $\lambda(r) = \lambda(r_{min})(r_{min}/r)$, where r_{min} is the inner radius of the line-emitting region of the disk. The terminal velocity of the wind is $v_\infty = 4.7 v_{\phi'}$, according to Equation (2) of Murray & Chiang (1998).

According to Flohic et al. (2012), they used this analytical velocity field to calculate Q:

$$Q = \frac{v_\infty}{r}\left[\sin^2 i\left(\cos^2\phi' + \frac{3}{2}\frac{v_{\phi'}}{v_\infty}\sin\phi'\cos\phi'\right) + \cos i\left(\frac{\sin i\cos\phi'}{\sin\lambda} + \cos i + \frac{v_{\phi'}}{v_\infty}\frac{\sin i\sin\phi'}{2\sin\lambda}\right)\right]. \quad \text{(A.34)}$$

In contrast, Murray & Chiang (1997) derived a different Q:

$$Q = \frac{v_\infty}{r}\left[\sin^2 i\left(\cos^2\phi' + \frac{3}{2}\frac{v_{\phi'}}{v_\infty}\sin\phi'\cos\phi'\right) - \cos i\left(\sin i\cos\phi'\cot\lambda + \cos i + \frac{v_{\phi'}}{v_\infty}\frac{\sin i\sin\phi'}{2r\sin\lambda}\right)\right]. \quad \text{(A.35)}$$

The two expressions are different in the second term in square brackets, where Equation (A.34) shows $\sin i\cos\phi'/\sin\lambda$, but Equation (A.35) shows $\sin i\cos\phi'\cot\lambda$. They are approximately equal when λ is small. There is a more substantial difference in the sign of $\cos i$. Flohic et al. (2012) confirms that this difference is due to a sign error in Murray & Chiang (1997).

It is noted that the Murray & Chiang (1997) analytical velocity field is constrained for the case of the equatorial wind where its opening angle λ is small. However, the constraint will be relaxed in this empirical work. Thus I modify the velocity field in polar component as $v_\theta = -v_r\tan\lambda(r)$ such that the wind can be in polar. The expression of Q then becomes:

$$Q = \frac{v_\infty}{r}\left[\sin^2 i\left(\cos^2\phi' + \frac{3}{2}\frac{v_{\phi'}}{v_\infty}\sin\phi'\cos\phi'\right) + \cos i\left(\sin i\cos\phi'\left(\tan\lambda + \frac{1}{\sin\lambda}\right) + \frac{\cos i}{\cos\lambda} + \frac{v_{\phi'}}{v_\infty}\frac{\sin i\sin\phi'}{2\sin\lambda}\right)\right]. \quad \text{(A.36)}$$

As suggested by Hall & Chajet (2010), in order to have blueshifts comparable to the observed CIV line profiles, the wind launch velocity at each radius must equal the Keplerian velocity at that radius. The streamlines are straight with constant poloidal angle λ. I therefore modify the radial velocity:

$$v_r = v_\infty\left(1 - \frac{r_f}{r}\right)^\beta + v_{\phi'}\cos\lambda. \quad \text{(A.37)}$$

The expression for Q becomes:

$$\begin{aligned} Q &= \frac{v_\infty}{r}\left[\sin^2 i\left(A\cos^2\phi' + \frac{3}{2}\frac{v_{\phi'}}{v_\infty}\sin\phi'\cos\phi' + B\right)\right. \\ &\left. + \cos i\left(A\sin i\cos\phi'\left(\tan\lambda + \frac{1}{\sin\lambda}\right) + A\frac{\cos i}{\cos\lambda} + C + \frac{v_{\phi'}}{v_\infty}\frac{\sin i\sin\phi'}{2\sin\lambda}\right)\right], \end{aligned} \tag{A.38}$$

where

$$A = 1 - \frac{v_{\phi'}}{v_\infty}\cos\lambda, \tag{A.39}$$

$$B = \frac{v_{\phi'}}{v_\infty}\cos\lambda\sin^2\phi', \tag{A.40}$$

$$C = \frac{v_{\phi'}}{v_\infty}\left(\cos i - \sin i\tan\lambda\cos\phi'\right). \tag{A.41}$$

BIBLIOGRAPHY

Abbott, D. C. 1982, ApJ, 259, 282

Adler, R., Bazin, M., & Schiffer, M. 1975, Introduction to general relativity.

Aihara, H., et al. 2011, ApJS, 193, 29

Allen, J. T., Hewett, P. C., Maddox, N., Richards, G. T., & Belokurov, V. 2011, MNRAS, 410, 860

Antonucci, R. 1993, ARA&A, 31, 473

Antonucci, R. R. J., & Miller, J. S. 1985, ApJ, 297, 621

Arav, N., Barlow, T. A., Laor, A., & Blandford, R. D. 1997, MNRAS, 288, 1015

Arav, N., Barlow, T. A., Laor, A., Sargent, W. L. W., & Blandford, R. D. 1998, MNRAS, 297, 990

Arav, N., Becker, R. H., Laurent-Muehleisen, S. A., Gregg, M. D., White, R. L., Brotherton, M. S., & de Kool, M. 1999, ApJ, 524, 566

Arav, N., & Li, Z. 1994, ApJ, 427, 700

Arav, N., et al. 2012, ArXiv e-prints

Bahcall, J. N., Kozlovsky, B.-Z., & Salpeter, E. E. 1972, ApJ, 171, 467

Bardeen, J. M. 1970, Nature, 226, 64

Barlow, T. A. 1994, PASP, 106, 548

Barlow, T. A., Junkkarinen, V. T., Burbidge, E. M., Weymann, R. J., Morris, S. L., & Korista, K. T. 1992a, ApJ, 397, 81

—. 1992b, ApJ, 397, 81

Batchelor, G. K. 2000, An Introduction to Fluid Dynamics

Begeman, K. G., Broeils, A. H., & Sanders, R. H. 1991, MNRAS, 249, 523

Bickerton, S., Badenes, C., Hettinger, T., Beers, T., & Huang, S. 2012, in IAU Symposium, Vol. 285, IAU Symposium, 289–290

Blaes, O. 2004, in Astronomical Society of the Pacific Conference Series, Vol. 311, AGN Physics with the Sloan Digital Sky Survey, ed. G. T. Richards & P. B. Hall, 121

Blandford, R. D. 1990, in Active Galactic Nuclei, ed. R. D. Blandford, H. Netzer, L. Woltjer, T. J.-L. Courvoisier, & M. Mayor, 161–275

Blandford, R. D., & McKee, C. F. 1982, ApJ, 255, 419

Bon, E., Gavrilović, N., La Mura, G., & Popović, L. Č. 2009a, New A Rev., 53, 121

Bon, E., Popović, L. Č., Gavrilović, N., Mura, G. L., & Mediavilla, E. 2009b, MNRAS, 400, 924

Bon, E., Popović, L. Č., Ilić, D., & Mediavilla, E. 2006, New A Rev., 50, 716

Borguet, B. C. J., Arav, N., Edmonds, D., Chamberlain, C., & Benn, C. 2013, ApJ, 762, 49

Boroson, T. A., & Green, R. F. 1992, ApJS, 80, 109

Boyce, P. J., et al. 1996, ApJ, 473, 760

Bushouse, H. A., et al. 2002, ApJS, 138, 1

Cao, X., & Wang, T.-G. 2006, ApJ, 652, 112

Castor, J. I., Abbott, D. C., & Klein, R. I. 1975, ApJ, 195, 157

Chen, K., & Halpern, J. P. 1989, ApJ, 344, 115

Chen, K., Halpern, J. P., & Filippenko, A. V. 1989, ApJ, 339, 742

Chiang, J., & Murray, N. 1996, ApJ, 466, 704

Clavel, J., et al. 1991, ApJ, 366, 64

Colella, P., & Woodward, P. R. 1984, Journal of Computational Physics, 54, 174

Collier, S. J., et al. 1998, ApJ, 500, 162

Collin, S., Boisson, C., Mouchet, M., Dumont, A., Coupé, S., Porquet, D., & Rokaki, E. 2002, A&A, 388, 771

Collin, S., & Huré, J. 2001, A&A, 372, 50

Corbin, M. R. 1997, ApJ, 485, 517

Crenshaw, D. M., & Blackwell, Jr., J. H. 1990, ApJ, 358, L37

Cunningham, C. T. 1975, ApJ, 202, 788

Czerny, B., & Elvis, M. 1987, ApJ, 321, 305

Czerny, B., Witt, H. J., & Zycki, P. T. 1996, ArXiv Astrophysics e-prints

Dai, X., Shankar, F., & Sivakoff, G. R. 2008, ApJ, 672, 108

Davidson, K., & Netzer, H. 1979, Reviews of Modern Physics, 51, 715

Davis, S. W., Woo, J., & Blaes, O. M. 2007, ApJ, 668, 682

de Vries, W. H., Becker, R. H., & White, R. L. 2006, AJ, 131, 666

Decarli, R., Labita, M., Treves, A., & Falomo, R. 2008, in 8th National Conference on AGN, ed. L. Lanteri, C. M. Raiteri, A. Capetti, & P. Rossi

Denney, K. D., Peterson, B. M., Dietrich, M., Vestergaard, M., & Bentz, M. C. 2009, ApJ, 692, 246

Denney, K. D., et al. 2010, ApJ, 721, 715

Dunn, J. P., et al. 2010, ApJ, 709, 611

Edmonds, D., et al. 2011, ApJ, 739, 7

Elvis, M. 2000, ApJ, 545, 63

Elvis, M. 2010, in IAU Symposium, Vol. 267, IAU Symposium, 55–64

Elvis, M., et al. 1994, ApJS, 95, 1

Eracleous, M., & Halpern, J. P. 2003, ApJ, 599, 886

Eracleous, M., Livio, M., Halpern, J. P., & Storchi-Bergmann, T. 1995, ApJ, 438, 610

Ferrara, A., & Pietrini, P. 1993, ApJ, 405, 130

Flohic, H. M. L. 2008, PhD thesis, The Pennsylvania State University

Flohic, H. M. L. G., Eracleous, M., & Bogdanović, T. 2012, ApJ, 753, 133

Foltz, C. B., Weymann, R. J., Morris, S. L., & Turnshek, D. A. 1987, ApJ, 317, 450

Gallagher, S. C., Brandt, W. N., Wills, B. J., Charlton, J. C., Chartas, G., & Laor, A. 2004, ApJ, 603, 425

Gammie, C. F., Shapiro, S. L., & McKinney, J. C. 2004, ApJ, 602, 312

Gaskell, C. M., & Goosmann, R. W. 2008, ArXiv e-prints

Gayley, K. G. 1995, ApJ, 454, 410

Gibson, R. R., Brandt, W. N., Gallagher, S. C., Hewett, P. C., & Schneider, D. P. 2010, ApJ, 713, 220

Gibson, R. R., Brandt, W. N., Schneider, D. P., & Gallagher, S. C. 2008, ApJ, 675, 985

Gilbert, A. M., Eracleous, M., Filippenko, A. V., & Halpern, J. P. 1999, in Astronomical Society of the Pacific Conference Series, Vol. 175, Structure and Kinematics of Quasar Broad Line Regions, ed. C. M. Gaskell, W. N. Brandt, M. Dietrich, D. Dultzin-Hacyan, & M. Eracleous, 189

Giveon, U., Maoz, D., Kaspi, S., Netzer, H., & Smith, P. S. 1999, MNRAS, 306, 637

Goodman, J. 2003, MNRAS, 339, 937

Green, P. J., Aldcroft, T. L., Mathur, S., Wilkes, B. J., & Elvis, M. 2001, ApJ, 558, 109

Greenstein, J. L., & Schmidt, M. 1964, ApJ, 140, 1

Grier, C. J., et al. 2012, ApJ, 744, L4

Haggard, D., Arraki, K. S., Green, P. J., Aldcroft, T., & Anderson, S. F. 2012, ArXiv e-prints

Hall, P. B., & Chajet, L. S. 2010, in IAU Symposium, Vol. 267, IAU Symposium, 398–398

Hall, P. B., Sadavoy, S. I., Hutsemekers, D., Everett, J. E., & Rafiee, A. 2007, ApJ, 665, 174

Hamann, F., Barlow, T. A., Junkkarinen, V., & Burbidge, E. M. 1997, ApJ, 478, 80

Hamann, F., Kaplan, K. F., Rodríguez Hidalgo, P., Prochaska, J. X., & Herbert-Fort, S. 2008, MNRAS, 391, L39

Hamann, F., Korista, K. T., & Morris, S. L. 1993, ApJ, 415, 541

Hamann, F., & Sabra, B. 2004, in Astronomical Society of the Pacific Conference Series, Vol. 311, AGN Physics with the Sloan Digital Sky Survey, ed. G. T. Richards & P. B. Hall, 203

Hewett, P. C., & Foltz, C. B. 2003, AJ, 125, 1784

Hines, D. C., Low, F. J., Thompson, R. I., Weymann, R. J., & Storrie-Lombardi, L. J. 1999, ApJ, 512, 140

Hook, I. M., McMahon, R. G., Boyle, B. J., & Irwin, M. J. 1994, MNRAS, 268, 305

Hu, C., Wang, J.-M., Ho, L. C., Chen, Y.-M., Bian, W.-H., & Xue, S.-J. 2008, ApJ, 683, L115

Ilić, D., Popović, L. Č., Bon, E., Mediavilla, E. G., & Chavushyan, V. H. 2006, MNRAS, 371, 1610

Jovanović, P., & Popović, L. Č. 2008, Fortschritte der Physik, 56, 456

Junkkarinen, V. T. 1983, ApJ, 265, 73

Junkkarinen, V. T., Burbidge, E. M., & Smith, H. E. 1987, ApJ, 317, 460

Kallman, T. R., & Krolik, J. H. 1986, ApJ, 308, 805

Kaspi, S., Brandt, W. N., Maoz, D., Netzer, H., Schneider, D. P., & Shemmer, O. 2007, ApJ, 659, 997

Kaspi, S., Maoz, D., Netzer, H., Peterson, B. M., Vestergaard, M., & Jannuzi, B. T. 2005, ApJ, 629, 61

Kaspi, S., Smith, P. S., Netzer, H., Maoz, D., Jannuzi, B. T., & Giveon, U. 2000, ApJ, 533, 631

Kawaguchi, T., Pierens, A., & Huré, J.-M. 2004, A&A, 415, 47

Kollatschny, W. 2003, A&A, 407, 461

Koratkar, A., & Blaes, O. 1999, PASP, 111, 1

Koratkar, A. P., & Gaskell, C. M. 1989, in Bulletin of the American Astronomical Society, Vol. 21, Bulletin of the American Astronomical Society, 754

Koratkar, A. P., & Gaskell, C. M. 1991, ApJS, 75, 719

Korista, K. T., Baldwin, J. A., Ferland, G. J., Verner, D. A., & Ferguson, J. W. 1996, in Bulletin of the American Astronomical Society, Vol. 28, American Astronomical Society Meeting Abstracts #188, 825

Korista, K. T., et al. 1995, ApJS, 97, 285

Krolik, J. H. 1999, The Observatory, 119, 306

Krolik, J. H., & Kriss, G. A. 2001, ArXiv Astrophysics e-prints

Krongold, Y., Binette, L., & Hernández-Ibarra, F. 2010, ApJ, 724, L203

Ku, W. H.-M., Helfand, D. J., & Lucy, L. B. 1980, Nature, 288, 323

Lamers, H. J. G. L. M., & Cassinelli, J. P. 1999, Introduction to Stellar Winds

Laor, A. 1990, MNRAS, 246, 369

—. 1991, ApJ, 376, 90

Lin, D. N. C., & Papaloizou, J. C. B. 1996, ARA&A, 34, 703

Lípari, S. L., & Terlevich, R. J. 2006, MNRAS, 368, 1001

Lundgren, B. F., Wilhite, B. C., Brunner, R. J., Hall, P. B., Schneider, D. P., York, D. G., Vanden Berk, D. E., & Brinkmann, J. 2007, ApJ, 656, 73

Ma, F. 2002, MNRAS, 335, L99

Malkan, M. A. 1983, ApJ, 268, 582

Mardaljevic, J., Raine, D. J., & Walsh, D. 1988, Astrophysical Letters Communications, 26, 357

Marziani, P., Sulentic, J. W., Calvani, M., Perez, E., Moles, M., & Penston, M. V. 1993, ApJ, 410, 56

Marziani, P., Zamanov, R., Sulentic, J. W., Dultzin-Hacyan, D., Bongardo, C., & Calvani, M. 2003, in Astronomical Society of the Pacific Conference Series, Vol. 290, Active Galactic Nuclei: From Central Engine to Host Galaxy, ed. S. Collin, F. Combes, & I. Shlosman, 229

Mathews, W. G., & Capriotti, E. R. 1985, in Astrophysics of Active Galaxies and Quasi-Stellar Objects, ed. J. S. Miller, 185–233

McLure, R. J., & Jarvis, M. J. 2002, MNRAS, 337, 109

Mirabel, I. F., & Rodríguez, L. F. 1999, ARA&A, 37, 409

Misawa, T., Eracleous, M., Charlton, J. C., & Tajitsu, A. 2005, ApJ, 629, 115

Moran, E. C., Barth, A. J., Kay, L. E., & Filippenko, A. V. 2000, ApJ, 540, L73

Morgan, C. W., Kochanek, C. S., Morgan, N. D., & Falco, E. E. 2010, ApJ, 712, 1129

Murray, N., & Chiang, J. 1997, ApJ, 474, 91

—. 1998, ApJ, 494, 125

Murray, N., Chiang, J., Grossman, S. A., & Voit, G. M. 1995, ApJ, 451, 498

Mushotzky, R. F., Done, C., & Pounds, K. A. 1993, ARA&A, 31, 717

Nandra, K., Clavel, J., Edelson, R. A., George, I. M., Malkan, M. A., Mushotzky, R. F., Peterson, B. M., & Turner, T. J. 1998, ApJ, 505, 594

Narayanan, D., Hamann, F., Barlow, T., Burbidge, E. M., Cohen, R. D., Junkkarinen, V., & Lyons, R. 2004, ApJ, 601, 715

Netzer, H. 1999, Astronomische Nachrichten, 320, 171

Netzer, H., et al. 1996, MNRAS, 279, 429

Novikov, I. D., & Thorne, K. S. 1973, in Black Holes (Les Astres Occlus), ed. A. Giannaras, 343–450

Obrien, P. T., Gondhalekar, P. M., & Wilson, R. 1988, MNRAS, 233, 845

O'Brien, P. T., & Harries, T. J. 1991, MNRAS, 250, 133

Ogle, P. M. 1997, in Astronomical Society of the Pacific Conference Series, Vol. 128, Mass Ejection from Active Galactic Nuclei, ed. N. Arav, I. Shlosman, & R. J. Weymann, 78

Owocki, S. P., Castor, J. I., & Rybicki, G. B. 1988, ApJ, 335, 914

Owocki, S. P., Cranmer, S. R., & Blondin, J. M. 1994, ApJ, 424, 887

Page, D. N., & Thorne, K. S. 1974, ApJ, 191, 499

Pereyra, N. A., Hillier, D. J., & Turnshek, D. A. 2006, ApJ, 636, 411

Pereyra, N. A., & Kallman, T. R. 2003, ApJ, 582, 984

Pereyra, N. A., Kallman, T. R., & Blondin, J. M. 1997, ApJ, 477, 368

—. 2000, ApJ, 532, 563

Pereyra, N. A., Owocki, S. P., Hillier, D. J., & Turnshek, D. A. 2004, ApJ, 608, 454

Perez, E., Penston, M. V., & Moles, M. 1989, MNRAS, 239, 55

Peterson, B. M. 1993, PASP, 105, 247

Peterson, B. M. 1994, in Astronomical Society of the Pacific Conference Series, Vol. 69, Reverberation Mapping of the Broad-Line Region in Active Galactic Nuclei, ed. P. M. Gondhalekar, K. Horne, & B. M. Peterson, 1

—. 1997, An Introduction to Active Galactic Nuclei

—. 1998, Advances in Space Research, 21, 57

Peterson, B. M. 2006, in Lecture Notes in Physics, Berlin Springer Verlag, Vol. 693, Physics of Active Galactic Nuclei at all Scales, ed. D. Alloin

Peterson, B. M. 2011, in Narrow-Line Seyfert 1 Galaxies and their Place in the Universe

Peterson, B. M., & Wandel, A. 1999, ApJ, 521, L95

Peterson, B. M., Wanders, I., Horne, K., Collier, S., Alexander, T., Kaspi, S., & Maoz, D. 1998, PASP, 110, 660

Peterson, B. M., et al. 1999, ApJ, 510, 659

—. 2004, ApJ, 613, 682

Polletta, M., Weedman, D., Hoenig, S., Lonsdale, C., Wilkes, B., & Kilgard, R. 2007, in X-ray Surveys, Evolution of Accretion, Star-Formation and the Large Scale Structure

Popovic, L., Stanic, N., Kubicela, A., & Bon, E. 2001, Astronomical and Astrophysical Transactions, 20, 319

Popović, L. Č., Mediavilla, E., Bon, E., & Ilić, D. 2004, A&A, 423, 909

Popović, L. Č., Mediavilla, E. G., Bon, E., Stanić, N., & Kubičela, A. 2003, ApJ, 599, 185

Popović, L. Č., Mediavilla, E. G., Kubičela, A., & Jovanović, P. 2002, A&A, 390, 473

Proga, D. 2000, ApJ, 538, 684

Proga, D., Stone, J. M., & Drew, J. E. 1998, MNRAS, 295, 595

—. 1999, MNRAS, 310, 476

Proga, D., Stone, J. M., & Kallman, T. R. 2000, ApJ, 543, 686

Raimundo, S. I., Fabian, A. C., Vasudevan, R. V., Gandhi, P., & Wu, J. 2012, MNRAS, 419, 2529

Rees, M. J. 1984, ARA&A, 22, 471

Reichard, T. A., et al. 2003, AJ, 125, 1711

Richards, G. T., Vanden Berk, D. E., Reichard, T. A., Hall, P. B., Schneider, D. P., SubbaRao, M., Thakar, A. R., & York, D. G. 2002, AJ, 124, 1

Rodriguez Hidalgo, P., Hamann, F., Eracleous, M., Capellupo, D., Charlton, J., & Shields, J. 2012, ArXiv e-prints

Romano, P., Zwitter, T., Calvani, M., & Sulentic, J. 1996, MNRAS, 279, 165

Runnoe, J. C., Brotherton, M. S., & Shang, Z. 2012, MNRAS, 422, 478

Rybicki, G. B., & Hummer, D. G. 1978, ApJ, 219, 654

Sanders, D. B., Phinney, E. S., Neugebauer, G., Soifer, B. T., & Matthews, K. 1989, ApJ, 347, 29

Shakura, N. I., & Sunyaev, R. A. 1973, A&A, 24, 337

Shields, G. A. 1978, Nature, 272, 706

Shields, J. C., Ferland, G. J., & Peterson, B. M. 1995, ApJ, 441, 507

Shlosman, I., & Begelman, M. C. 1987, Nature, 329, 810

Speith, R., Riffert, H., & Ruder, H. 1995, Computer Physics Communications, 88, 109

Stalin, C. S., Srianand, R., & Petitjean, P. 2011, MNRAS, 413, 1013

Stoughton, C., et al. 2002, AJ, 123, 485

Strateva, I. V., et al. 2003, AJ, 126, 1720

Sulentic, J. W., Marziani, P., & Dultzin-Hacyan, D. 2000, ARA&A, 38, 521

Sulentic, J. W., Rosado, M., Dultzin-Hacyan, D., Verdes-Montenegro, L., Trinchieri, G., Xu, C., & Pietsch, W. 2001, AJ, 122, 2993

Sun, W.-H., & Malkan, M. A. 1989, ApJ, 346, 68

Tanaka, Y., et al. 1995, Nature, 375, 659

Trevese, D., Stirpe, G., Vagnetti, F., Zitelli, V., & Paris, D. 2006, in Astronomical Society of the Pacific Conference Series, Vol. 360, Astronomical Society of the Pacific Conference Series, ed. C. M. Gaskell, I. M. McHardy, B. M. Peterson, & S. G. Sergeev , 201

Trump, J. R., et al. 2006, ApJS, 165, 1

Turnshek, D. A. 1984a, ApJ, 278, L87

—. 1984b, ApJ, 280, 51

Turnshek, D. A. 1988, in QSO Absorption Lines: Probing the Universe, ed. J. C. Blades, D. A. Turnshek, & C. A. Norman, 17

Turnshek, D. A., Grillmair, C. J., Foltz, C. B., & Weymann, R. J. 1988, ApJ, 325, 651

Turnshek, D. A., Kopko, Jr., M., Monier, E., Noll, D., Espey, B. R., & Weymann, R. J. 1996, ApJ, 463, 110

Turnshek, D. A., Weymann, R. J., Liebert, J. W., Williams, R. E., & Strittmatter, P. A. 1980, ApJ, 238, 488

Ulrich, M., Maraschi, L., & Urry, C. M. 1997, ARA&A, 35, 445

Ulrich, M.-H., Courvoisier, T. J.-L., & Wamsteker, W. 1993, ApJ, 411, 125

Urry, C. M., & Padovani, P. 1995, PASP, 107, 803

Usher, P. D. 1978, ApJ, 222, 40

Vanden Berk, D. E., et al. 2004, ApJ, 601, 692

Veilleux, S., Cecil, G., & Bland-Hawthorn, J. 2005, ARA&A, 43, 769

Vestergaard, M., & Peterson, B. M. 2006, ApJ, 641, 689

Vilkoviskij, E. Y., Efimov, S. N., Karpova, O. G., & Pavlova, L. A. 1999, MNRAS, 309, 80

Vilkoviskij, E. Y., & Irwin, M. J. 2001, MNRAS, 321, 4

Wampler, E. J., Chugai, N. N., & Petitjean, P. 1995, ApJ, 443, 586

Wandel, A., Peterson, B. M., & Malkan, M. A. 1999, ApJ, 526, 579

Wandel, A., & Petrosian, V. 1988, ApJ, 329, L11

Warner, C., Hamann, F., & Dietrich, M. 2003, ApJ, 596, 72

Welsh, W. F., & Robinson, E. L. 2000, in NOAO Proposal ID #2000A-0210, 210

Weymann, R. J., Morris, S. L., Foltz, C. B., & Hewett, P. C. 1991, ApJ, 373, 23

Wild, V., & Hewett, P. C. 2010, ArXiv e-prints

Wilhite, B. C., Vanden Berk, D. E., Kron, R. G., Schneider, D. P., Pereyra, N., Brunner, R. J., Richards, G. T., & Brinkmann, J. V. 2005, ApJ, 633, 638

Yip, C. W., et al. 2009, AJ, 137, 5120

Zamorani, G., Maccacaro, T., Giommi, P., & Tananbaum, H. 1984, ApJ, 278, 28